Neutral Strange Particle Production in High Energy proton+proton Collisions

John Adams

Submitted for the Degree of Doctor of Philosophy

School of Physics and Astronomy

The University of Birmingham, U.K.

June 6, 2005

'Listen to advice and accept instruction, and in the end you will be wise'

Proverbs 19:20

'Luckily, life is not so easy as all that; otherwise we should get to the end too quickly,'

Sir Winston Churchill (1930)

Abstract

An enhancement in the number of strange particles produced in the collisions of relativistic heavy ions is expected to coincide with the formation of a de-confined state of partonic matter called the Quark-Gluon Plasma. Strangeness enhancement is an established Quark-Gluon Plasma Signature, and indeed was observed at CERN by the NA49 and WA97 experiments. The Solenoidal Tracker at RHIC (STAR) experiment is mainly devoted to the search for the Quark-Gluon Plasma so it is particularly important to determine if strangeness is also enhanced at RHIC, where the maximum centre of mass collision energy is an order of magnitude larger than at the CERN SPS.

This thesis describes the measurements of transverse momentum spectra for strange particles emerging from collisions of protons (p + p) at centre of mass energies of 200 GeV. Such measurements are essential as the strangeness yield from collisions of light ions, such as p + p, form a baseline to which results from heavy ion collisions (Au + Au) can be compared. In addition, other observables from p + p collisions, such as the shape of the spectra, and the variation in mean transverse momentum with multiplicity are interesting in their own right, as they relate to the collision dynamics.

The transverse momentum spectra for Λ, $\overline{\Lambda}$ and K^0_S were measured and found to be best described by a two component fit, inspired by elements of pQCD and thermal models. The yield of Λ, $\overline{\Lambda}$ and K^0_S were measured over the rapidity interval $y < 0.5$, and were found to be consistent with previous p + $\overline{\text{p}}$ collisions at the same centre of mass energy. The $\langle p_T \rangle$ was observed to increase with multiplicity for Λ, $\overline{\Lambda}$ and K^0_S. This agreed with earlier measurements, and was therefore consistent with a mini-jet production mechanism.

When the Λ and $\overline{\Lambda}$ yields were compared with those from Au + Au collisions at centre of mass energies of 200 GeV, an enhancement was observed. However the enhancement

explanation for the decrease in the enhancement factors is provided by thermal model analyses, which indicate a suppression of strange yields from low energy collisions of light particles, compared to collisions at higher energies.

Author's Contribution

The Solenoidal Tracker At RHIC (STAR) experiment is an international collaboration comprising ~ 570 collaborators from 51 institutions. The author has participated in biannual collaboration meetings since joining STAR in October 2001, and was also involved in taking data for runs 3 (2003) and 4 (2004). The author has attended weekly STAR phone meetings which focus on strange particle analysis, making regular contributions.

My work for the STAR collaboration has focused on analysing data from proton+proton collisions at $\sqrt{s} = 200$ GeV. Proton+proton collisions could be reconstructed using existing software, but not properly corrected. This was because of vertex reconstruction inefficiencies and the presence of additional 'pile-up' events within the detector. A significant part of the analysis work involved the development of vertex correction and pile-up rejection techniques, now used by other members of the collaboration.

The purpose of the analysis was to extract Λ, $\overline{\Lambda}$ and K^0_S signals from the proton+proton collision data and apply the correction techniques in order to extract the final particle yields. These yields, together with strange particle yields from heavy ion data form the basis of the strangeness enhancement plot which is a signature for the Quark Gluon Plasma. The data provided by this analysis has been used in various STAR collaboration presentations at international conferences.

Furthermore the author has presented posters of his work at two major international conferences (Strange Quark Matter 2003, N. Carolina, USA and Quark Matter 2004, Oakland, USA [1]) and given several talks at smaller conferences and summer schools.

Acknowledgements

Studying for this PhD has been harder process than I imagined, and has been helped by contributions from a large number of people. I would firstly like to thank Professor John Nelson for giving me the opportunity to return to physics as part of the Birmingham Relativistic Heavy Ion (RHI) group and as a member of the STAR collaboration. The Engineering and Physical Sciences Research Council (EPSRC) have funded me throughout my time as a post-graduate student, and I am extremely grateful for their support. The help and encouragement provided by Doctor Peter Jones, my supervisor, cannot be understated. As well as providing answers to my questions for the last three and a half years, Peter has spent many hours proof reading my thesis, and I am sure it is a much better document because of his comments.

I would like to acknowledge the work of the 570 STAR collaborators from which I have been lucky enough to benefit from. I would particularly like to mention Mark Heinz, Dr Richard Witt, Prof. Helen Caines, Prof. Rene Bellwied and Camelia Mironov for their helpfulness and interest in many aspects of my analysis. I would also thank Dr Gene Van Buren and Dr Olga Barannikova for helpful discussions regarding fit functions and vertex corrections respectively. Indeed, it was a real privilege to work with such a dedicated collection of scientists. Thanks must be extended to Jim Campbell, Dr Victor Ziman, Dr Jerome Lauret and Dr Iwona Sakrejda, for maintaining the computer systems on which I have worked.

I could not have undertaken this PhD without the help I received from the RHI group at Birmingham. I would like to thank Dr Lee Barnby, Leon Gaillard, Anthony Timmins, Dr Charles Blyth, and Dr Gordon Squire for many fascinating discussions and their thoughtful comments on my work. A special thanks must be accorded to Dr Matt

I would also like to thank the current head of nuclear physics, Dr Gary Tungate, and the other members of staff, Dr Martin Freer, Dr Paul Norman, Dr David Parker, Dr Norman Clarke, Paul Jagpal and Mrs Tina Campbell. I probably haven't been the easiest student to teach physics to over the years, as what understanding I have has been built up by asking questions. Thus in addition to Peter I would like to thank those who, through putting up with me, have inspired me most over the years; Mr Taylor, Mr Fitter, Dr D. Weaver and Dr S. Holloway.

My time at Birmingham has been an enjoyable one, mainly due to the large number of friends I have made over the last three and a half years. I will remember with great fondness the time spent with my house mates, particularly Carl, for those long drunken conversations and 'DIY' Bradley for saving my house, and being a thoroughly nice chap (as long as you didn't feed him scampi fries). I would like to thank Saher for her friendship but probably more for shouting and ranting at her computer, which strangely helped me feel better about my analysis. The other residents of E320 are deserving of mention for providing a friendly, lively and often entertaining, backdrop to work; these are Paul M, Tom, Dave P, Sybil, Joe, Nick, Neil, Marc, Phil and Ali. Great thanks must be extended to Dave F, Matt G, Mark, Yves, Yannis, Tamsin, Paul B and Bruce as their presence in the staff house bar after work was one of the most reliable and enjoyable aspects of the last few years.

Outside of University I would like to thank Dan, Mark, Paul, Tony and Rob for their friendship, and for enduring my student habits. The friends I have made at St Johns Church have all been an inspiration to my faith and I would particularly like to thank Pat, Howard, Martin, Ann, Tamsin, Mark, Nush, Sara, Stu, Liz, Sally, Tim R, Tim S, Jon, Harry, Sharon, Andy, Mike and Jen for helping me to understand God a little better. Finally I would like to thank my family from the bottom of my heart for the many, many hot dinners and for their unconditional love and support.

Contents

List of Figures

List of Tables

Chapter 1

Introduction

1.1 Evidence for Quarks

After the discovery of the neutron in 1932, it was believed that the proton and the neutron were fundamental constituents of nuclear matter. From the 1940s onwards a number of other similar strongly interacting particles, or hadrons, were observed in cosmic ray cloud chamber experiments. Indeed Figure 1.1 shows evidence for a neutral particle (a K meson) decaying into two charged pions. Some of these particles, such as the K^0, were observed to possess much longer lifetimes than expected. Due to this unexpected behaviour, such hadrons were called strange particles. However, there was no reason to believe that these strange particles, or indeed any of the others, were not also fundamental constituents of matter.

In the early sixties Gell-Mann (and, independently Zweig) tentatively put forward the idea that all hadrons could be categorised using various combinations of three different types of fractionally charged, spin 1/2, quarks [3]. In their model the quark was nothing more than a convenient mathematically derived quantity, having one of three flavours: up (u), down (d) or strange (s) that when grouped together formed hadrons with the correct, experimentally observed, quantum numbers. States with half integer spin, consisting of three quarks (qqq) were known as baryons, and hadrons with integer spin, consisting of quark anti-quark ($q\overline{q}$) pairs as mesons. All of the strangely behaving particles contained the strange quark, whereas the more familiar neutrons and protons consisted of just up

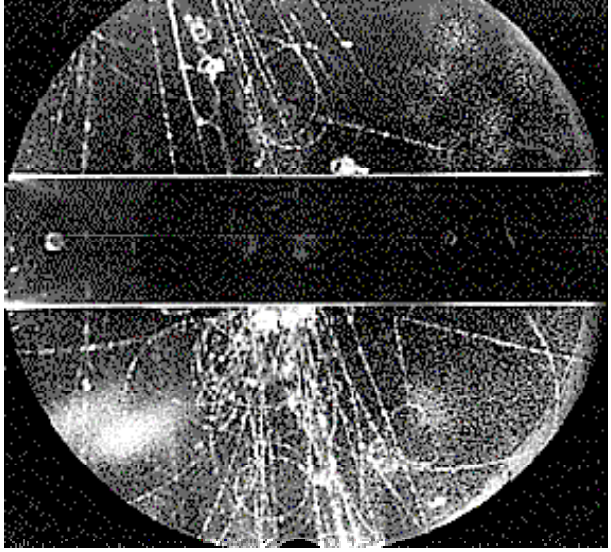

Figure 1.1: Cosmic rays produced a large number of different charged particles in the early cloud chamber experiments [2]. This image presents the first evidence for the K meson; being uncharged the K^0 leaves no track until it decays into 2 charged pions (see right side of the image, just below the central bar). This decay is characterised by a V shape. Neutral strange particle candidates are often referred to as v0 candidates in modern day high-energy experiments.

and down quarks. Hadrons are classified according to their hadronic spins and parities and each group is further arranged according to their strangeness and isospin quantum numbers, as shown in Figure 1.2. This simple model gained credibility due to its ability to predict previously unknown particle states.

Direct experimental evidence for quarks as constituent particles came in 1968 from the results of inelastic scattering of high energy electrons off protons [4]. As can be seen in Figure 1.3, most of the cross-section is due to the electron elastically scattering off the proton. There are also smaller mid-energy inelastic scattering peaks, which correspond to the creation of short-lived nucleon like states. Crucially however, below these peaks, the cross-section remains large. Feynman's quark-parton model helped explain this result and others from deep inelastic scattering experiments, by proposing that these data were consistent with the idea of an electron elastically scattering off smaller, non-interacting point like constituents [5]. Later experiments showed that Feynman's assumption of non-interacting quarks was incorrect. A better description of the internal dynamics of the proton is given by Quantum Chromo-Dynamics (QCD) [6], which describes interactions

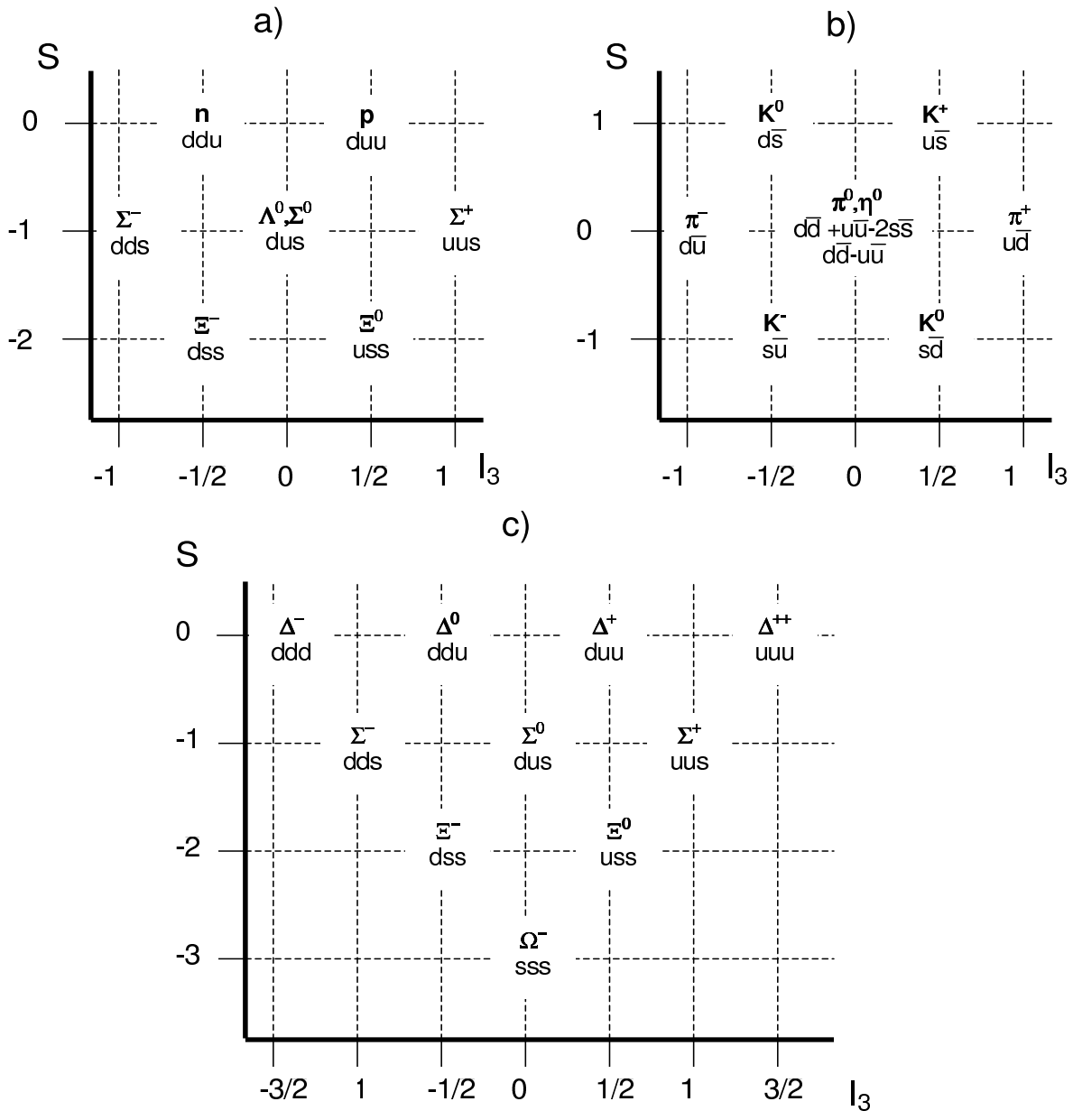

Figure 1.2: a) The octet of spin 1/2 even parity baryons, b) The octet of spin 0 odd parity mesons, c) The decuplet of spin 3/2 even parity baryons.

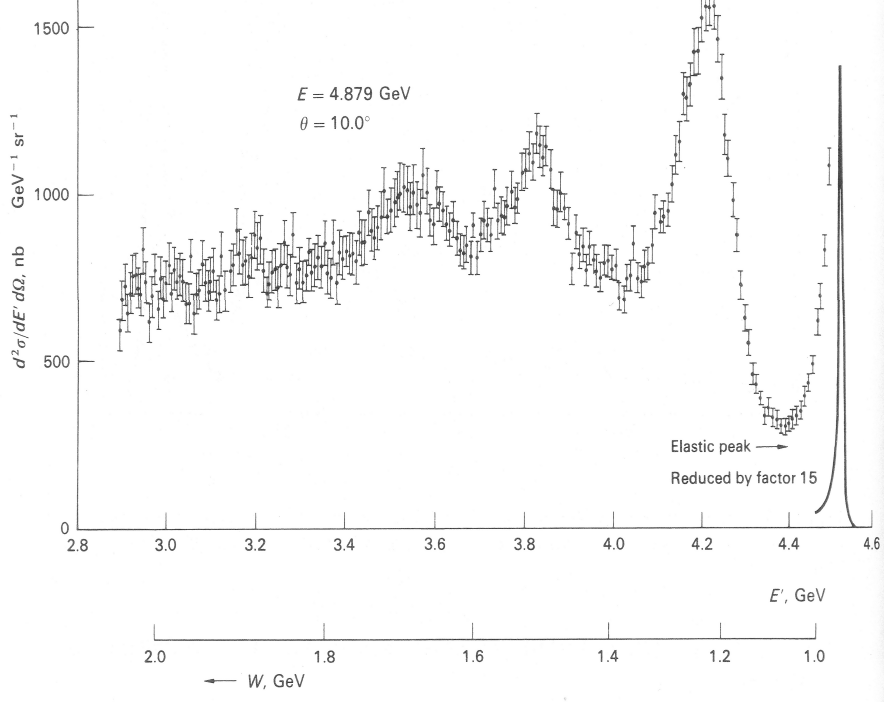

Figure 1.3: The first evidence for quarks came from measurements of scattered electrons off protons (taken from [4]). In the Figure, E' is the energy of the scattered electron, measured at 10°, and W is the mass of the recoiling hadronic state. The cross-section for electron proton scattering remains large for low scattered electron energies (E'), indicating finer structure within the proton.

between the quarks by gluon exchange.

Interactions in QCD require the exchange of colour between quarks and gluons (which collectively became known as partons). Gell-Man saw the need for this additional 'colour' quantum number in order to explain the existence of spin 3/2 hadrons such as the Δ^- (ddd), the Δ^+ (uuu) and the Ω^- (sss) as the Pauli exclusion principle forbids two identical particles to be in the same quantum state. To satisfy the exclusion principle each of the constituent quarks are postulated to have different colour charge. For baryons a combination of red (r), blue (b) and green (g) quarks makes a colourless state, where as for mesons a combination of a coloured quark and an anti-colour anti-quark ($\overline{r}$, $\overline{b}$, or $\overline{g}$) is required. Isolated quarks have never been observed in nature, which leads to the idea that all physical states must be colourless. Most importantly, QCD requires the gluon to carry a net colour charge, in order to enable colour exchange between quarks. For example, a blue quark may change into a red quark, by exchanging a blue anti-red gluon

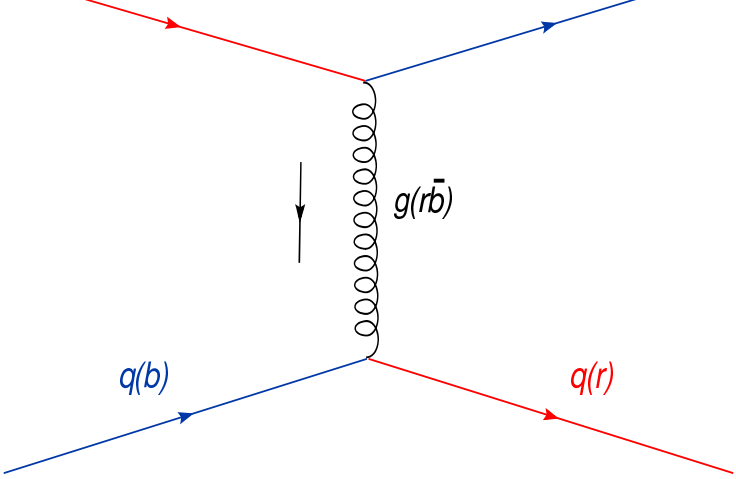

Figure 1.4: According to QCD, quarks change colour when they interact by exchanging coloured gluons.

with a neighbouring quark as shown in Figure 1.4.

Particles with constituent strange quarks, such as the Λ were found to be heavier than those which contain just u and d quarks, indicating that quarks of different flavour do not have the same mass. Heavier quarks have been made in high energy particle collisions and to date six flavours of quarks have been confirmed as existing in nature. In addition to the ones postulated by Gell-Mann, these are charm (c), bottom (b) and top (t), listed in Table 1.1.

The current theory of fundamental particles is called the Standard Model, which describes the strong interaction between quarks and gluons, and also describes the combined theory of the electromagnetic and weak interactions. In the standard model the entire material world consists of 24 matter particles comprising six quarks and six leptons, and

Name	Constituent Mass (MeV)	Bare Mass (MeV)	Charge(e)	Quantum Number
Up(u)	$\sim$310	$1.5 \rightarrow 5$	$+\frac{2}{3}$	-
Down(d)	$\sim$310	$5 \rightarrow 9$	$-\frac{1}{3}$	-
Strange(s)	$\sim$500	$80 \rightarrow 155$	$-\frac{1}{3}$	Strangeness = -1
Charm(c)	$\sim 1,600$	$1000 \rightarrow 1400$	$+\frac{2}{3}$	Charm = +1
Bottom(b)	$\sim 4,500$	$4000 \rightarrow 4500$	$-\frac{1}{3}$	Bottom = -1
Top(t)	$\sim 175,000$	174 300 $\pm$ 5 100	$+\frac{2}{3}$	Top = +1

Table 1.1: A summary of the properties of the 3 families of quarks taken from [7]. Each of the quarks listed in the above table has an associated anti-quark.

1.2 Confinement

The fact that gluons carry colour leads to some crucial differences between QCD and the analogous theory of the electromagnetic interaction, Quantum Electro-Dynamics (QED). In QED the potential between two test charges, separated by a distance r is given by,

$$V(r) = \frac{\alpha_{em}(r)}{r} \tag{1.1}$$

where α_{em} is the electromagnetic coupling 'constant'.

In QED it is postulated that an isolated electron is surrounded by many virtual e^+e^- pairs. Such virtual pairs will be polarised due to the presence of the electron. In this manner the vacuum acts like a dielectric medium, shielding the charge of the electron from a test charge. The electromagnetic coupling 'constant' therefore varies weakly with r, and may be regarded as a running coupling constant.

In QCD gluon-gluon pairs can exist in addition to the $q\overline{q}$ pairs. An individual quark is surrounded by $q\overline{q}$ pairs, which are analogous to the e^+e^- pairs in QED, and also have a screening effect on the quark's colour charge. However the gluon pairs, which carry a net colour charge, are more common than the quark loops and have an anti-screening effect. The overall effect is for there to be net anti-screening of the colour charge. The net colour charge observed by a test charge is therefore found to decrease as its distance to the real quark decreases.

The strong coupling constant has been experimentally measured to be a strongly varying function of distance or Q^2 of the form [8],

$$\alpha_s(Q^2) = \frac{12\pi}{(33 - 2n_f)\ln\left(\frac{Q^2}{\Lambda_{QCD}}\right)} \tag{1.2}$$

where Q^2 = -q^2 (q is the momentum transfer and is inversely proportional to r), n_{f} is the number of quark flavours, and Λ_{QCD} is a constant. The behaviour of α_s is crucial to understanding the nature of confinement, as unlike α_{em}, the value of α_s varies very

At high $Q^2 (\gg \Lambda_{\mathrm{QCD}})$, $\alpha_s < 1$, and the inter-quark force may be considered similar to a QED like one. At low Q^2 $(\sim \Lambda_{\mathrm{QCD}})$ $\alpha_s \gg 1$, and gluon self-interaction becomes the predominant process when considering the force between two quarks. At large distances, the gluons interacting between two quarks will attract each other. Consequently, the potential between 2 quarks may be considered as the sum of a coulomb like, $1/r$ type term, and a term which is linear in r, as given by,

$$V_s = \frac{-\frac{4}{3}\alpha_s}{r} + \kappa r \tag{1.3}$$

.

where α_s is the strong coupling constant, κ is the string constant ($\sim$ 1 GeV/fm) and r is the separation of the quarks [9].

At low Q^2, as $r \to \infty$, $V_s \to \infty$; this explains why free partons are not observed in isolation. However at high Q^2 or small r, $\alpha_s \to 0$ faster than r itself, causing the interaction potential to drop to zero in this high Q^2 (low r) regime.

The Λ_{QCD} constant, referred to in equation 1.2 is regarded as defining the scale of the strong interaction, and has been measured to be $\sim$ 200 MeV [10]. It is important as effectively it differentiates between a system of confined hadrons, and a system where the partons no longer feel the strong force ($Q^2 \gg 200$ MeV). The latter state corresponds to the asymptotically free regime where the separation of the partons is $\ll$ 1fm with $\alpha_s \to 0$. It has been suggested that an asymptotically free system of quarks and gluons may be described as an ideal gas of partons, with thermo-dynamical properties such as temperature and pressure [11]. It was the notion of a thermally equilibrated asymptotically free system of partons that first led to the idea that a Quark-Gluon Plasma (QGP) may exist.

1.3 Debye Screening

A different route to the creation of a Quark-Gluon Plasma is predicted if one considers the mechanism of Debye screening [12], which can be understood by examining an analogous

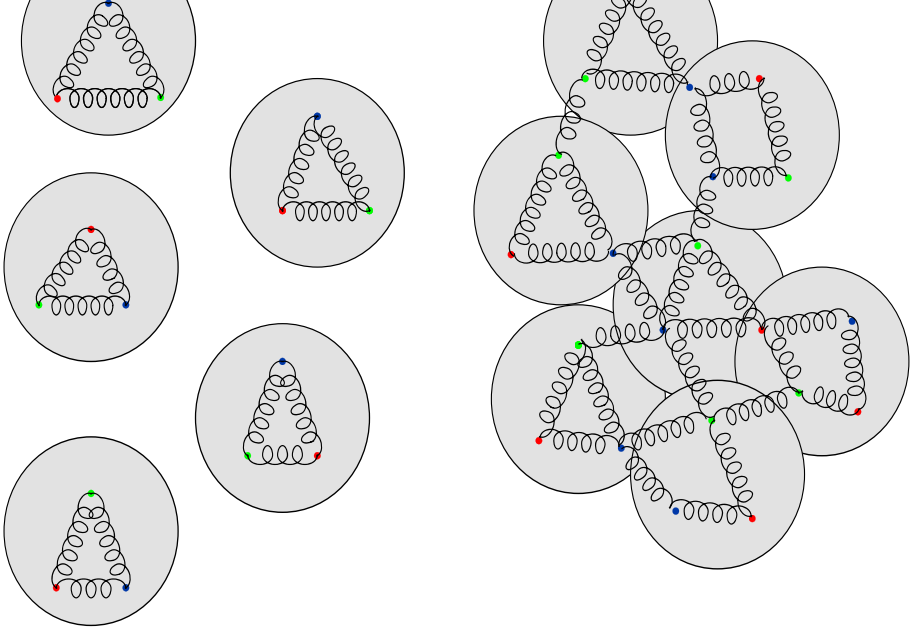

Figure 1.5: If the energy density of normal hadronic matter (a) is increased sufficiently, hadron boundaries will begin to overlap (b). As quarks and gluons become de-localised throughout this extended medium, Quark-Gluon matter is formed.

process in condensed matter. If one considers the hypothetical case of an array of hydrogen atoms, in an insulating state, then each electron is bound to its proton by the Coulomb interaction. However an electron is not only attracted to its atomic proton, but also to neighbouring protons. This has the effect of modifying the potential between the electron and its proton to give,

$$V(r) = \frac{-\mathrm{e}^2}{4\pi\epsilon_0 r} \exp(\frac{-r}{R_D}) \tag{1.4}$$

where the electron binding radius is r, and the Debye screening radius, R_D is related to the number density of atoms, N_D by,

$$R_D \sim \frac{1}{\sqrt[3]{N_D}} \tag{1.5}$$

As the number density is increased, R_D becomes smaller than the electron binding radius, and the exponential term in equation 1.3 tends to zero. The electrons become de-localised, turning the insulating array of atoms into an electrical conductor.

In QCD the Debye screening radius should also decrease with the parton number

by their neighbouring nucleons. This represents the transition of a colour insulator into a colour conductor, as the coloured partons become free to propagate throughout an extended volume, as shown in Figure 1.5. The process of Debye screening is important for calculating the conditions necessary for deconfinement, as it occurs at much lower energy densities than those required for an asymptotically free plasma [13].

1.4 The Phase Diagram of Nuclear Matter

Clues as to how a Quark-Gluon Plasma may exist are given by astro-physical observations. For example modern theories of super-dense nuclear matter predict that a neutron star may have a net baryon density of 3 to 5 times that of nuclear matter, which may be sufficient for the QGP to exist [14].

The measurements of cosmic background radiation and of the cosmological red shift, suggest that the universe is expanding and has been cooling since the big bang. The state of matter in the early universe is utterly different to that of a neutron star, because it would have consisted of nearly equal amounts of very hot matter and anti-matter, forming a high temperature, low net baryon number plasma.

The critical temperature, T_c above which the early universe may have consisted of a Quark-Gluon Plasma, can be calculated by using Lattice QCD [15],[16]. Lattice QCD calculations indicate that T_c is between (154 ± 8) MeV and (173 ± 8) MeV [17]. These temperatures correspond to energy densities of between ~ 0.8 GeV/fm^3 and ~ 1.4 GeV/fm^3. Using these temperatures, it is predicted that when the universe was less than 10 μs old it was hot enough and dense enough to be composed of deconfined quark gluon matter [18].

It is useful therefore to characterise Quark-Gluon and hadronic matter in terms of temperature, T and the net baryon density [19]. The state of nuclear matter may be described by a phase diagram in the plane of T and net baryon density, where its two phases are hadronic or nuclear matter and Quark-Gluon Matter as shown in Figure 1.6.

The QGP phase transition is expected to coincide with a partial restoration of Chiral

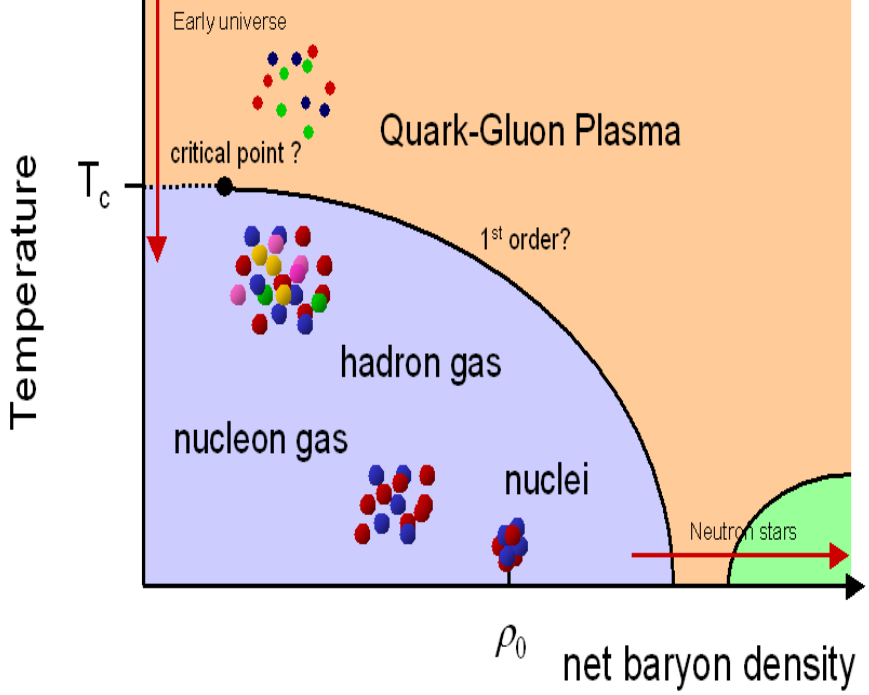

Figure 1.6: The Phase diagram of nuclear matter.

symmetry. This is important as the mass of the quark effectively has two parts, the first part of which is the intrinsic 'bare mass' which comes from the quark's interaction with the Higgs field, and a second part due to the quarks interaction with its surrounding medium. A partial restoration of Chiral symmetry is believed to reduce the latter quark mass contribution to zero, leaving only the bare quark mass. Consquently less energy is required to produce new quark anti-quark pairs in the QGP scenario, than in a hadron gas.

1.5 Kinematics of Relativistic Heavy Ion Collisions

The best prospects for creating a terrestrial Quark-Gluon Plasma are in the study of relativistic heavy ion collision experiments. Such experiments have been performed since 1986 at the Alternating Gradient Synchrotron (AGS), and are presently being conducted at the CERN Super Proton Synchrotron (SPS) and at the Relativistic Heavy Ion Collider (RHIC) at Brookhaven National Laboratory. One of the main distinguishing features between these experiments is the energy content available to the nuclear collision, repre-

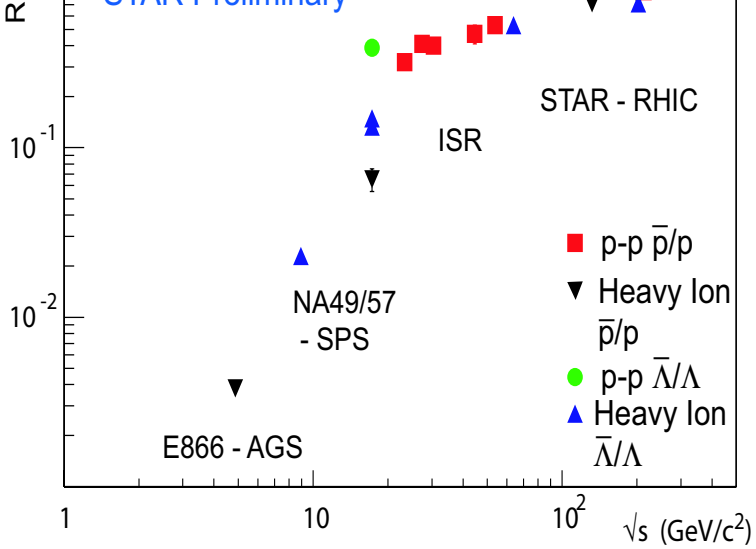

Figure 1.7: A plot of anti-baryon to baryon ratios for proton+proton and heavy ion data as a function of centre of mass collision energy ($\sqrt{s}$). Taken from [20].

sented by the centre of mass collision energy, $\sqrt{s}$.

Experiments at the SPS and the AGS involved colliding a beam onto a fixed target, where as at RHIC two synchrotron beams are made to collide. Therefore when comparing results between experiments the longitudinal component of momentum, p_l is inconvenient as it depends on the velocity of the centre of mass frame with respect to the lab frame. Spectra of particles produced in relativistic particle collisions are presented as functions of the transverse component of momentum, p_T, within a certain rapidity acceptance, where rapidity, y, is defined as,

$$y = \frac{1}{2} \ln \left(\frac{E + p_l}{E - p_l} \right) \tag{1.6}$$

where E is the beam energy. A summary of the maximum beam energies, $\sqrt{s}$ and beam rapidities available at the AGS, SPS, RHIC and that planned for the LHC is shown in Table 1.2. The mid-rapidity region, y_{mid}, is important as it is here that the number of newly created particles is largest, and so is the window of rapidity that most RHI experiments tend to focus on. As rapidity is Lorentz additive the mid-rapidity regions for all the collisions indicated in Table 1.2 are comparable.

Rapidity is mass dependent, and often, particularly when quoting detector acceptances

as,

$$\eta = \frac{1}{2} \ln \left(\frac{p + p_l}{p - p_l} \right) \tag{1.7}$$

Facility Name	Max. Beam Energy(GeV/A)	$\sqrt{s}$ (GeV/A)	$\Delta y/2$	y_{mid}
AGS	11	4.6	1.6	1.6
SPS	158	17.2	3.0	3.0
RHIC	100	200	5.4	0
LHC	3500	7000	8.8	0

Table 1.2: A summary of the maximum beam and centre of mass collision energies for heavy ions at RHI facilities.

As shown in Figure 1.7, as the centre of mass collision energy increases, the net baryon density of the system decreases, with the number of baryons and anti-baryons created at mid-rapidity at $\sqrt{s} = 200$ GeV being approximately equal. At RHIC energies, roughly equal numbers of baryons and anti-baryons are produced and the net baryon density is approximately zero. Thus fireballs created in RHIC collisions are in the low net baryon density, high temperature regime of the phase diagram displayed in Figure 1.6.

Out of the many heavy ion events measured by experiments, the most 'central' are most likely to produce a fireball with sufficient energy density to make a QGP. Centrality is related to impact parameter, as discussed in Appendix A. The energy density, assuming a central collision and zero net baryon density at mid-rapidity is given by Bjorken [21],

$$\varepsilon(\tau) = \frac{1}{\tau \mathcal{A}} \frac{dE_T}{dy}\bigg|_{y=0}, \tag{1.8}$$

where $\mathcal{A}$ is the transverse area of the incident nuclei and τ is the formation time (assumed to be 1fm/c - the time for light to traverse a nucleon). E_T is transverse energy and is a measured quantity.

The enhancement of strangeness as a Quark-Gluon Plasma signature was originally suggested by Rafelski [22]. Rafelski proposed that $s\overline{s}$ pairs will be easier to produce in the QGP than in a hadronic gas, both because they are much lighter due to paritial chiral symmetry restoration and because of the much higher density of gluons, which opens up new formation processes such as gluon fusion ($gg \rightarrow s\overline{s}$). Perhaps more importantly the time taken for strangeness equilibration via strong interactions (eg gg, qg, $q\overline{q}$) in a QGP should be less than for a purely hadronic scenario [23]. The increased production of strangeness should manifest itself as an increase in the produced numbers of strange particles and anti-particles, such as the singly-strange Λ, the doubly-strange Ξ and the triply-strange Ω.

Of course, when considering enhancement of strangeness in heavy ion collisions, one has to consider also a control measurement to which strange yields from heavy ion collisions can be compared. The CERN NA57 and WA97 experiments measured yields of strange particles from collisions of lead on lead for which a maximum energy density of 3.2 GeV/fm^3 was achieved, above that predicted for a QGP [24], [25]. The CERN experiments also measured strange yields from collisions of protons on Beryllium and protons on lead, which form the control measurements. Pb + Pb collisions will naturally produce more particles than collisions of lighter ions, due to the fact that usually Pb + Pb collisions contain more participating pairs of nucleons than either p + Be or p+Pb collisions. Therefore strange yields are usually normalised by the number of participating pairs of nucleons which will vary according to the centrality of the event. The number of participant pairs is estimated using Glauber Monte Carlo Models (See Appendix A). Strangeness enhancement may be defined as,

$$Enhancement = \frac{\left(\frac{Yield}{N_{part}}\right)_{A+A}}{\left(\frac{Yield}{N_{part}}\right)_{CONTROL}} \tag{1.9}$$

where A+A represents the heavy ion system (Pb + Pb for NA57), *control* represents the control measurement (either p + Be, or p+Pb for NA57) and N_{part} is the number of participating nucleons, which varies as a function of collision centrality. Figure 1.8

centrality [25]. In Figure 1.8 enhancement is measured relative to p + Be collisions, and strangeness is shown to be enhanced for all hyperons shown in the Figure. Significantly, the enhancement is in hierarchical order of strangeness content, with $\Omega^- + \overline{\Omega^-}$ enhanced by an order of magnitude. This discovery of strangeness enhancement was one of the pieces of evidence mentioned in the CERN press statement of 2000, claiming compelling evidence for the discovery of the QGP.

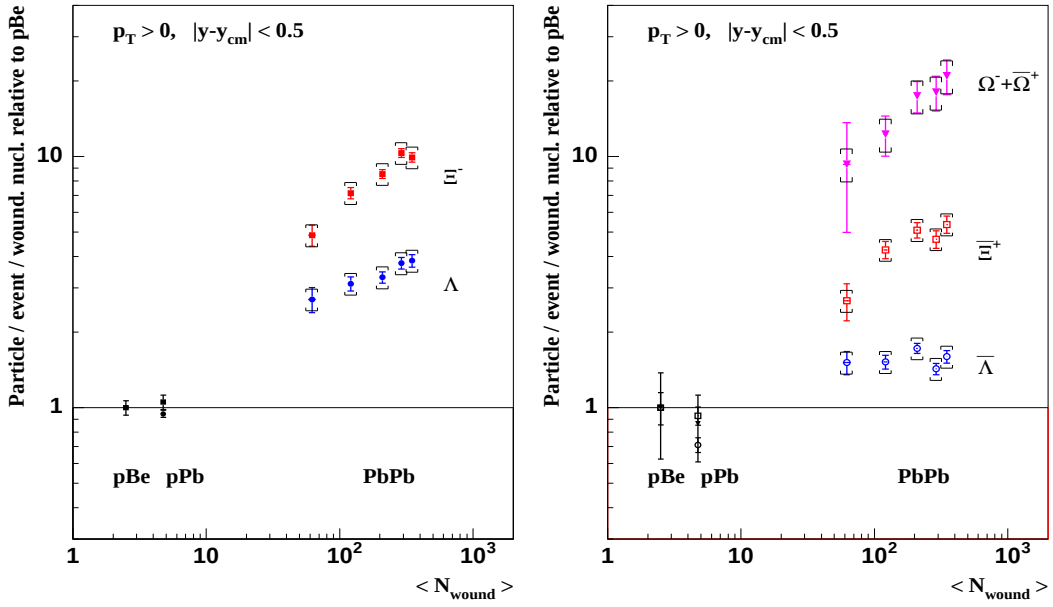

Figure 1.8: Strangeness enhancement factors, as a function of mean number of participating nucleons (N_{wound}=N_{part}), as measured by the NA57 experiment at CERN at $\sqrt{s}$ = 17.2 GeV (Figure taken from [87]).

The Solenoidal Tracker at RHIC (STAR) experiment began taking its first data in 2000, and during its second run (2001-2002) measured both Au + Au collisions and p + p collisions at $\sqrt{s} = 200$ GeV. The PHENIX collaboration have measured the energy density for Au + Au collisions at $\sqrt{s} = 200$ GeV to be 5.4 ± 0.6 GeV/fm^3 [26], this is well above the critical ϵ for a QGP phase transition, determined by the lattice QCD calculations. The p + p collisions act as the control or baseline measurement, acting in a similar role as the p + Be collisions in the NA57 experiment.

However, although RHIC was the first experiment to collide heavy nuclei with centre of mass energies of 200 GeV, there are other similar p + $\overline{\text{p}}$ collider facilities such as the Super

the mid-rapidity regime at RHIC is net-baryon number free, it is reasonable to assume that measured yields in $p + p$ collisions at $\sqrt{s} = 200$ GeV will be similar to those from $p + \overline{p}$ at the same energy. Indeed proton and anti-proton yields from $p + p$ and $p + \overline{p}$ collisions have been compared directly at a lower energy of $\sqrt{s} = 53$ GeV, and were found to be similar [27].

There are good reasons for RHIC experiments to make their own $p + p$ measurement. The rapidity acceptance for Λ,$\overline{\Lambda}$ and K^0_S of the STAR detector is limited to -1 $< y <$ 1, where as strange particle results, from for example, the UA5 experiment are quoted over larger rapidity intervals. Any conversion to make the STAR heavy ion results cover the UA5 rapidity interval would be model dependent. The statistics available to some of the earlier $p + \overline{p}$ work, particularly the strange particle UA5 results were also poor, with large errors being quoted on the final yields [28]. Also UA5 was unable to distinguish between strange particles and anti-particles.

The objective of the work described herein is to measure singly strange particles (Λ, $\overline{\Lambda}$ and K^0_S) from $p + p$ collisions at $\sqrt{s} = 200$ GeV at RHIC. One of the purposes of this is to extract the yields (dN/dy) in order to determine the strangeness enhancement factors, relative to Au+Au collisions for Λ and $\overline{\Lambda}$. However, the spectra can also be used to help verify and tune various models and calculations, some of which are discussed in the following Chapter.

Chapter 2

Theory

If comparisons are to be made to results from heavy ion collisions it is important to understand the baseline p + p measurement. Unfortunately although the theory of QCD is well established, it cannot be used to give a complete description of particle production from nuclear collisions. This section describes some of the models which have been formulated in an attempt to describe particle production in proton + proton (p + p) and also proton + anti-proton (p + $\overline{\text{p}}$) collisions. Also described are some of the earlier p + $\overline{\text{p}}$ experimental results, together with some of the model comparisons.

2.1 Microscopic Models

2.1.1 Hard Processes

Evidence for the form of the potential between two quarks given in equation 1.3 is provided by the observation of high p_T jets from high energy collisions [29]. As such events involve very high momentum transfers the strong coupling constant α_s is less than unity, allowing perturbation theory to be used to calculate the cross-cross section.

hard processes into 3 separate contributions. Taking, for example, the inclusive reaction $A + B \rightarrow C +$ anything, where A, B and C are hadrons, the contributions are:

1) The initial state interaction is between two quarks, a and b belonging to hadrons A and B. This initial interaction is linked to the momentum distributions of the quarks within the hadrons, represented by the structure functions $G_{a/A}(x_a, a_T)$ and $G_{b/B}(x_b, b_T)$. Here a_T and b_T represent the transverse momenta of partons a and b (which are constituents of A and B), and x is the Bjorken x variable defined by,

$$x = \frac{q^2}{2M\nu} \tag{2.1}$$

where q is the 4 momentum transfer, M is the mass of the proton and ν is the energy transferred to the proton. Bjorken x is a measure of the inelasticity of the collision, and for a totally elastic collision it is equal to 1.

2) The Feynman diagram for the quark-quark scattering, $a+b \rightarrow c+x$ where x can be anything. From the Feynman diagram, and knowledge of the strong coupling constant, α_s, the cross section for the partonic scattering processes, $a+b \rightarrow c+x$ can be evaluated.

3) The chance for quark c to fragment into a hadron of type C, $G_{C/c}$. Fragmentation is a poorly understood process, as all fragmentation takes place at large r, ($\alpha_s > 1$). Therefore jet fragmentation functions are empirically derived from experimental data [30].

A simplified cross section calculation can be written as,

$$\frac{\mathrm{d}\sigma}{\mathrm{d}y} = \sum_{abc} \int_0^1 G_{a/A}(x_a, a_T) G_{b/B}(x_b, b_T) \frac{\mathrm{d}\sigma_{ab\rightarrow cx}}{\mathrm{d}y} \frac{G_{C/c}(x_c, c_T)}{x_c} \mathrm{d}x_a \mathrm{d}x_b \mathrm{d}x_c \tag{2.2}$$

These types of equations have been successfully used to describe jet production at the Tevatron [31]. Attempts have also been made to describe particle spectra (not just jets) using pQCD models. The UA1 K^0_S spectra at $\sqrt{s} = 630$ GeV [32], and K^0_S spectra from the Collider Detector at Fermilab (CDF) [33] are plotted in Figure 2.1. Also shown are 3 parameterisations of a next to leading order pQCD calculation by Borzumati et al. [34]. The calculation made by Borzumati agrees well with the 630 GeV spectra for $p_T > 2$ GeV,

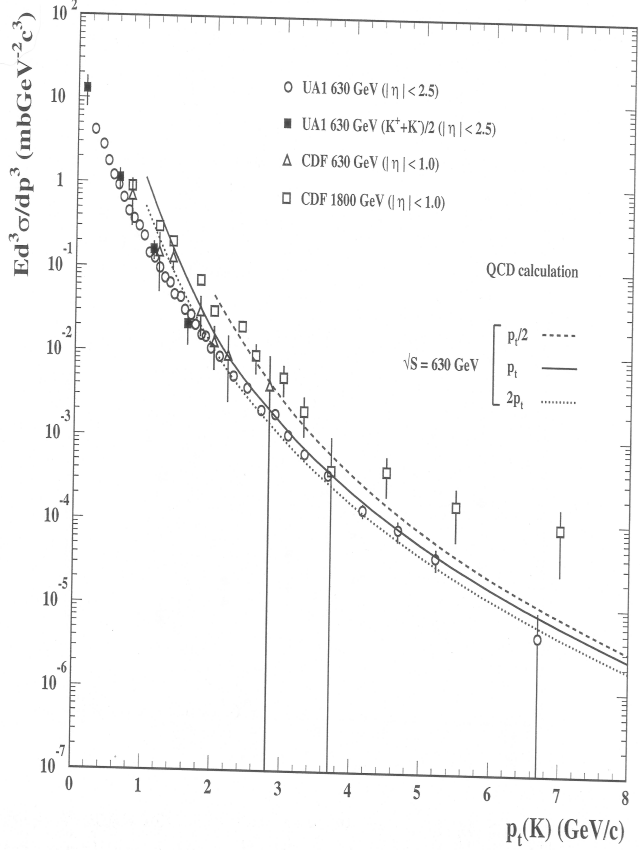

Figure 2.1: A comparison of K^0_S and $K^{\pm}$ spectra as a function of p_T from UA1 [32] and CDF [33]. The fitted lines are pQCD calculations made by Borzumati, which describe the UA1 data well at high p_T.

but is not expected to agree at low p_T, as particle production at low p_T is dominated by non-pQCD (soft) processes. As stated by Hagedorn [35], the spectral shape at high p_T becomes flatter, and an empirical power law function (equation 2.3) is expected to fit the high p_T part of the spectra where the power law is defined as,

$$E\frac{d^3N}{dp^3} = \frac{1}{2\pi p_T}\frac{d^2N}{dydp_T} = B(1+\frac{p_T}{p_0})^{-n} \tag{2.3}$$

where n (the power factor), B and p_0 are fit parameters. The power law parameterisation is widely used to describe K^0_S and π spectra from high energy $\mathrm{p}+\overline{\mathrm{p}}$ and $\mathrm{p}+\mathrm{p}$ collisions (see for example [36]).

Calculations involving QCD perturbation theory are very complicated (see for example [37]) and cannot be expected to agree at low p_T. Also pQCD calculations cannot be used to

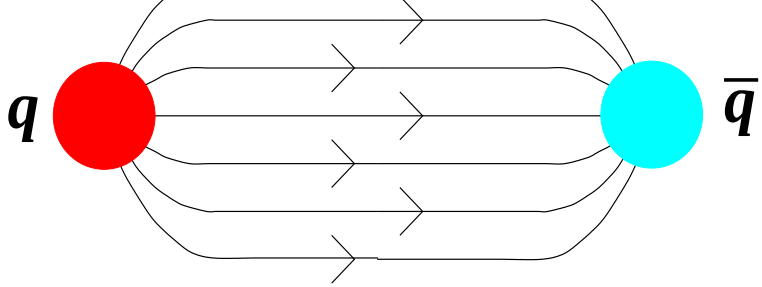

Figure 2.2: Over large distances the gluons attract each other and form a 'flux tube'. This is in contrast to QED, as the field lines do not spread out to form a dipole pattern.

describe the underlying event in hadron hadron collisions, which is essentially everything else except the outgoing particles from the hard scatter.

2.1.2 Soft Processess

The features of p + p and p + $\overline{\text{p}}$ collisions at lower energies ($\sqrt{s} < 1$ TeV) are dominated by small q^2 collisions, where $\alpha_s > 1$. Therefore unfortunately, the majority of particles generated in collisions at RHIC energy ($\sqrt{s} = 200$ GeV) and below, are produced in collisions where pQCD is not applicable. It has so far proved impossible to calculate from first principles the low p_T part of particle spectra produced from such 'soft' collisions.

This is why a phenomenological approach has to be applied in the analysis of particles produced in soft collisions. One of the most commonly used models is the Lund string model [38]. The string model is a semi-classical model, based on the observation that the colour field between two colour charges does not extend radially throughout space, like for two electromagnetic charges. Instead, because of the self interaction of the gluons the field is concentrated into a colour flux tube, as illustrated in Figure 2.2. The tube has a constant linear energy density of $\kappa \sim 1$ GeV/fm, thus the potential energy between the colour charges grows with distance [39]. If the distance becomes too large the tube will break by the production of a $q\overline{q}$ pair from the field energy, producing two new strings. Each string fragments into hadrons, breaking up repeatedly, as long as the invariant mass of the string pieces exceeds the mass of a hadron.

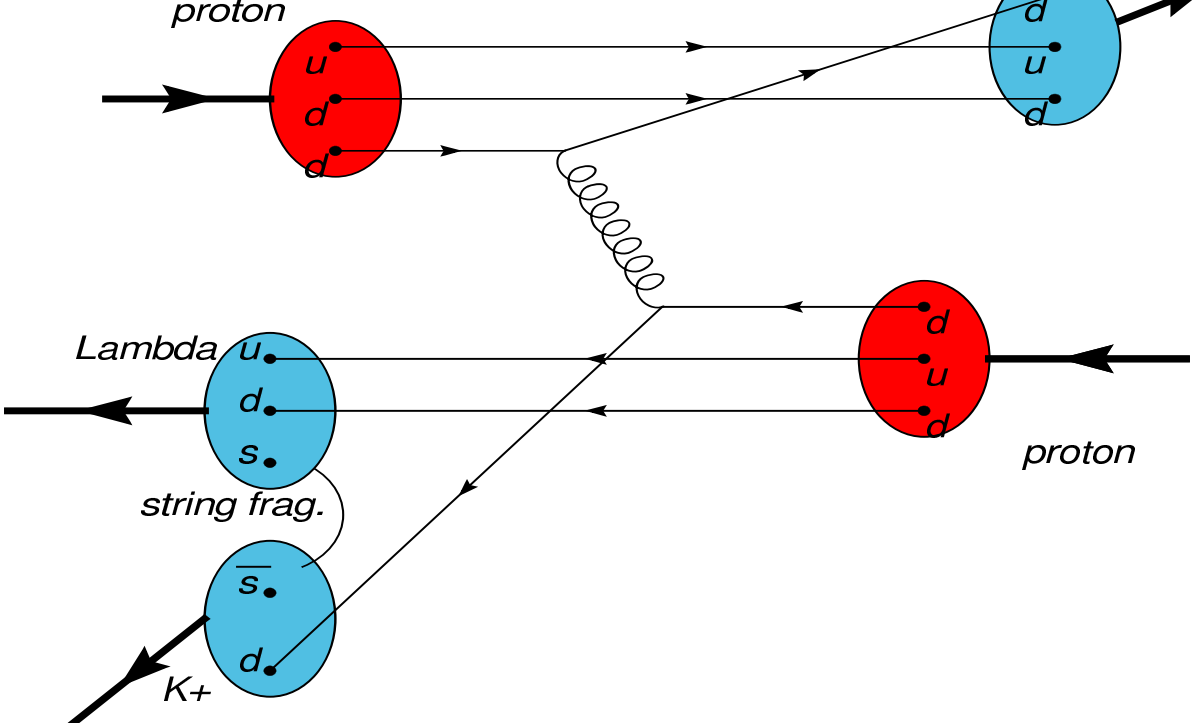

Figure 2.3: Schematic diagram of the string fragmentation process. A d-quark + d-quark collision occurs between the two red protons, resulting in a string being pulled between the separated (ud) di-quark and a d quark, (formally the lower udd proton in the diagram). In the example shown, the string fragments into a $s\overline{s}$ pair, creating 3 new final state particles (blue), a proton, a Λ and a K^0_S. If the collision is sufficiently violent, the string may fragment into much more than one $q\overline{q}$ pair.

A simple example of Lund string fragmentation is given in Figure 2.3, where the process,

$$p + p \rightarrow p + \Lambda + K^+. \tag{2.4}$$

is described at the level of the constituent quarks.

In the Lund string model the probability for creating the $q\overline{q}$ pairs decreases exponentially with the transverse mass squared, m_T^2 of the $q\overline{q}$ system, where the transverse mass is defined as,

$$m_T{}^2 = m^2 + p_T{}^2 \tag{2.5}$$

d quarks, with for example strange quark production estimated to be three times less likely than u or d quark production [38].

There are event generators such as PYTHIA [40] and HIJING [41] which describe production of particles via the strong interaction using a Monte Carlo model. As well as being based on the Lund model, they incorperate leading order pQCD calculations for the hard parton-parton scattering process. Collisions are simulated many times in order to build up sufficient statistics to enable a comparison with experimental data.

However, such event generators are also controlled by a series of adjustable parameters. The default PYTHIA parameters correspond to those which achieve good agreement with high energy e+e- collision data. The parameters can be further tuned, for example, in order to make the minimum-bias charged particle spectra from $\mathrm{p} + \overline{\mathrm{p}}$ collisions at $\sqrt{s} =$ 546 GeV agree with PYTHIA [42]. Interestingly a parameter which provides multiple parton-parton collisions needs to be incorporated to achieve the agreement. This backs up earlier experimental observations (for example [43]), that for $\sqrt{s}$ greater then a 100 GeV or so, collisions between protons and anti-protons largely consist of more than a single parton-parton interaction.

2.2 Proton + Proton ($\mathrm{p} + \mathrm{p}$) and Proton + Anti-proton ($\mathrm{p} + \overline{\mathrm{p}}$) Collisions

There is a wealth of $\mathrm{p} + \mathrm{p}$ and $\mathrm{p} + \overline{\mathrm{p}}$ data from collisions with $\sqrt{s}$ from a few GeV, to $\sim$ 2 TeV [33]. Much of the data concerns the measurement of pions, or other light mesons, since these are the most copiously produced particles in relativistic collisions. Such data, including those from the comparatively rarer strange particle analyses, can then be used to help tune models such as PYTHIA, and help improve our understanding of the strong force.

At CERN Intersecting Storage Rings (ISR) energy regions ($\sqrt{s} \leq 65$ GeV) a number of features of hadronic collisions are observed to have scaling properties such as constant

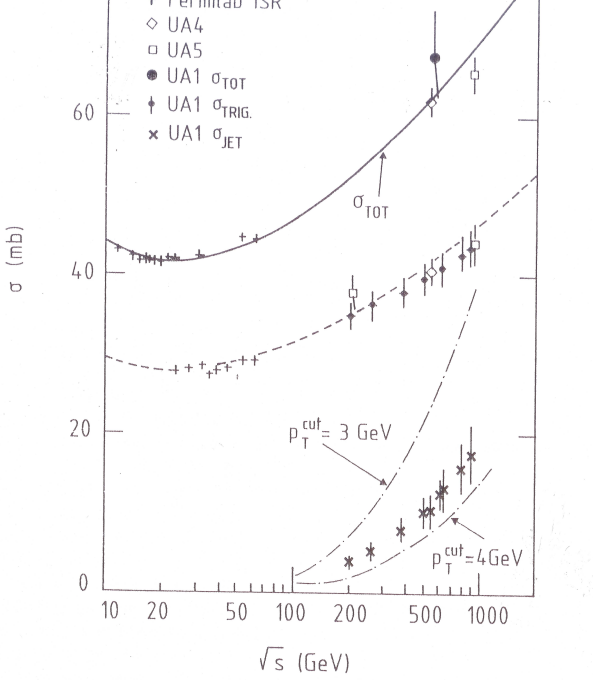

Figure 2.4: The UA1 trigger cross section σ_{trig} as a function of $\sqrt{s}$. The fitted line is consistent with the conclusions of Gaisser and Halzen and L. Durand and H. Pi, that the observed rise in the inelastic cross section may be associated with the jet event cross section. (Taken from [45]).

$\langle p_T \rangle$ and total cross section, σ_{tot} [44]. As $\sqrt{s}$ is increased beyond 65 GeV one of the phenomena encountered is the increase of the inelastic cross section σ_{tot}, with $\sqrt{s}$ of $\mathrm{p} + \overline{\mathrm{p}}$ collisions, as indicated in Figure 2.4. One explanation for this behaviour is presented by Gaisser and Halzen [46], where, due to the difficulties in calculating non-pQCD cross sections, σ_{tot} is split into two components,

$$\sigma_{tot} = \sigma_0 + \sigma_{jet}(p_{Tmin}) \tag{2.6}$$

where σ_0 is the $p + \overline{p}$ cross section at low energy and $\sigma_{jet}(p_{Tmin})$ is calculated using pQCD. The calculated value of σ_{jet} increases with $\sqrt{s}$, indicating that the increasing cross section may be described by an increasing contribution from a hard, pQCD based component. This simple model has since been refined [47], but the basic conclusion remains that the overall cross section can be described by soft and hard components, with the pQCD component increasing with $\sqrt{s}$.

in $p + \overline{p}$ collisions, observed at Fermilab for $\sqrt{s} = 1.8$ TeV for charged kaons, pions and protons [33] and also for $(\Lambda + \overline{\Lambda})$ and K^0_S at $\sqrt{s} = 630$ GeV, measured by the UA1 collaboration (see Figure 2.5)[32]. The dependence is interesting, because a naive expectation might be for there to be less kinetic energy available to the particles, as more of the collision energy has been used in creating new particles (increased multiplicity). Wang and Hwa have used a semi-empirical model to reproduce the increase of $\langle p_T \rangle$ with charged multiplicity [48]. This model indicates that the increase of $\langle p_T \rangle$ is related to a growing contribution from particles produced by so called 'mini-jets'. A mini-jet is produced from semi-hard events involving parton scatters which can be treated perturbatively, but which do not produce jets of particles with $p_T > 5$GeV. Instead these high q^2 scatters produce 'mini-jets' of particles with p_T between approximately 1 and 5 GeV. Using this model Wang also shows that the increase of mean multiplicity with $\sqrt{s}$ can be explained by a growing mini-jet contribution [49]. At RHIC energies and lower the model indicates that particle production is dominated by the soft processes and is able to reproduce the slow logarithmic increase of mean particle multiplicity with $\sqrt{s}$ seen in the data [50]. The multiplicity contribution from the pQCD mini-jet processes rises much more quickly with $\sqrt{s}$, but does not become dominant until $\sqrt{s} > 4$TeV [49].

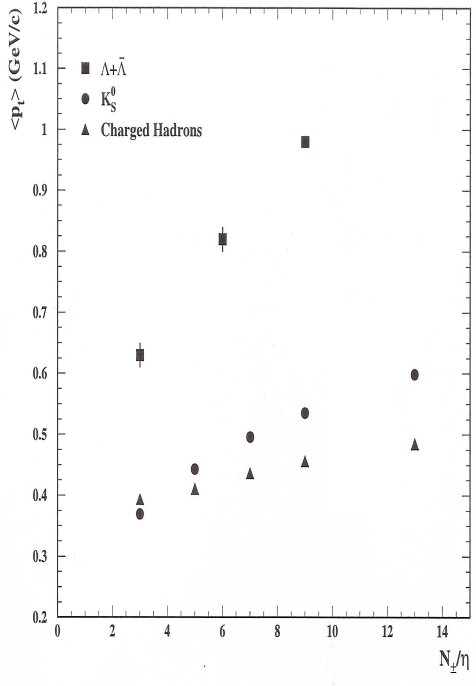

Figure 2.5: $\langle p_T \rangle$ as a function of charged track multiplicity per unit pseudo-rapidity for charged hadrons, K^0_S and $\Lambda + \overline{\Lambda}$, as measured by the UA1 experiment [32].

A model by Giovannini and Ugoccioni describes the multiplicity distributions in terms of a weighted superposition of the multiplicity distributions from soft events and semi-hard events (events with mini-jets), where the semi-hard component is characterised by larger mean multiplicity [51]. Their results indicate that particle production is dominated by hard pQCD processes in the $\sqrt{s} \sim$ TeV region, but by soft non-pQCD processes in the $\sqrt{s} \sim$ GeV region and therefore are consistent with the conclusions by Wang and his collaborators.

These observations provide evidence for contributions from two separate components to spectra from p + p and p + $\overline{\text{p}}$ collisions; a soft non-pQCD component and a hard pQCD component, with the hard part part increasing both with $\sqrt{s}$ (resulting in an increase in cross section), and also with the measured multiplicity.

Where as microscopic models such as a pQCD calculation or a PYTHIA simulation attempt to model particle interactions in detail, thermal models can be used to predict simpler characteristics, such as the overall yield, dN/dy for individual particles, or chemical freeze out temperature. Generally statistical models assume a thermally and chemically equilibrated system where all inelastic processes have ceased but make no predictions about how the system arrived in such a state, or for long the system lives for.

2.3.1 Thermalisation and the QGP

The Quark-Gluon Plasma has been defined as [53],

> 'A (locally) thermally equilibrated state of matter in which quarks and gluons are deconfined from hadrons, so that colour degrees of freedom become manifest over nuclear, rather than merely nucleonic volumes.'

The question of whether the system created in nuclear collisions is relevant not just in determining the applicability of thermal models, but also in deciding if the Quark-Gluon Plasma exists, and is therefore worth attempting to answer.

If one assumes that a Quark-Gluon Plasma is produced in relativistic heavy ion collisions, then the system may be considered as evolving over time. This evolution starts with the initial state interactions between the individual constituent partons, within the heavy nuclei. The number of partons increases rapidly as new partons are created via fragmentation processes. If the energy density is large enough it is believed that the matter created in such collisions could undergo a phase transition to a new deconfined state known as the Quark-Gluon Plasma. If this is so then, as the system is rapidly expanding, the QGP will only last a very short time before it cools and re-hadronises. One very important consideration is that whether the QGP lives long enough in order for equilibrium to be obtained. Indeed, as new types of quark, such as strange quarks and anti-quarks are produced in the collisions, there are infact two types of equilibrium relevant: thermal equilibrium and chemical equilibrium. The factors governing whether these two types of

Quark-Gluon plasma lives for.

Thermal equilibration takes place via both elastic and inelastic collisions between gluons and quarks. A model by Biro et al., which uses a pQCD based Monte Carlo model to predict the strong interactions between partons is able to determine the time it takes for a purely partonic system to reach thermal equilibrium [54]. It is predicted that the QGP is dominated by gluons, which have a factor of 2-3 larger interaction cross section than the quarks; hence the gluons thermalise very quickly ($\sim 0.3 fm/c$) with the whole system thermalising after 1 fm/c.

At RHIC this initial plasma temperature is expected to be $\sim$ 300 MeV; the plasma therefore lives for as long as it takes for it to cool down to the phase transition temperature of 160 MeV. Assuming, the longitudinal expansion rate of the separating quarks and gluons, the plasma at RHIC is expected to last ≤ 10 fm/c [55].

As there are no strange valence quarks in the original heavy nuclei, they must be produced via inelastic collisions. The equilibration of strangeness occurs on a much longer time scale than thermalisation [56]. Thus even though the QGP may be in thermal equilibrium, strangeness may not be fully equilibriated.

As the system continues to expand there will come a point where there is insufficient energy for flavour changing inelastic interactions; this is known as chemical freeze out. As the system expands further, it will become sufficiently diffuse so that elastic interactions cease; this is known as thermal freeze out.

2.3.2 The Temperature Parameter

The thermodynamic approach to hadron production in hadronic collisions was originally introduced by Hagedorn [35]. The most important indication of thermal hadron production in high energy reactions was considered to be the 'slope' or temperature parameter, T of the transverse mass, (m_T) spectra, where m_T was by defined equation 2.5. However, here the parameters from equation 2.5, m and p_T relate to the mass and transverse momentum for a particular particle respectively. Assuming the hadrons exist in an infinitely

described by,

$$\frac{1}{2\pi p_T}\frac{d^2N}{dydp_T} = Am_T e^{-\frac{m_T}{T}} \tag{2.7}$$

where A is a constant. The temperature parameter, is effectively used to describe the spectral shape, which reflects not only the apparant temperature after thermal freeze out, but also the velocity of the expanding fireball.

2.3.3 Thermal Models

For systems involving large numbers of produced particles the thermal model can be considered within the context of the grand canonical ensemble. Given a set of input parameters, such as the slope parameter, T and the chemical potentials, the number density for a particular species may be calculated. A thermal model determines mean particle multiplicities, $\langle n_i \rangle$, of type i, by assuming a Boltzmann distribution of the form,

$$\langle n_i \rangle = (2J_i + 1)\frac{V}{(2\pi)^3}\int \mathrm{d}^3p \; \frac{1}{\gamma_{\mathrm{s}}^{-s_i}\exp\left[(E_i - (\mu_b + \mu_s))/T\right] \pm 1} \tag{2.8}$$

where J_i is the spin of hadron i, s_i is the number of strange quarks and the temperature, T and the chemical potentials u_b, and u_s can be regarded as free parameters. The γ_s factor was introduced by Rafelski [57] in order to account for the amount of strangeness chemical equilibration, where γ_s can be between 0 and 1, and full strangeness equilibration is represented by $\gamma_s = 1$. Some models, such as Braun-Munzinger's [58] assume complete chemical equilibration ($\gamma_s = 1$), and, initially an infinite volume. The measured mean particle yields are used as a basis to apply thermal model fits using variables such as T and u_b as the fit parameters. The success of the thermal model is in being able to tune the fit in order to agree with a number of different measured particle abundances. Good agreement is obtained between the relativistic heavy ion data and the thermal model fits using both the Braun-Munizinger approach and also the model by Becattini and Cleymans [59] (shown in Figure 2.6). At energies below 200 GeV energy γ_s is < 1, but at RHIC energies it has been shown that $\gamma_s \sim 1$ [60].

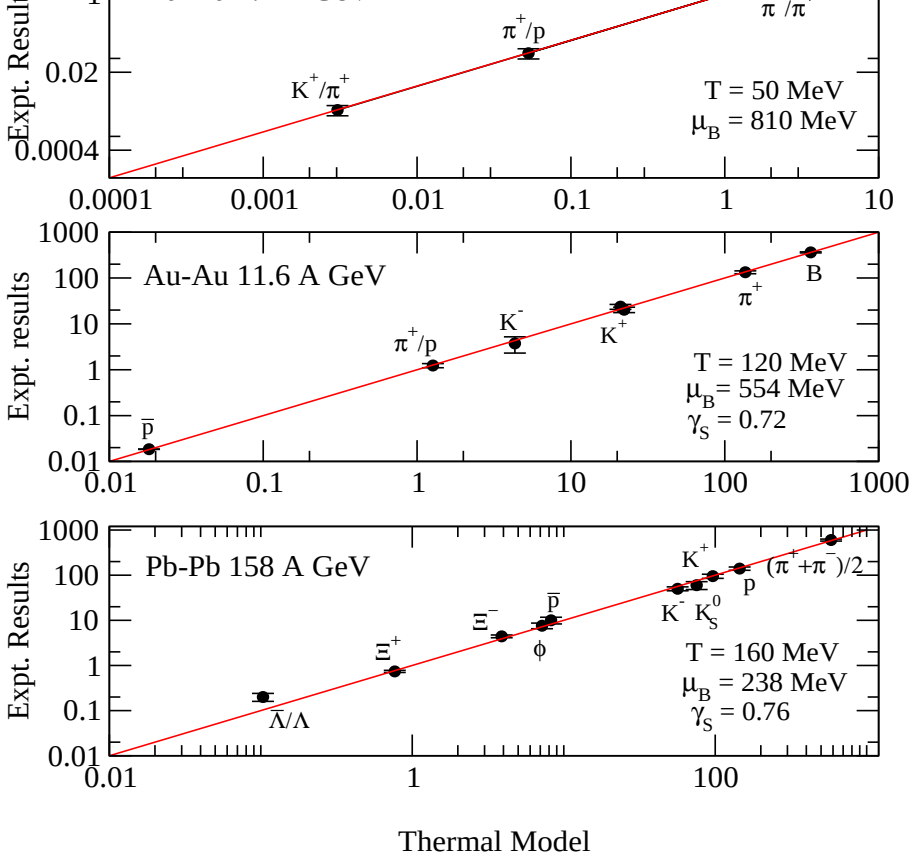

Figure 2.6: Thermal model multiplicities as calculated by Becattini and Cleymans model agree with experimentally measured yields from heavy ion collisions (with beam energies between 1.7 GeV/A and 158 GeV) well (taken from [59]).

It has therefore been shown that particle yields and ratios from the relativistic heavy ion experiments agree well with thermal model based model predictions, where the condition of complete thermal equilibration is implicit. It is important to address if this agreement is unique to just the heavy ion data. Accordingly thermal model analyses have also been conducted on results involving smaller systems (eg $\mathrm{p}+\mathrm{p}$), where a thermal system is not expected.

When thermal model type analyses are applied to results from $\mathrm{p}+\mathrm{p}$ and $\mathrm{p}+\overline{\mathrm{p}}$ it is important to point out that the number of produced particles is reduced so that the grand canonical ensemble is no longer applicable. Instead, the canonical ensemble is used, which requires for exact conservation of quantum numbers (rather than global conservation of quantum numbers as in the grand canonical ensemble). The requirement for exact conservation of quantum numbers places a constraint on the thermal model, so that

a canonical ensemble. However it has been shown that results obtained using grand canonical and canonical approaches converge in the limit of high multiplicity [23].

Thermal models have been applied to a wide range of results from p + p and p + $\overline{\text{p}}$ collisions from $\sqrt{s}$ = 19.4 GeV to $\sqrt{s}$ = 900 GeV by Becattini and Heinz [61]. The multiplicities extracted from the thermal model agree well with the measured values, as shown in Figure 2.7. However it is worth pointing out that agreement could only be achieved by using a γ_s value of ~ 0.58 or less.

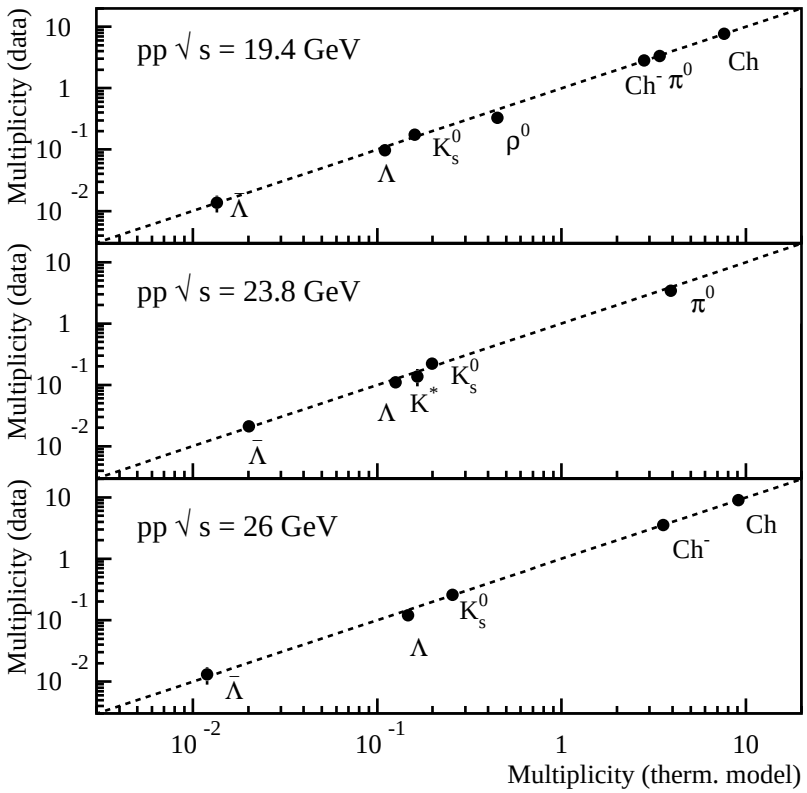

Figure 2.7: Measured yields from proton proton collisions (with $\sqrt{s}$ between 19.4 GeV and 26 GeV) agree with thermal model predictions (taken from [61]).

The analysis described herein is concerned with the measurement of K^0_S, Λ and $\overline{\Lambda}$ particles from p + p collisions at $\sqrt{s}$ = 200 GeV, for which there is a similar measurement made by UA5. A Becattini thermal model analysis has also been performed for the UA5 experimental results of p + $\overline{\text{p}}$ collisions at $\sqrt{s}$ = 200 GeV [62]. The results indicate good

in Table 2.1.

Particle	Measured Yield	Thermal Model Prediction
All Charged	$21.4 \pm 0.4 \pm 0.72$	21.27
K^0_S	$0.75 \pm 0.09 \pm 0.009$	0.783
Λ ($\overline{\Lambda}$)	$0.23 \pm 0.06 \pm 0.008$	0.194
Ξ^-	$0.015 \pm 0.015 \pm 0.0002$	0.0123

Table 2.1: Becattini's thermal model analysis agrees with the strange particle data taken by the UA5 data for $\mathrm{p} + \overline{\mathrm{p}}$ at $\sqrt{s} = 200$ GeV. The displayed yields are extrapolated over the full rapidity range (taken from [62]).

Thermal model analyses thus give very good agreement with experimental data, both for heavy ion data, where chemical and thermal equilibrium may be attained through re-scattering processes, and also in collisions of protons and anti-protons, where there is considered to be no re-scattering. Agreement with thermal models therefore cannot indicate that thermalisation has taken place. It has been argued that 'particles may be born thermal' and that the agreement of the data with thermal models is due to a statistical filling of the available phase space [23]. Indeed, the Hagedorn 'temperature' for proton+proton collisions has been shown to represent the Lund model's string tension [64].

Chapter 3

Experimental Setup

The Relativistic Heavy Ion Collider (RHIC) ia situated at Brookhaven National Laboratory, on Long Island in the USA. The collider comprises two super-conducting synchrotrons which accelerate heavy ions in opposite directions, with beam energies from 30 GeV/A up to 100 GeV/A [65]. Therefore, the maximum centre-of-mass heavy ion collision energy ($\sqrt{s}$) available at RHIC is between 60 GeV/A and 200 GeV/A. Experiments at RHIC are mainly devoted to the searches for the Quark-Gluon Plasma, but as well as colliding heavy ions, RHIC is able to collide lighter ions such as protons on protons, and deuterons on gold. The maximum proton beam energy is 250 GeV.

The RHIC began operating in 2000, and to date, there have been four main experimental runs, which are summarised in Table 3.1. The p + p run, which is the subject of this analysis, was undertaken between December 2001 and January 2002. Collisions were analysed using the Solenoidal Tracker at RHIC (STAR) detector which forms one of the 4 four main experiments placed at the beam intersection points around the ring.

Run	Year	CMS energy $\sqrt{s}$	Collision Species
1	2000	130 GeV	Au + Au
2	2001-2002	200 GeV	Au + Au
2	2001-2002	200 GeV	p + p
3	2003	200 GeV	d + Au
4	2004	200 GeV	Au + Au

Table 3.1: A summary of the major runs at RHIC.

The Relativistic Heavy Ion Collider Facility is depicted schematically in Figure 3.1. The Collider cannot accelerate ions from rest, so several pre-accelerators are used in order to provide ions for RHIC injection [65]. For protons the acceleration to RHIC injection energy is a three stage process. Protons from a source of hydrogen gas are accelerated to 200 MeV by a proton Linear Accelerator (LINAC). The 200 MeV protons are then injected into a booster synchrotron, which further accelerates the protons to 1.5 GeV. The booster infact incorporates two injection lines; one for protons and another for heavy ions. When used to accelerate heavy ions the booster's main purpose is to strip the remaining electrons off the ions.

The 1.5 GeV protons are transferred to the Alternating Gradient Synchrotron (AGS). The AGS has been operating since the 1960's, and was itself used for the first Relativistic Heavy Ion experiments, starting in 1986. The AGS gets its name from the fact that its bending magnets are arranged into sectors, with alternately increasing and decreasing radial gradients. These alternating gradients help to focus the beam. Protons in the AGS are accelerated from 1.5 GeV to the RHIC injection energy of 25 GeV.

As is common with synchrotrons, the ions are accelerated in bunches, with each bunch containing $\sim 10^{11}$ ions. Ions are transferred to the RHIC via the AtR (AGS to RHIC) transfer line, which can supply both rings separately with ion bunches, one bunch at a time.

3.2 The Relativistic Heavy Ion Collider

The Relativistic Heavy Ion Collider consists of two intersecting synchrotron rings, each 3.8 km in circumference. Bending and focusing of the beam is achieved by 1740 superconducting magnets, arranged in 6 segments around each ring. The magnets must be run at ~ 5 Kelvin, so they are cooled with liquid helium and nitrogen. The two rings are identified as yellow, where the ions travel anti-clockwise, and blue, where the ions travel clockwise.

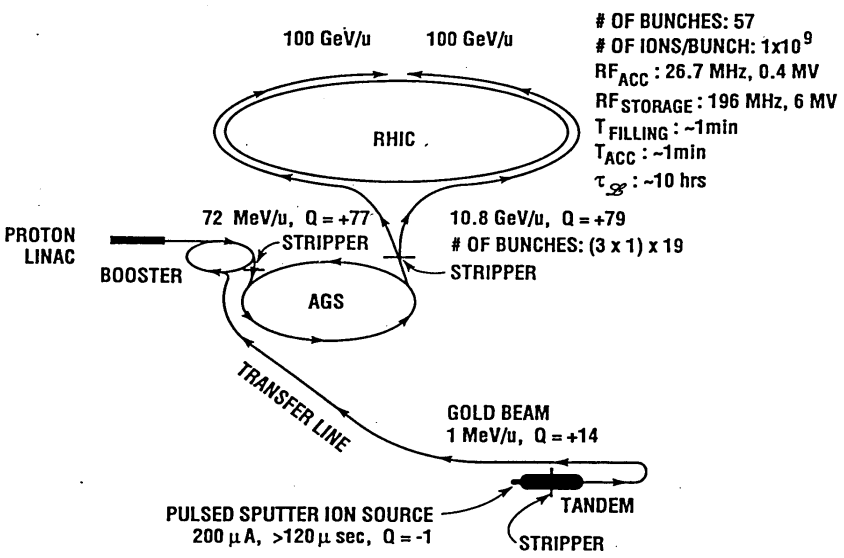

Figure 3.1: A schematic diagram showing the passage of particles as they pass from a source (the proton LINAC or the Tandem Van de Graaf generator) to the Alternating Gradient Synchrotron (AGS) and finally to the Relativistic Heavy Ion Collider (RHIC) [66].

Protons of energy 25 GeV are injected into the rings and need to be accelerated by RHIC up to 100 GeV. The energy of the particles is increased by using RF cavities which provide an accelerating alternating potential, operating at radio frequency (RF). During the acceleration stage it is advantageous to capture the injected ions from the AGS in bunches, as it is much easier to accelerate small ion bunches, compared to continuous beams. The bunch configuration for the year 2 p + p run is detailed in Table 3.2.

Collision Type	Number of Bunches	Mean Number of Ions per bunch	Minimum Time Between Bunch Crossings (ns)
p + p	60	100 x 10^9	213 ns

Table 3.2: Bunch configuration for year 2 p + p running.

Collisions are made by steering each of the counter rotating beams into a common beam pipe, by using a 'kicker' magnet. The beams are diverted back into their own respective rings by another kicker magnet, at the opposite end of the beam pipe.

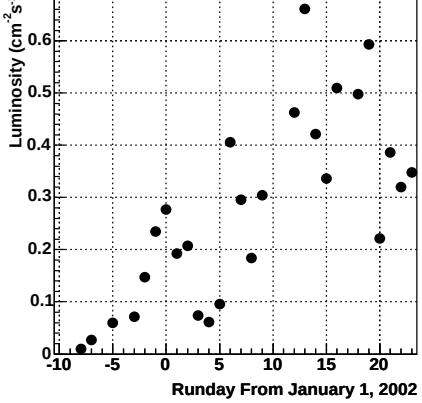

Figure 3.2: Average luminosity vs run day.

3.3 Maximising Beam Luminosity

Although the main advantage of colliders is the potential maximum use of *all* of the available beam energy, it comes at the expense of the experimental difficulty of achieving acceptable collision rates. This is because the density of ions available in a beam is less than for a fixed solid target.

Once the bunches have been accelerated to the required energy, RHIC operates in its storage ring mode. In this mode all of the ions in RHIC circulate with a frequency, f, of 78 kHz. The length of a typical store may be ten or so hours, so bunches of ions have many opportunities to interact over the time of a store.

The collision rate, R, obtainable at RHIC is determined by,

$$R = L\sigma \tag{3.1}$$

where σ is the nuclear interaction cross section and L is the beam luminosity, which is defined by,

$$L = \frac{f \times n_{bunch} \times N_{blue} \times N_{yellow}}{(4\pi\sigma_x\sigma_y)} \tag{3.2}$$

where N is the number of ions in either the blue or yellow ring ($\sim 10^{11}$), n_{bunch} is the number of filled bunches, and $4\pi\sigma_x\sigma_y$ is the beam cross sectional area. It is important to try and minimise the beam cross sectional area ($4\ \pi\sigma_x\sigma_y$) in order to maximise the

beam scattering due to Coulomb interactions between particles in the same bunch [67], introduces a defocusing effect, and this places a limit on the maximum luminosity which can be achieved.

The luminosity can also be increased by increasing the average number of ions in the blue and yellow rings, N_{blue} and N_{yellow}. This number varied throughout the length of the 30 day p + p running period, leading to luminosity variations as shown in Figure 3.2.

Over the time of a store, the luminosity becomes reduced as ions are removed from the beam, and it is necessary to dump the beam by magnetically steering it out of the rings. It is useful therefore for some (~ 4) of the buckets to be left empty as this gives a time gap of a few $/mus$ and allows for easier beam steering. As the beam luminosity was gradually reduced throughout each run, *average* luminosity values are used in Figure 3.2.

3.4 The STAR Detector

The Solenoidal Tracker at RHIC (STAR) detector is primarily a hadron spectrometer. It consists of many subsystems, used for event triggering, particle tracking and particle identification. STAR gets its name from the fact that its main tracking detector is a large cylindrical gas-filled Time Projection Chamber (TPC), which is inside a solenoid magnet, designed to produce a uniform magnetic field within the detector of up to 0.5 T. A schematic diagram of the STAR detector is presented in Figure 3.3. The sub-systems particular to the analysis of strange particles produced in p + p collisions are discussed in the next sections, and are described in greater detail elsewhere [68],[69].

3.4.1 Particle Tracking Using the TPC

The main detector is the Time Projection Chamber (TPC), and its job is to measure the trajectory of particles which are created in the p + p collisions. A schematic diagram of the Time Projection Chamber (TPC) [70] is shown in Figure 3.4. It is a large cylindrical detector with an outer radius 2 m and is 4.2 m long, with the beam line passing through the centre of it. The TPC can provide tracking for charged particles with pseudo-rapidity

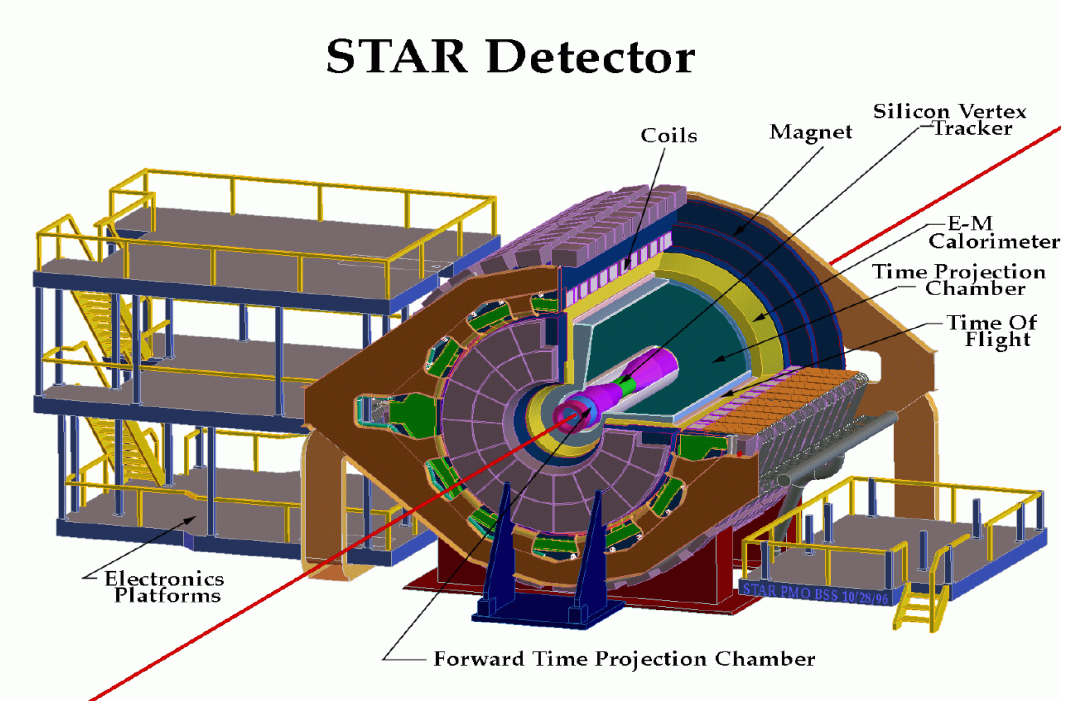

Figure 3.3: Schematic diagram of the STAR detector [66].

$|\eta|$ up to < 1.8 and has full azimuthal coverage and symmetry.

The inner part of the TPC through which the beam pipe runs has a radius of 50cm, meaning that the active regions of the TPC (radially) are from 50cm to 200cm. The active region is filled with P10 gas (10% methane and 90% argon). As charged particles produced in $\mathrm{p}+\mathrm{p}$ collisions traverse the active regions, they ionise the P10 gas with read-out from the TPC being based on detecting the ionisation electrons.

The electrons drift through the gas under the influence of an electric field. The field is produced by a central membrane cathode held at 28 kV, and the shield grids at the end caps which are held at ground. Thus the TPC may be envisaged as two independent detectors, joined at the centre, with electrons in each half drifting in opposite directions towards the outer read-out planes. As the electrons can drift by distances of up to 2m, the choice of gas is very important. As well as having small electron absorption, P10 gas has a low diffusion constant which limits charge spreading, which ultimately results in good two track resolution. The P10 gas is held at slightly above atmospheric pressure, in order to stop impurities from leaking into the detector.

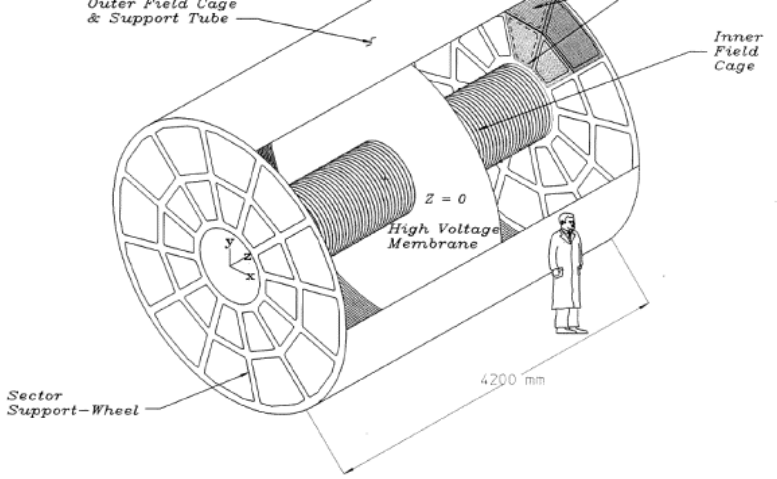

Figure 3.4: A diagram of the TPC. The east and west halves of the TPC are divided by a central high voltage membrane. Both ends of the TPC are split into 12 super-sectors which contain pad rows which are used to read out particle hits [66].

As the drifting electrons reach the read-out planes they approach a gating grid as shown in Figure 3.5. The gating grid is an electronic shutter composed of anode wires which controls whether the drifting electrons are allowed to be detected at the pad plane. When the grid is in the closed state the wires are alternately held at +75 V and - 75V, to collect both the drift electrons and any remaining positive ions. The grid is only opened (ie set to 0 V) when a valid trigger signal is received and when the data acquisition system is not already processing a previous event.

When the gated grid is open the electrons are detected by a Multi Wire Proportional Counter (MWPC). This is to say the electrons are accelerated by anode wires held at high potential ($\sim$ 1 kV) so as to produce an avalanche of electron+ion pairs. The avalanche charge is proportional to the initial amount of ionisation which is important for calculating the energy loss of the particle as a function of distance traveled, $\frac{dE}{dx}$. Charge is prevented from re-entering the TPC by the shield grid. The positive ions created by the avalanche move quickly away from the anodes, and their movement induces a read out signal on an array of cathode pads underneath the anode wires as shown in Figure 3.5.

The cathode pads are arranged into straight lines as shown in Figure 3.6 which are configured into 12 radial super-sectors, as shown in Figure 3.4. Each super sector is divided into an inner sector of 13 pad rows and an outer sector of 32 pad rows giving a

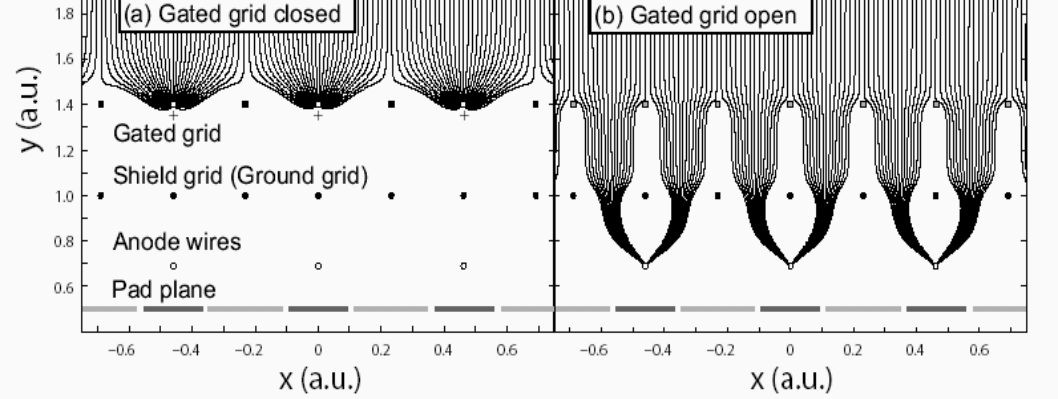

Figure 3.5: A diagram of the region between the gating grid and the read-out pads for part of a pad row. Diagram a) is for when the gating grid is closed, and b) is when the gating grid is open. The region between the shield grid and the anode wires operates like a proportional counter, as electrons are accelerated towards the high voltage anode wires. The movement of positive ions, created in the proportional region induces a voltage on the cathode pads. A constant electric field exists beyond the gating grid which extends to the central high voltage membrane shown in Figure 3.4 and defines the drift region (taken from [73]).

total of 45 pad rows which is the maximum number of space points which can be used to reconstruct a particle's trajectory.

The size and spacing of the pads is important as it determines the hit resolution. The pads in the inner sector, at small radial distance from the TPC centre are smaller (2.85mm x 11.5mm) than in the outer sector (6.2 x 20mm) in order to improve hit resolution where the track density is largest. The spacing between pad rows in the inner sector ($\sim$ 50mm) is however larger than in the outer sector ($\sim$ 20mm) because of the limited available space into which the read out electronics can be installed.

In order to achieve track reconstruction in 3 dimensions, a 3rd ordinate is needed, in addition to the 2 which can simply be found from the physical locations of the cathode pads. The third ordinate is found from the time it takes for electrons to drift to the cathode pads, using the trigger time as a reference point. The pad signal is sampled by an ADC every 100 ns, and the third ordinate is calculated by dividing the drift time by the average drift velocity of electrons within the TPC. Laser beams are used to make regular drift velocity calculations, which varies as a function of temperature and pressure but is typically 5 cm/μs; the maximum drift time is therefore 40 μs.

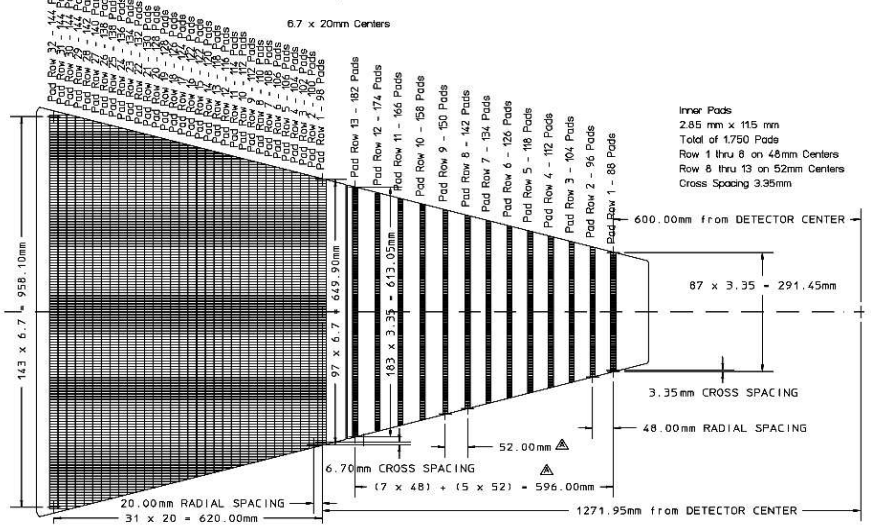

Figure 3.6: A diagram showing the 32 outer cathode pad rows and the 13 inner pad rows, which make up the 45 pad rows in each of the 24 super-sectors (taken from [68]).

The analogue signal from the pads is processed by Front-End Electronics (FEE) cards. Each FEE card contains an Analogue to Digital Converter chip which samples the cathode pad voltage every 100ns, converting it into a 12 bit digital number. The outputs from all of the FEE cards are gathered by readout boards, and are sent to the Data Acquisition system (DAQ). The DAQ system builds the event from the read out boards and writes it to disc, with the whole process taking about 1 second.

3.4.2 The Magnet

The TPC is situated inside a large solenoidal water cooled aluminium magnet, which has an outer diameter of 7.3m. When operating in full field mode it generates a magnetic field, B, of 0.5 T, parallel to the electric field. The magnetic field is very important as it enables the transverse momentum, p_T (in GeV/c), of the tracks to be calculated from their radius of curvature, R using,

$$p_T = 0.2998 \times qBR \tag{3.3}$$

where q is the charge of the particle. The magnet is able to operate in either Forward

calculate systematic errors.

3.4.3 Triggering using the Beam-Beam Counters (BBCs)

Even though there is only a small probability ($< 0.5\%$) of a p + p bunch crossing yielding an actual collision, the maximum frequency of bunch crossings is large (~ 4.7 million per second). The rate at which data can be recorded from STAR is limited to ~ 1 event per second. It is therefore important to determine when a collision event has taken place.

The STAR p + p trigger is a pair of Beam-Beam Counter (BBC) detectors, situated at $\pm$ 3.5m from the interaction region. Each BBC disc is composed of closely packed scintillating tiles which surround the beam pipe and are sensitive to charged particles. The scintillator tiles are arranged in a circle around the beam pipe, and cover a pseudo-rapidity range $3.3 < |\eta| < 5.0$. The scintillation light is converted into voltage by photo-multiplier tubes, and this voltage is sent to an ADC which sums the output of all of the tiles arranged around the beam pipe. If both of the BBCs register a signal within the coincidence window of 17 ns, then other detectors, such as the Time Projection Chamber are triggered.

Triggering for p + p collisions at $\sqrt{s} = 200$ GeV is thus reliant on the the break up of *both* incident protons. As illustrated in Figure 3.7 this can be caused by a non-diffractive p + p collision. When a nucleon suffers a diffractive scatter it may become only slightly excited, and lose a relatively small amount of its energy, producing only a small number of particles compared to a non-diffractive collision [71]. The trigger will be sensitive to doubly diffractive events, but not singly diffractive events. Thus the trigger is sensitive to the Non-Singly Diffractive (NSD) part of the total inelastic cross section, which has been measured to be 31.1 ± 3.7 mb [73].

The STAR detector can also be made to record events involving the collisions of empty buckets (used for beam steering). In this instance the RHIC clock is used to determine when crossings involving empty bunches may take place. Such events are known as 'abort gap' events.

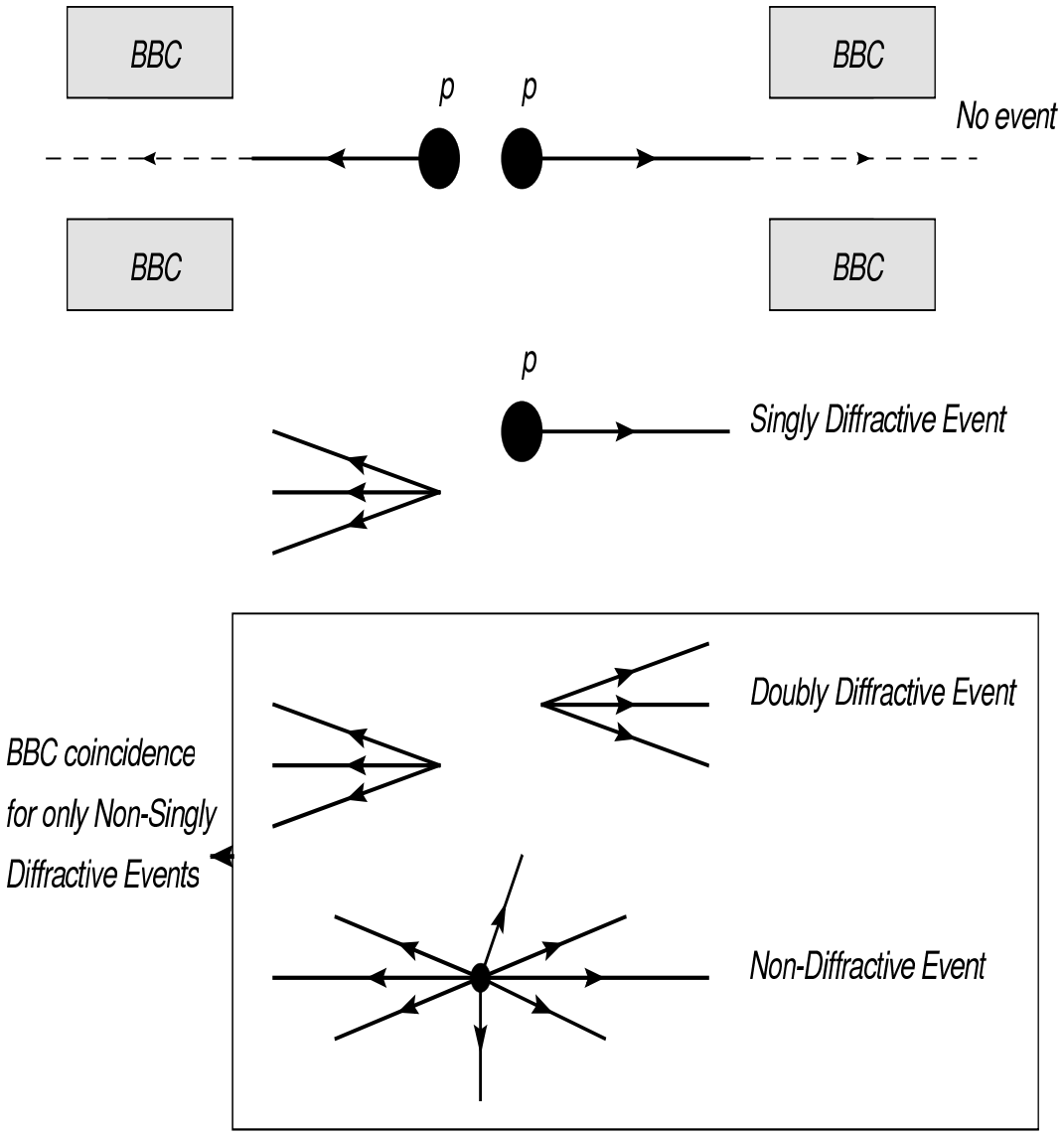

Figure 3.7: A Non-Singly diffractive event is characterised by the break up of both incomming protons, and is the part of the overall p + p cross section which the BBC is sensitive to [71].

The CTB consists of a Barrel shaped array of 240 scintillator slats, arranged around the outside of the TPC at a radius of 2.14m. Each 1m long slat covers 6 degrees in azimuth. The CTB has complete azimuthal coverage for charged particles, with $|\eta| < 1$. The scintillator slats are sensitive to charged particles, with the photo-multiplier tube and electronics being located on the slats themselves. The CTB has a fast (< 100ns) response time.

The maximum drift time for electrons in the TPC is 40 μs, but, if every bunch crossing were to yield an event, collisions may occur every 0.2 μs. Therefore there is some chance for electrons produced in events both before and after the triggered event to be mixed in with electrons produced by particles from the triggered event. A reconstructed event may be pictured as being composed of tracks from both the triggered event and a background of so called 'pile-up' tracks, from other collisions which may occur within the drift time of the TPC.

The fast response time of the CTB is particularly useful for the p + p analysis, as its response time is much less than the time between bunch crossings. If a track is matched back to a hit in an individual CTB panel, then there is a high probability that such a track came from the triggered event, and not a 'pile-up' event.

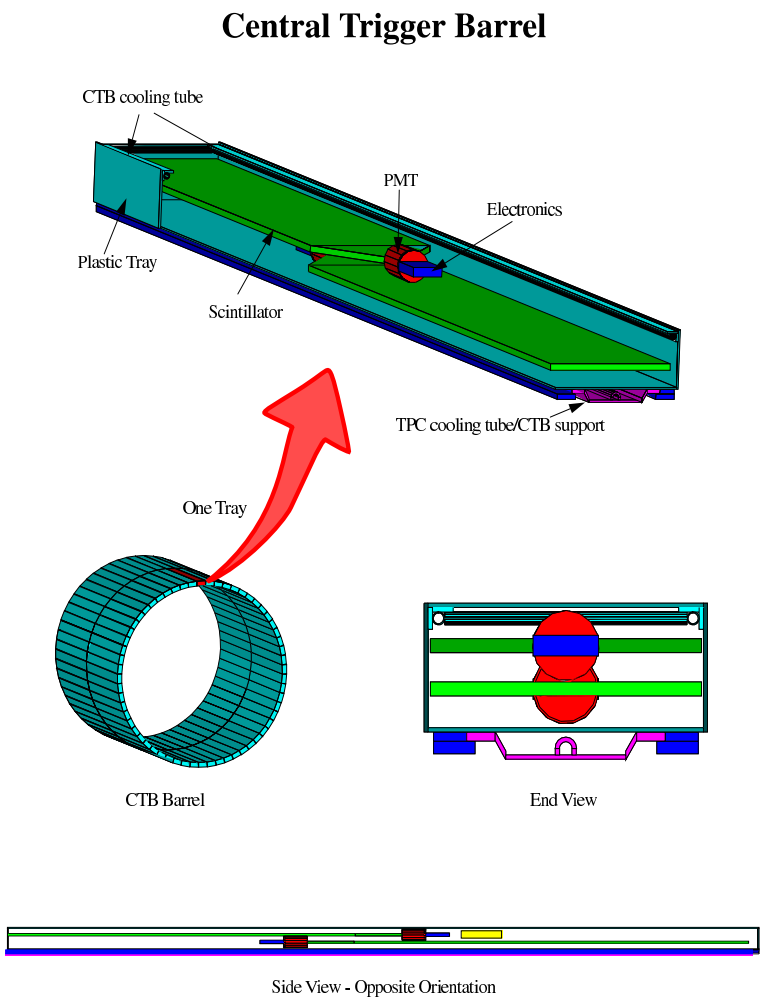

Figure 3.8: A diagram of the Central Trigger Barrel (CTB), and one its trays. Each of 120 plastic trays contain 240 scintillator slats, which are arranged in a barrel shape around the outside of the TPC.

Chapter 4

Event Reconstruction

In order to analyse the particles generated in a p + p collision event the digital output from the STAR detectors must be reconstructed into particle tracks. An example of a fully reconstructed p + p event is shown below in Figure 4.1.

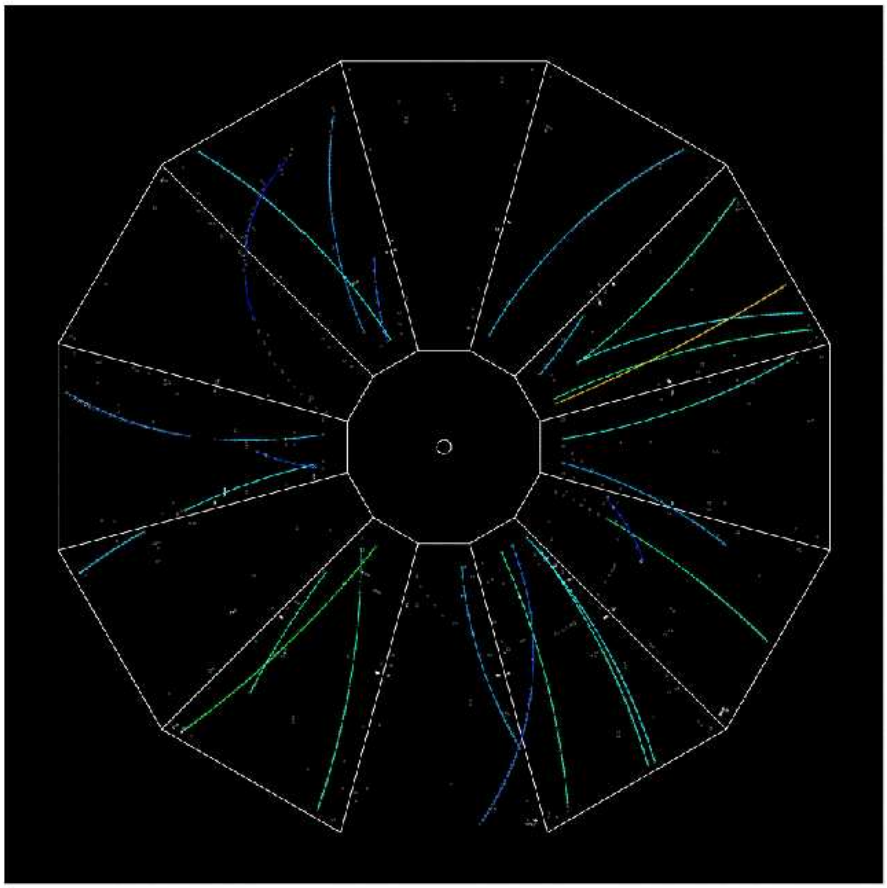

Figure 4.1: A reconstructed p + p collision at $\sqrt{s}$ =200 GeV within the STAR TPC.

Λ, $\overline{\Lambda}$ and K^0_S analysis presented in this thesis. Essentially, event reconstruction for p + p collisions consists of 4 steps:

1) Space point (or 'Hit') finding. The ADC values, which are the output of the read out pads at either end of the TPC are converted into 3 dimensional space points.

2) Track reconstruction. Hit points are joined together to make global tracks.

3) Primary vertex finding. The interaction point or primary vertex is found by determining the best common point of origin for all of the global tracks. Global tracks may be refit using the primary vertex as an extra hit point to form primary tracks.

4) V0 finding. Neutral strange particles are reconstructed from their charged decay products.

The following sections focus on each of the above procedures in more depth.

4.1 Space Point Determination

Tracks are reconstructed from space points which are clusters of charge induced on the cathode read out pads at either end of the TPC. Such clusters are formed from the raw ADC outputs from the cathode pads, located on the TPC end-caps. Therefore the physical location of the pad-rows determines the radius and azimuth of the original ionisation caused by the track.

Only those ADC values that are above a threshold 'pedestal' value are written out. For each new data acquisition period and before applying the high voltage to the STAR TPC, pedestal ADC values are measured.

The ADC readouts are arranged into time ordered sequences for each pad in a row. Clusters are sequences of ADC values from adjacent cathode pads both along the pad row (the y direction), and in adjacent time buckets (the z direction, parallel to the beam line). An example of how a cluster may look in terms of ADC values is shown in Figure 4.2. The centroid of the cluster is defined as a hit point, and is found from fitting a 2 dimensional Gaussian function in order to derive the y and z ordinates of the cluster.

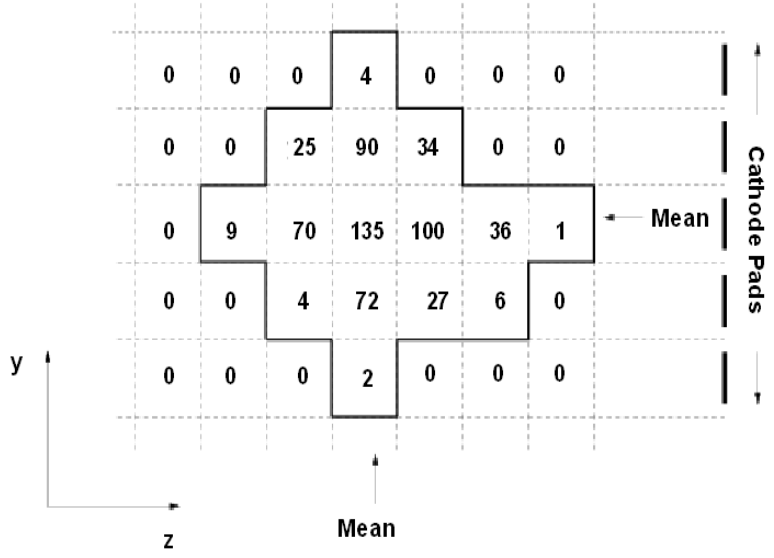

Figure 4.2: Schematic depiction of how ADC readout values make a cluster, the centroid of which makes a hit point, from which tracks can be reconstructed.

The third ordinate (x) runs radially out from the centre of the TPC and is defined as the centre of the pad row in which the cluster was found.

4.2 Track Finding

Track finding in the TPC is performed by the TPC tracking package (TPT) [72]. TPT is the same tracking package used for the Au + Au analyses and, therefore, it is very robust as it must be capable of reconstructing thousands of tracks from a single event.

Track finding is accomplished by first considering those hits in the outermost pad rows, where the hit density is lowest. Every hit on the outermost pad row is considered as a potential starting point for a track and are therefore called "roots". Using an assumed position for the interaction point (or primary vertex) as a guide, 3 point links are made between one root and the adjacent space points by assuming a simple linear fit. Such links are made into longer segments by extrapolating radially inwards, using the local slope of the segment as a guide. The longest segment for this root is stored, and its hit points removed from the hit pool. Once all roots on the outermost pad row have been extended

have been exhausted.

For charged particles a helical trajectory is expected due to the magnetic field. Therefore, once a segment has been assigned to each root, a helix fit is applied to the segments with space points being removed or added to the track according to the fit.

Low momentum tracks will spiral several times and, therefore, have large path lengths. A track merging algorithm compares helix parameters from different tracks and, if they agree, performs track merging. The minimum number of hits required to make a track is 5. However, sometimes, particularly when there may be missing hits on a track trajectory, a single track may be reconstructed as two split tracks; this is known as track splitting. Generally a larger number of hits (15 for this analysis) is used for the final analysis, as this helps to minimise the chance of track splitting. The position resolution in the pad-row and drift directions is between 0.5 and 3 mm.

The number of reconstructed tracks for each event may be counted to give the global track distribution, as shown in Figure 4.3 ($|\eta|$ <1). The global track distributions are different for the two luminosity runs due to the additional contributions of tracks from 'pile-up' events, which is discussed next.

4.3 Pile-up Within the TPC

Perhaps the most challenging aspect of the p + p analysis is how to deal with multiple events, or 'pile-up' occurring within the relatively slow TPC drift time. The TPC read out is integrated over a 40 μs time period, but the proton beams can cross every 213ns. Therefore nearly 200 p + p events can occur during the drift time of the TPC, and there can also be 200 p + p events depositing charge in the TPC at the instant before the BBC trigger occurs.

However, the probability for a single bunch crossing producing an NSD p + p event is very low, being dependent on the luminosity, L, and the cross section, σ_{NSD}. The number of minimum bias events occurring per second, R, is given by,

$$R = L\sigma_{NSD} \tag{4.1}$$

where σ_{NSD} has been measured to be 31.1 ± 3.7 mb [73]. Thus the number of collisions per second varies between $\sim$ 2500 s^{-1} and $\sim$ 20,000 s^{-1}. The number of pile-up events which can exist within the TPC is thus roughly between 0.2 and 1.6. These numbers approximately correspond to the variation in the observed mean number of global tracks shown in Figure 4.4, and so is a very strong indication of pile-up effects within the TPC. The effect of pile-up must be removed if a stable measure of multiplicity is to be achieved.

4.4 V0 Finding

Neutral strange particles such as Λ, $\overline{\Lambda}$ and K^0_S do not produce ionisation and are therefore not possible to detect directly using the TPC. Fortunately Λ, $\overline{\Lambda}$ and K^0_S particles can undergo a weak decay into two oppositely charged particles, as shown in Table 4.1.

As was found in the early cloud chamber experiments (see Figure 1.1), the oppositely charged daughter tracks of neutral strange particles make a characteristic 'v' shape, and pairs of such daughters may be combined to make a 'v0 candidate', with the '0' indicating that the candidate is electrically neutral. The STAR reconstruction code uses a v0 finder that searches for pairs of oppositely charged global tracks, compatible with having originated from a secondary decay vertex. In this initial v0 finding stage all global track pairs with a distance of closest approach of < 1.2cm are saved for later analysis. Although the majority of v0 decays occur before the active volume of the TPC (at a radius of 50cm), v0 candidates may be formed in this region as tracks are extrapolated back according to a helix fit.

Particle	Reconstructed Decay Mode [branching fraction]	quark content	Mass (GeV)
Λ	$\Lambda \rightarrow \pi^- + p$ [63.9 ± 0.5%]	uds	1.1156
$\overline{\Lambda}$	$\overline{\Lambda} \rightarrow \pi^+ + \overline{p}$ [63.9 ± 0.5%]	$\overline{uds}$	1.1156
K^0_S	$K^0_S \rightarrow \pi^+ + \pi^-$ [68.95 ± 0.14%]	$\frac{1}{\sqrt{2}}\lvert d\overline{s} + \overline{d}s\rvert$	0.498

Table 4.1: A summary Λ, $\overline{\Lambda}$ and K^0_S characteristics. Only the most predominant decay mode was used to identify Λ and $\overline{\Lambda}$s [7].

a definite Λ, $\overline{\Lambda}$ or K^0_S, or more likely just a combination formed from random crossing of charged background. In order to help determine the identity of a v0 candidate its invariant mass M_{V0} can be calculated from the measured properties of the two daughter particles with mass m_1 and m_2, and momentum $\vec{p_1}$ and $\vec{p_2}$,

$$M^2_{V0} = m^2_1 + m^2_2 - 2(E_1E_2 - \vec{p_1}.\vec{p_2}) \tag{4.2}$$

where the momentum of the daughters is found from their curvature in the magnetic field. The mass of the daughters must be hypothesised if the invariant mass of the parent is to be calculated. The invariant mass of the Λ, the $\overline{\Lambda}$ and the K^0_S at the v0 finding stage is shown in Figure 4.5. Peaks corresponding to the published [7] Λ, $\overline{\Lambda}$ and the K^0_S mass values (see table 4.1) are visible, and have been highlighted in blue. The peaks lie on top of a large background, produced from the large number of pairs which are formed from the 'combinatorial' background formed by random track crossings. A significant part of the analysis is the minimisation of the background regions (shaded red in Figure 4.5), and the maximisation of the blue signal region, which ultimately helps to reduce the uncertainty on the yield. Pile-up also has the effect of increasing the number of v0 candidates with luminosity, as shown in Figures 4.6 and 4.7

4.5 Vertex Finding

It is important to achieve an accurate determination of the interaction position (primary vertex) for each individual p + p collision. The primary vertex enables us to distinguish between primary tracks, which originate directly from the collision, and secondary tracks, which originate from, for example, weak decays of neutral strange particles. Moreover, suitable tracks can be refit using the primary vertex position as an extra hit point, allowing better momentum characterisation of the track. In particular for the p + p analysis matching tracks back to the primary vertex may be used to eliminate the effects of pile-up.

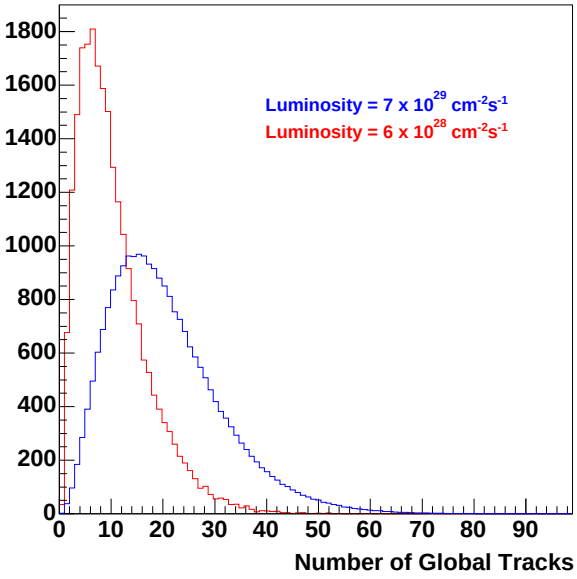

Figure 4.3: Global track distributions for two different luminosity runs ($|\eta| < 1$).

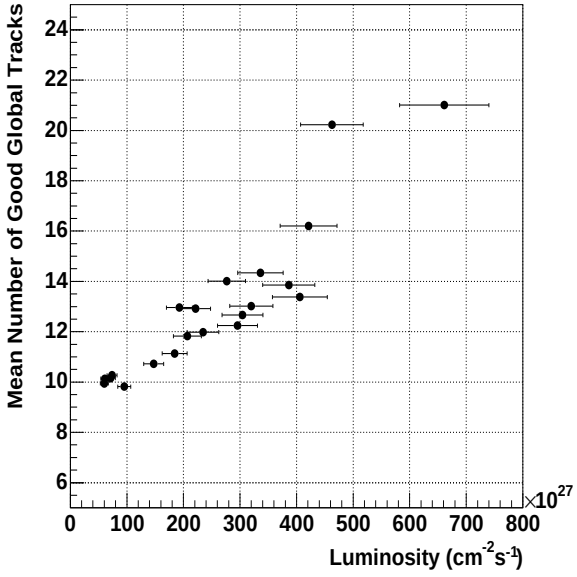

Figure 4.4: Mean global tracks versus average luminosity ($|\eta| < 1$).

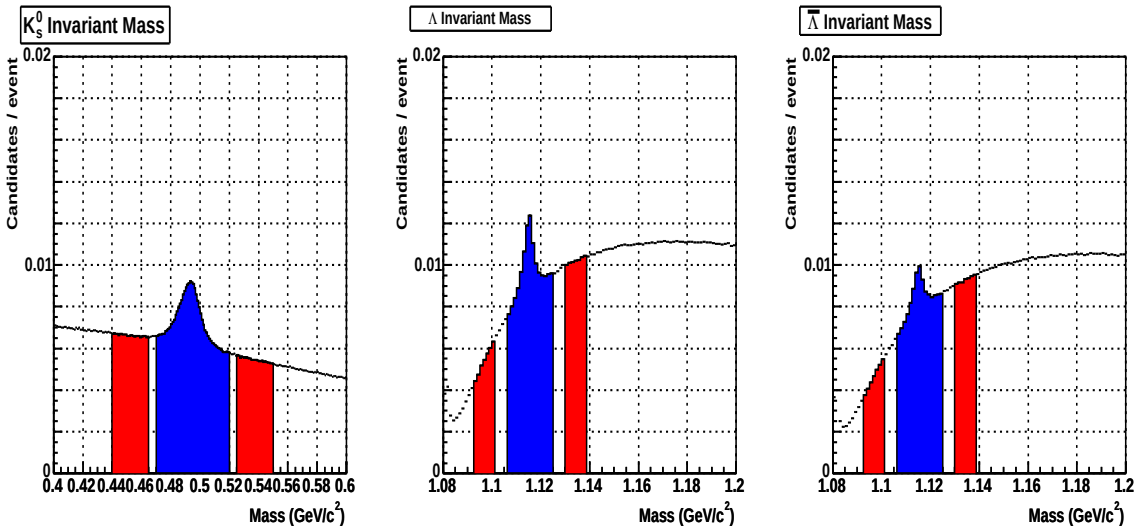

Figure 4.5: The invariant mass distributions for K^0_S, Λ and $\overline{\Lambda}$ (running from left to right), as reconstructed from the properties of the daughter particles, according to equation 4.2.

that the primary vertex reconstruction efficiency dropped appreciably when the number of global tracks within the TPC dropped below 50 [74]. This fact is particularly true in p + p collisions, which have mean global track multiplicities of between 10 and 20. The efficiency for primary vertex finding drops simply because of the small number of tracks available within the TPC for primary vertex reconstruction. A special piece of software, the proton-proton low multiplicity vertex finder, PPLMV, was designed to find the primary vertex in low multiplicity environments [75].

PPLMV constrains the vertex to lie somewhere along the beam axis and, in effect, only one ordinate, z (the position along the beam line) is therefore determined. The primary vertex finding code functions by only considering those tracks which match to specific Central Trigger Barrel detector (CTB) slats. This is crucial, as the response of the CTB is sufficiently fast so as to only be sensitive to those tracks which originate from the primary vertex.

All the CTB matched tracks are used to calculate the z ordinate of the primary vertex. The z ordinate is determined as being that value for which the χ^2, calculated using the distance of closest approach of the tracks to the reconstructed primary vertex, is minimised.

Higher momentum tracks are given greater weight than the lower momentum tracks, which have a larger chance of scattering off detector materials. Individual outlier tracks are iteratively rejected, and the vertex recalculated until there are no outlier tracks left.

All Global tracks found within the TPC can be re-fit, using the primary vertex as an extra, heavily weighted fit point, if the global track passes within 3cm of the reconstructed primary vertex. Tracks which undergo the re-fit are designated primary tracks, and the number of reconstructed primary tracks will always be less than the number of reconstructed global tracks, as not all global tracks pass through the interaction point. A primary track does not have to have a CTB match, because low momentum tracks may never hit the CTB, and because the CTB matching efficiency is finite, and drops for low p_T particles [73].

There are a maximum of two copies of each track per event, the 'global track', and

increase with luminosity (Figure 4.4), the primary track multiplicity remains stable with increasing luminosity as shown in Figure 4.9. Thus matching back to the primary vertex was deemed to be a good method of eliminating pile-up, as the multiplicity for those runs which are hardly effected by pile-up (those which on average have 0.2 pile-up events), is the same as for those runs which are strongly effected by pile-up (having on average 1.6 pile-up events).

4.6 Data Storage

As each event is processed, it is stored as part of a common Data Storage Tape (DST). A few hundred events are stored in detail individually on the DST in the form of a set of C++ classes. There are many thousands of DST files, as the total amount of p + p data available for analysis is 14 million events. The DST information is used by the whole of the STAR collaboration for many different analyses, and for an analysis involving just the v0 and track information it would be impracticable to run over the all of the DSTs.

The p + p analysis relies on the strangeness classes, which store the number of v0 candidates found for each event, as well as other information such as functions pertaining to the decay topology of the v0 daughter tracks. Thus the DSTs are condensed into a set of common Micro-DSTs, each $\sim$ 15 MBytes in size, which contain the event and v0 information relevant to this analysis. The analysis presented herein was performed using the common Micro-DSTs.

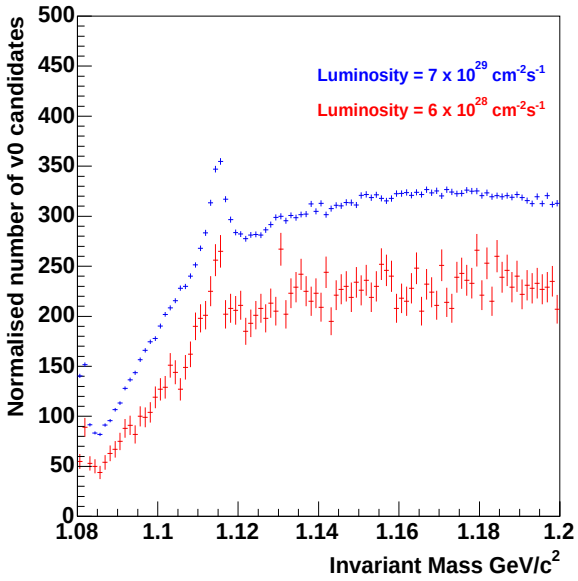

Figure 4.6: Normalised Λ invariant mass distributions for two different luminosity runs.

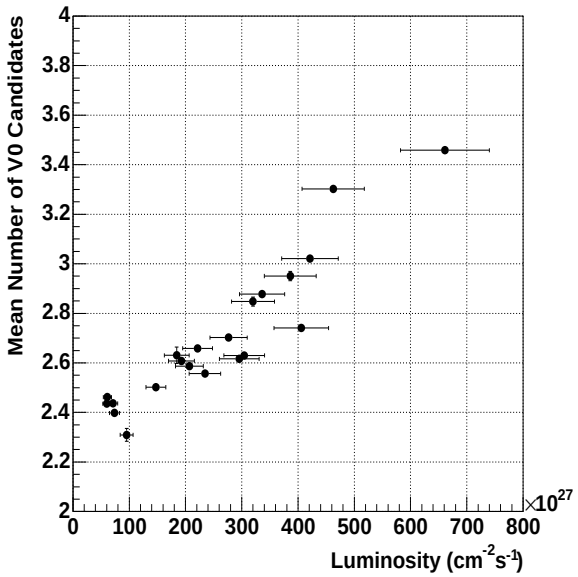

Figure 4.7: Mean number of v0 (Λ) candidates versus average luminosity.

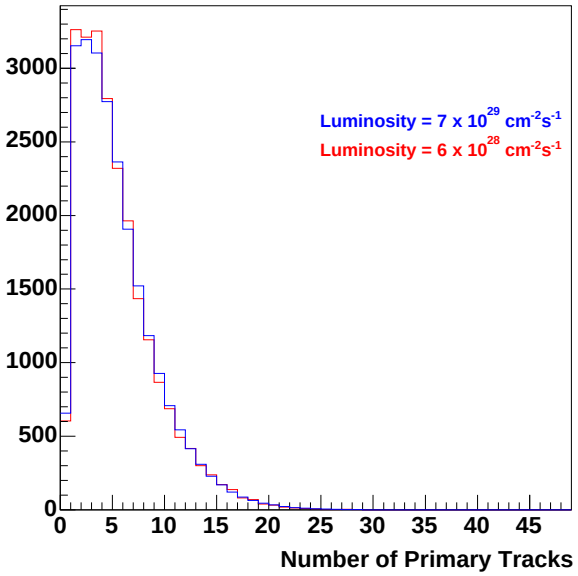

Figure 4.8: Primary track distributions for two different luminosity runs ($|\eta| < 1$).

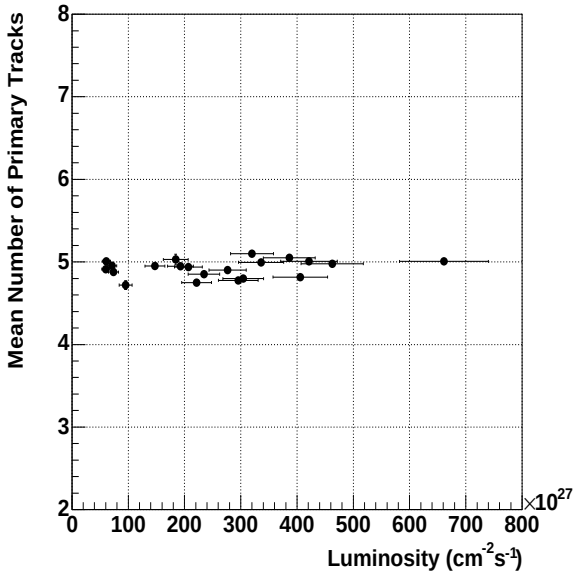

Figure 4.9: Mean primary tracks versus average luminosity ($|\eta| < 1$).

Chapter 5

Analysis

The end product of the analysis must be p_T spectra for Λ, $\overline{\Lambda}$ and K^0_S, from which mid-unit rapidity yields (dN/dy, with $|y| < 0.5$) can be extracted. The first stage of the analysis is the determination of the raw Λ, $\overline{\Lambda}$ and K^0_S yields directly from the Micro-DSTs. As was shown in Figure 4.5, the invariant mass spectra are dominated by background from random combinatorial crossings of tracks. The method of reducing this background is discussed in section 1.

Although it was shown in Figure 4.7 that the mean number of v0 candidates increases with beam luminosity due to pile up, it was shown in Figure 4.9 that the mean number of primary tracks (those tracks which can be matched back to the primary vertex) is stable with beam luminosity. Therefore matching v0s back to their primary vertex should provide a good method of discriminating against any pile up v0s. Unfortunately the efficiency of the vertex finder is reduced for low multiplicity events. The performance of the vertex finder, and the method used to correct for v0s which may erroneously fail the v0 to primary vertex matching method are discussed in section 2.

The third section describes how Λ, $\overline{\Lambda}$ and K^0_S spectra are binned as a function of transverse momentum, p_T. Finally the fourth section discusses the total efficiency correction, which corrects for losses due to v0 finding efficiency and TPC acceptance.

In Figure 4.5 it was shown that the Λ, $\overline{\Lambda}$ and K^0_S invariant mass spectra are dominated by a large background, produced from random pairs of positive and negative tracks. There were two techniques used to enhance the signal region with respect to the background. The rate of energy loss with respect to distance travelled ($\frac{dE}{dx}$) was used to provide Particle IDentification (PID) whereby the identity of the v0 daughter tracks (see Table 4.1) could be more easily determined. In addition, a number of geometrical cuts were applied to the v0s and daughter tracks found by the v0 finder. One of these cuts, the Distance of Closest Approach (DCA) of a v0 to the primary vertex is particularly important, as it provides a means of eliminating the effects of pile-up. Both of these techniques are described in the following subsections.

5.1.1 Particle Identification by Rate of Energy Loss with Respect to Distance Travelled ($\frac{dE}{dx}$)

As a charged particle traverses through the TPC it causes ionisation of the gas, losing energy in the process. The rate of energy loss with respect to distance travelled, $\frac{dE}{dx}$ can be used to identify particles as the shape of the $\frac{dE}{dx}$ curve as a function of the tracks momentum is characteristic for particles of a given mass. Figures 5.1 and 5.2 show $\frac{dE}{dx}$ vs momentum, p, for all positive and negative particles respectively detected in the TPC. In these figures $\frac{dE}{dx}$ bands characteristic of charged Kaons ($K^{\pm}$), charged pions ($\pi^{\pm}$), protons and anti-protons, (p,$\overline{p}$) and deuterons (d) can be observed.

The $\frac{dE}{dx}$ for a particular track can be determined from the Bethe-Bloch equation [76] which takes the form,

$$-\frac{dE}{dx} = \frac{e^2\,(Ze)^2\,n_e}{4\pi\epsilon_0^2\;m_e c^2\beta^2}\left[ln\left(\frac{2m_e c^2\beta^2\gamma^2}{I}\right) - ln(1-\beta^2) - \beta^2\right] \tag{5.1}$$

where e is the charge on an electron, and m_e is its mass, β and γ have their usual relativistic meanings, Z is the hadron charge, n_e is the electron number density, and I is the mean ionisation energy of the P10 gas. Equation 5.1 can be used to describe the

for a particular type of charged particle. The $\frac{dE}{dx}$ calculated from equation 5.1, and the measured $\frac{dE}{dx}$ for a particular track were compared and if they agree within $N(\sigma)$ that track is said to pass the $\frac{dE}{dx}$ cut. Here $N(\sigma)$ may be defined as,

$$N(\sigma) = \frac{\frac{dE}{dx}_{measured} - \frac{dE}{dx}_{Bethe-Bloch}}{(R/\sqrt{N_{hits}})\frac{dE}{dx}_{measured}} \tag{5.2}$$

where R is a resolution factor determined by calibration, and N_{hits} is the number of hit or space points on the track. Identification of charged hadrons is only possible for tracks with momentum below ~ 1 GeV, because the $\frac{dE}{dx}$ bands tend to merge at high p_T. It is important to mention that there is no correction for tracks which may be erroneously lost due to failing the $\frac{dE}{dx}$ cut. Therefore, as the measured $\frac{dE}{dx}$ values depend on a calibration, a $N(\sigma) = 5$ cut was used to identify the v0 charged daughter tracks. The $\frac{dE}{dx}$ bands after the $N(\sigma) = 5$ cuts for the positive and negative Λ daughters are shown in Figures 5.3 and 5.4 respectively.

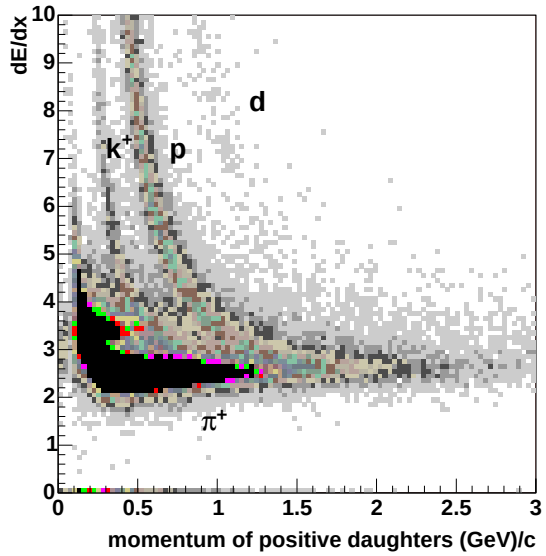

Figure 5.1: $\frac{dE}{dx}$ as a function of momentum for all positive tracks within the TPC.

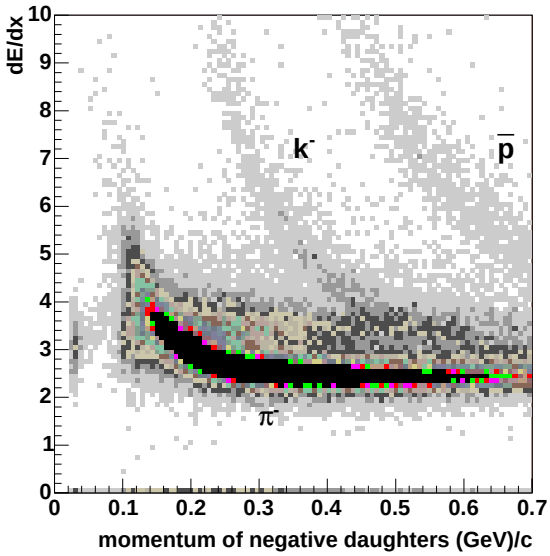

Figure 5.2: $\frac{dE}{dx}$ as a function of momentum for all negative tracks within the TPC.

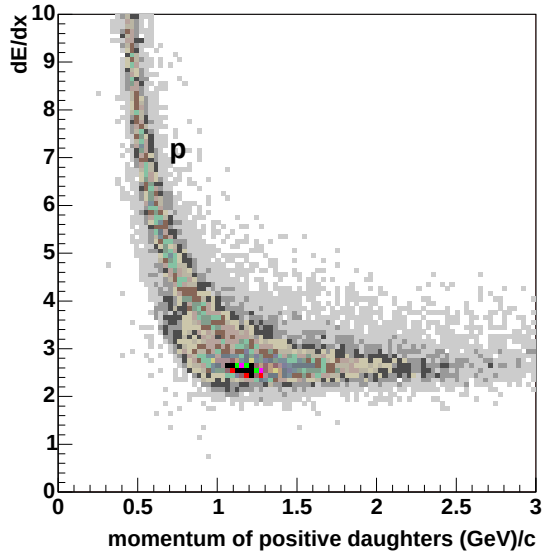

Figure 5.3: $\frac{dE}{dx}$ as a function of momentum for positive tracks within the TPC after the N(σ)=5 cut. The proton band has been isolated by the $\frac{dE}{dx}$ cut.

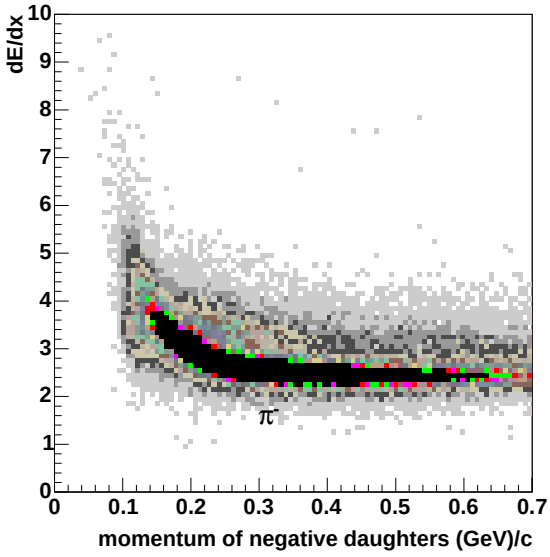

Figure 5.4: $\frac{dE}{dx}$ as a function of momentum for negative tracks within the TPC after the N(σ)=5 cut. The π^- band has been isolated by the $\frac{dE}{dx}$ cut.

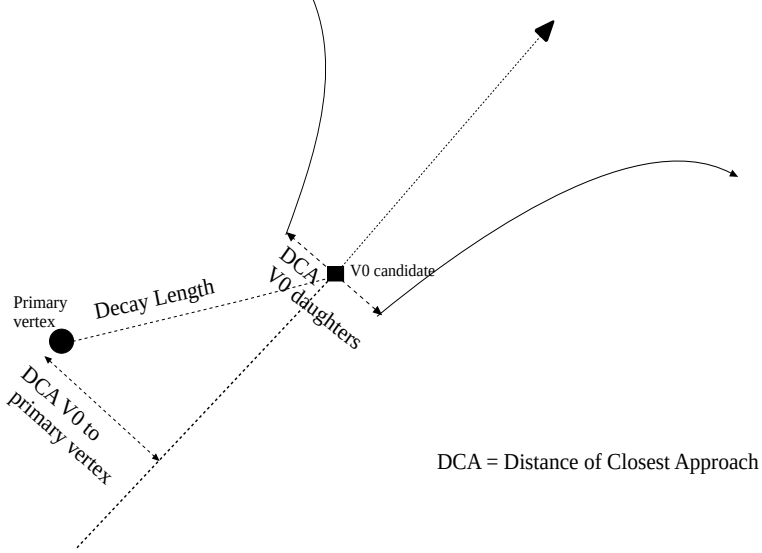

Figure 5.5: Topological cuts used for v0 (π^+ and π^- from a K^0_S decay in the diagram) identification.

5.1.2 Geometrical Cuts

Geometrical cuts are an effective way of reducing background, as v0 candidates formed from the random combinatorial crossing of tracks have different properties to true v0s. The cuts which were applied are shown defined diagrammatically in Figure 5.5. Each cut is described below:

- **Distance of Closest Approach (DCA) of the v0 daughters**

  This is the only cut which is applied at the initial v0 finding stage, and is initially set to 1.2 cm. The two hit resolution in the TPC is of the order of $\sim$ 1cm and the reconstructed daughter tracks may therefore be separated by some finite distance at the v0 decay vertex [70]. The amount of combinatorial background increases with the size of this cut.

- **Cylindrical Decay Length**

  The track density reduces with distance from the primary vertex. Near the primary vertex the number of randomly occuring track crossings will be large simply due to the increased track density. The decay length is the distance between the primary vertex and the decay vertex (see Figure 5.5), and the decay length cut requires for

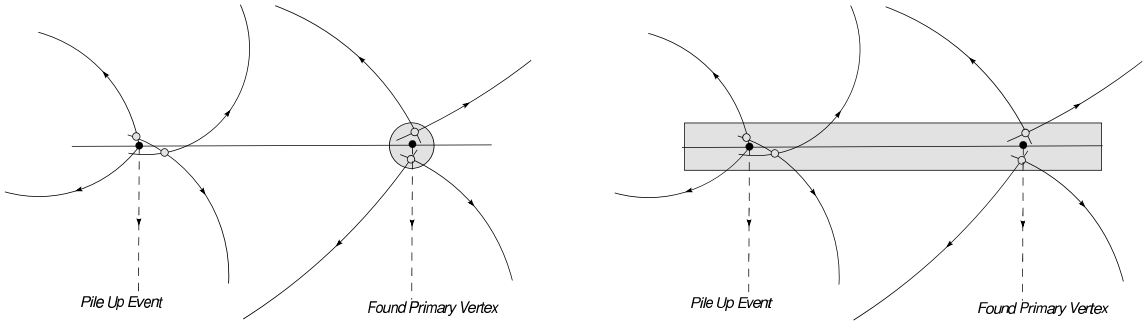

Figure 5.6: (left) A conventional 3 dimensional decay length cut will exclude combinatorial pairs from the triggered event, but not from any pile-up events within the TPC. Applying a radial decay length cut (right) excludes combinatorial background from both the triggered event and any pile-up events within the TPC.

the measured decay length to be greater than this cut. The amount of combinatorial background decreases with the size of the decay length cut. The decay length cut inevitably excludes some signal v0s (Λ,$\overline{\Lambda}$,K^0_S) as well as background v0s. However, the reduction in noise is significantly more beneficial than the decrease in signal.

Particular to this p + p analysis was the fact that a cylindrical (or 2d) decay length cut was applied, rather than the 3d decay cut (Figure 5.6). The cylindrical decay length cut is also described in Figure 5.6, and excludes a tubular region of v0 crossings along the beam line. The cylindrical decay length cut was shown to be more effective than the 3 dimensional version, as it also helps eliminate background from pile-up events, which can be envisaged as another event also occurring along the beam line. A 3 dimensional decay length cut would exclude all combinatorial background from the triggered event, but include combinatorial pairs from pile-up events.

- **Distance of Closest Approach (DCA) of the v0 to the primary vertex**

  The momentum vector of the v0 can be reconstructed from its daughter tracks. The vector can be extrapolated back to find its Distance of Closest Approach to the primary vertex (see Figure 5.5). All genuine primary v0 candidates should point back towards the primary vertex, and therefore have a small DCA. The application of this cut is expected to stabilise the v0 yield with respect to luminosity, as was

There is no reason for all of the combinatorial v0s to point back to the primary vertex, therefore the number of background tracks increases with this Distance of Closest Approach cut.

Due to reconstruction effects, neither the position of the primary vertex, nor the v0 momentum are known precisely. Indeed occasionally the vertex is not found at all, or found in the wrong place, in which case no genuine v0s will be found. Corrections for these losses, as well as primary vertex resolutions, are discussed in section 5.2.

- **Minimum number of track hits used to reconstruct a track**

  Tracks may be mis-reconstructed and split into smaller segments, such that they are not a proper representation of the full track. This cut is essentially meant to ensure track quality by excluding the split track segments which have low numbers of hits.

In order to apply the $\frac{dE}{dx}$ cut, the identity of the v0 must be hypothesised. Thus the initial stage of cut optimisation involved plotting individually for Λ, $\overline{\Lambda}$ and K^0_S, two dimensional histograms of cut parameter versus invariant mass, as shown for Λ in Figure 5.7 and for K^0_S in Figure 5.8. Using plots such as these initial cut values could be approximated by eye.

In order to further optimise the cuts a simple bin counting technique was employed to determine the amount of *Signal* relative to the amount of *Background*, where *Signal* is defined simply as,

$$Signal = Total - Background \tag{5.3}$$

where the *Total* and *Background* regions are defined in Table 5.1, and relate to the blue (*Total*) and red (*Background*) regions in Figures 4.5 and 5.9.

Implicit to the bin counting technique is that the background under the mass peak can be described by a linear function, thus one of the criteria for optimising the cuts was to obtain a linear background. It is evident from Figures 5.7 and 5.8 that very tight cuts

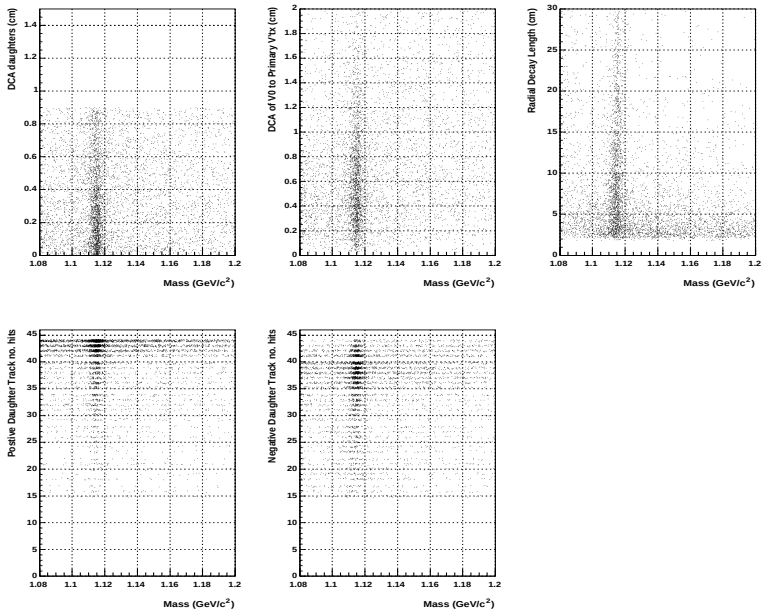

Figure 5.7: The initial stage of cut optimisation involved plotting the cut parameters vs Λ invariant mass. The signal region is centred on the Λ mass (1.116 GeV/c^2).

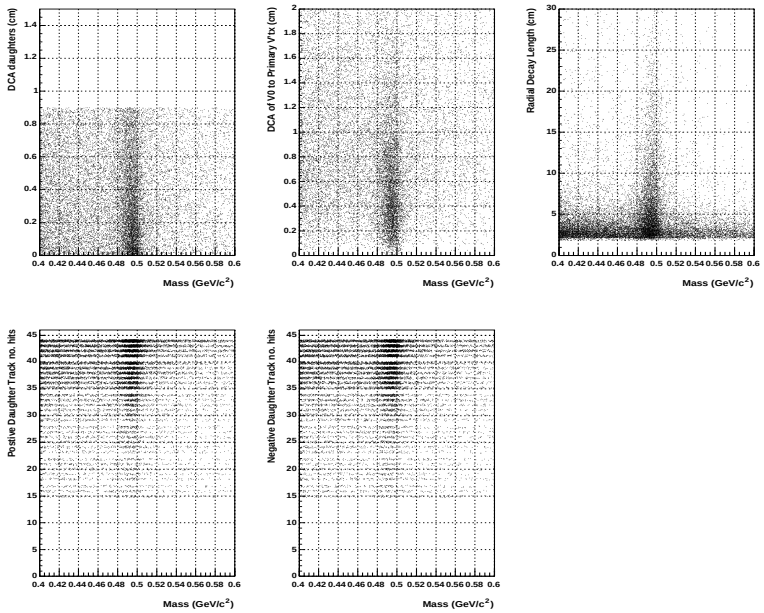

Figure 5.8: The initial stage of cut optimisation involved plotting the cut parameters vs K^0_S invariant mass. The signal region is centred on the K^0_S mass (0.498 GeV/c^2).

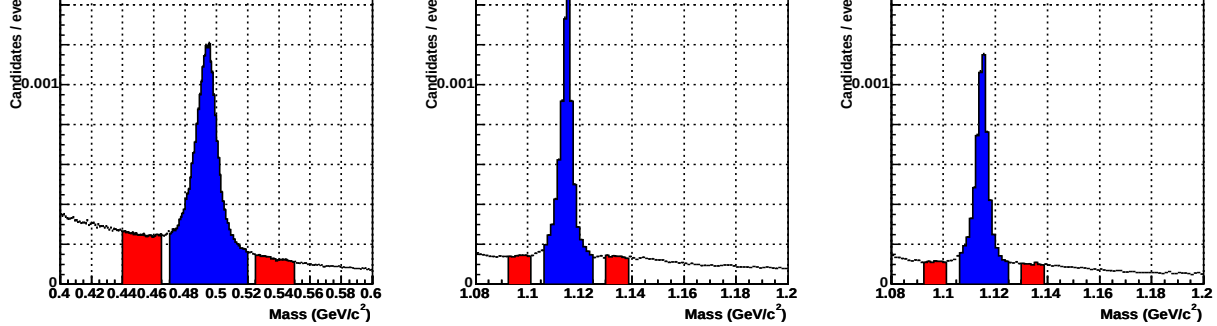

Figure 5.9: V0 masses after cuts. The blue shaded area indicates the signal region, and the red shaded area indicates the background regions, used for bin counting.

would eliminate almost all of the background; however, the consequence of this would be to reduce the signal region to a level where the statistical error is unsatisfactorily large. Thus optimisation involved changing cuts (the DCA of the daughters and the cylindrical decay length) so as to maximise both the extracted signal and the signal to background ratio. The final cut values are summarised in Table 5.2. The errors on *Total* and *Background* are assumed to be independent and Poissonian, thus allowing a statistical error to be calculated for *Signal*.

Particle	Lower background region	$Total(Signal+Background)$ region	Upper background region
Λ	$1.092 \rightarrow 1.102$ GeV/c^2	$1.106 \rightarrow 1.126$ GeV/c^2	$1.130 \rightarrow 1.140$ GeV/c^2
$\overline{\Lambda}$	$1.092 \rightarrow 1.102$ GeV/c^2	$1.106 \rightarrow 1.126$ GeV/c^2	$1.130 \rightarrow 1.140$ GeV/c^2
K^0_S	$0.440 \rightarrow 0.465$ GeV/c^2	$0.47 \rightarrow 0.52$ GeV/c^2	$0.525 \rightarrow 0.550$ GeV/c^2

Table 5.1: The regions of background and signal used to extract raw yields from the invariant mass histograms. *Background* is the sum of counts in the upper and lower regions.

Cut Type	Initial Value	Final value (Λ,$\overline{\Lambda}$ and K^0_S)
Number of Track hits	>10	> 15
DCA between v0 and Pr'y Vertex	none	< 2cm
DCA between daughters	< 1.2cm	<0.9cm
Cylindrical Decay Length	none	>2cm
Daughter $\frac{dE}{dx}$ identification	none	< 5 σ

Table 5.2: Optimised Cut parameters for Λ, $\overline{\Lambda}$ and K^0_S.

have improved the signal to noise ratio while maintaining reasonable populations of Λ, $\overline{\Lambda}$ and K^0_S. However, Table 5.3 also shows that a significant fraction of the total signal is excluded by the cuts. These 'lost' Λ, $\overline{\Lambda}$ and K^0_S are corrected for by using embedding techniques which are described in section 5.4.

Particle	$\frac{Signal}{Background}$ before cuts	$\frac{Signal}{Background}$ after cuts	Net *Signal* after cuts	Percentage Net *Signal* remaining
Λ	1.24	3.77	57317 $\pm$ 319	19%
$\overline{\Lambda}$	1.20	3.57	47127 $\pm$ 285	22%
K^0_S	1.20	2.8	173194 $\pm$ 594	28%

Table 5.3: A summary of the signal to background ratios obtained before and after applying the optimised cuts. The fraction of signal remaining (derived from Figures 4.5 and 5.9) and total net number of Λ, $\overline{\Lambda}$ and K^0_S after cuts is also shown.

5.1.3 Rejection of Pile-up

The distance of closest approach of the v0 to the primary vertex cut should in principle remove the effects of pile up from the analysis. The number of net Λ, $\overline{\Lambda}$ and K^0_S candidates (calculated according to equation 5.3) per event as a function of luminosity is shown in Figures 5.10, 5.11 and 5.12. From these figures it can be seen that the net number of Λ, $\overline{\Lambda}$ and K^0_S candidates is now stable with luminosity, with the number of candidates per event for the runs which contain very little pile up (0.2 pile up events / event) equal to the number of candidates per event for where the pile up rates were far greater (1.6 pile-up event/event). These plots indicate that the Λ, $\overline{\Lambda}$ and K^0_S net yields (*Signal*) are no longer affected by the pile-up problem.

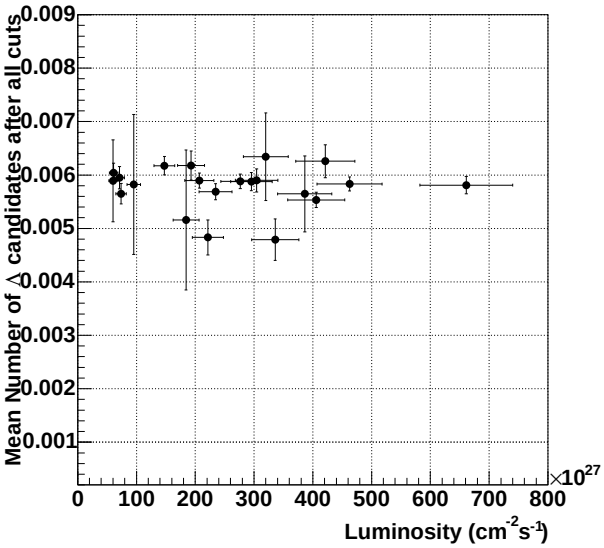

Figure 5.10: Reconstructed Λ candidates versus luminosity after all cuts.

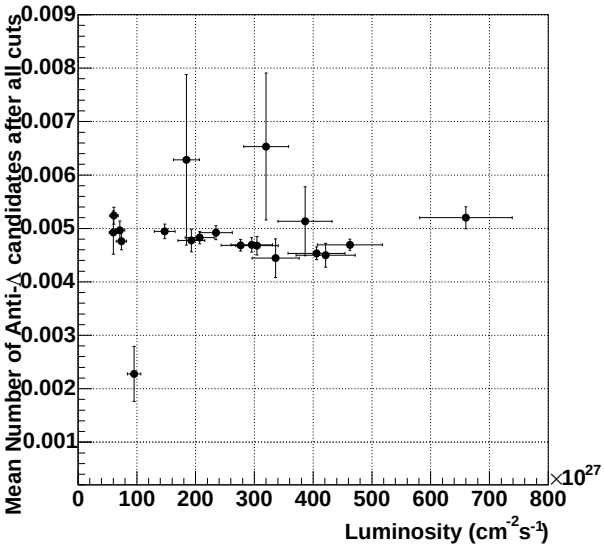

Figure 5.11: Reconstructed $\overline{\Lambda}$ candidates versus luminosity after all cuts.

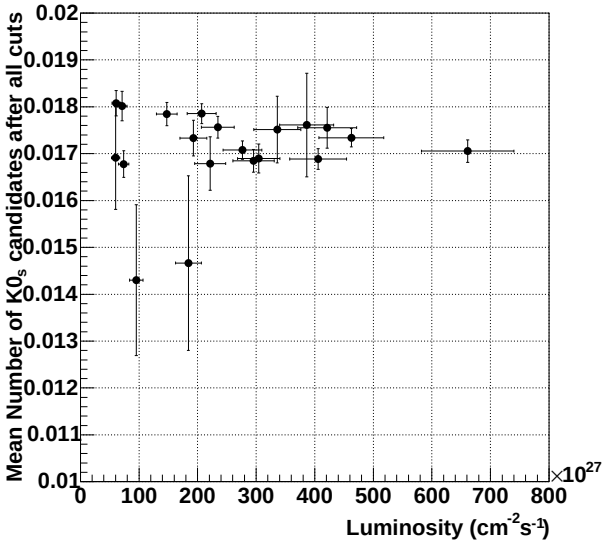

Figure 5.12: Reconstructed K^0_S candidates versus luminosity after all cuts.

It was shown in the previous section that the effects of pile up can be removed by requiring the v0 candidates to point back to the primary vertex (Figures 5.10, 5.11 and 5.12). In the event of the vertex not being found at all or the reconstruction of a false vertex, that is to say a primary vertex which is far from the real vertex, v0s will be lost to the analysis. This section details a study of the primary vertex finding efficiency and the subsequent steps which were taken to estimate the number of Λ, $\overline{\Lambda}$ and K^0_S which were lost due to the primary vertex being incorrectly determined.

5.2.1 Determining Vertex Efficiency by Simulation

The efficiency of the primary vertex finding software was investigated by embedding HIJING Monte-Carlo (MC) generated p + p events into abort-gap events (see section 3.4.3). The embedding process works by initially propagating the MC produced particles through a model of the STAR detector system using the GEANT code [77]. GEANT models the interaction with the detector materials and propagates charged particles according to the applied magnetic and electric fields. It contains accurate information on the surrounding materials, such as the detectors and P10 gas, through which the particles may propagate. As the daughter tracks propagate the amount of ionisation, and subsequent drift of the liberated electrons through the P10 gas is simulated. The effect of these ionisation electrons arriving at the read out plane is modelled by the TPC Response Simulation software (TRS). TRS also models the charge collection process at the cathode pads, as well as the digital signal generation. The purpose of this thorough simulation procedure is to convert the tracks made by the MC particles into simulated ADC counts; the hit-points that correspond specifically to the MC daughter particles are known at this stage.

The simulated ADC counts are embedded into abort-gap events. The abort-gap event provides a more realistic background environment, as in actuality v0 finding is done with a background of pile up tracks. The full reconstruction chain is then invoked, to convert the real and simulated ADC hits into a set of global and primary tracks. Event reconstruction is done using the same methods as described in Chapter 4. This leaves two versions of

includes background (or pile-up) tracks from preceding and following collisions. The z positions of the MC and reconstructed vertices were compared and a quantity Δ defined such that,

$$\Delta = z_{Monte-Carlo} - z_{Reconstructed} \tag{5.4}$$

where z relates to the primary vertex ordinate which runs parallel to the beam line. Δ is plotted in Figures 5.13 and 5.14. As can be seen in Figure 5.13 the overall range of possible Δ values is very large, indicating that the vertex finding software is not totally reliable. However, Figure 5.14 shows that most of the primary vertices are reconstructed well. Thus in most cases the found vertex is a good one, where good vertices were defined as those with $\Delta \leq 2$cm (this number is determined by where the background becomes approximately flat), shaded in blue in Figure 5.14. However, in a small number of instances $\Delta > 2$cm, and these were designated as 'fake' vertices. There are also cases where no vertex is found, and these are designated as 'not-found' vertices. The probability for these processes is summarised in Figure 5.15.

When no primary vertex is found the event is not fully reconstructed. Therefore it is important to draw a distinction between events where the vertex is fake, and not-found, as the v0 finder does not run in the latter instance. There is thus a known number of events for which there was a trigger, but for which it was impossible to count the number of v0s. The correction for the not-found vertices must add back in both the number of lost events and the number of lost v0s. If the vertex is fake, then a genuine v0 will fail to point back to the primary vertex. However, there is no way of telling if, in the real data there was a fake vertex or not, and so fake vertex events are always counted. The fake vertex correction must therefore only add back in the number of lost v0s.

5.2.2 Vertex Corrections as a Function of Multiplicity

Although the proportions of lost and fake vertices have been determined, simply scaling the measured v0 yields by the factors indicated in Figure 5.15 will not work, as the Monte-

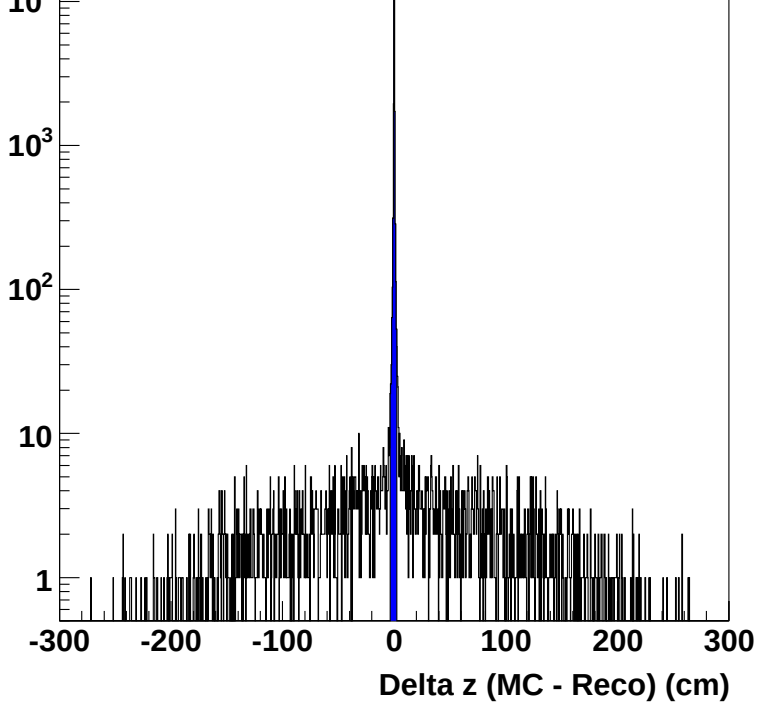

Figure 5.13: A plot of Δ as defined by equation 5.4. Although most primary vertices seem to be well reconstructed, there remain a significant number of events where the vertex reconstruction software, PPLMV, reconstructs the vertex falsely.

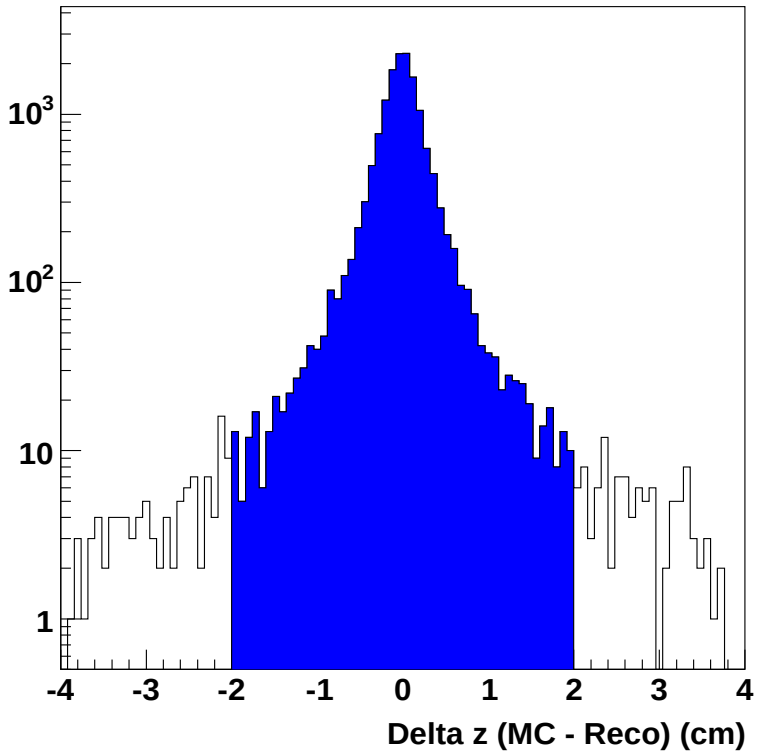

Figure 5.14: A plot of Δ as defined by equation 5.4. This plot shows that the majority of primary vertices are reconstructed well, with $\Delta \leq 2$cm.

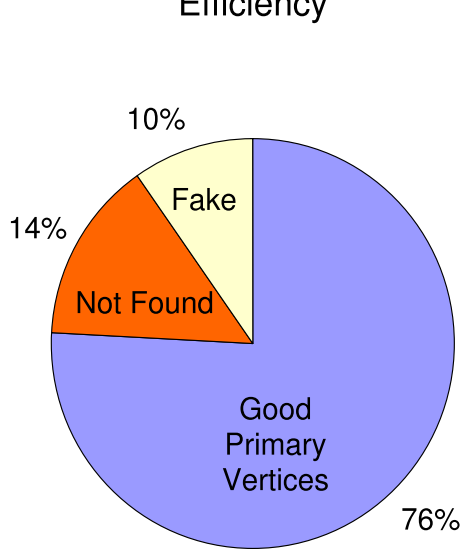

Figure 5.15: Probability for achieving an event with good, fake or not found vertex.

Carlo study showed that the vertex finding efficiency was strongly dependent on the event multiplicity. The number of Λ, $\overline{\Lambda}$ and K^0_S also increase with the event multiplicity and so the aim of the vertex correction is to determine the vertex finding efficiency as a function of multiplicity.

It is expected that the vertex finding efficiency varies as a function of the number of global tracks from the *triggered* event, rather than the overall number of tracks (including pile up tracks). Those reconstructed tracks that belong to the MC generated particles must therefore be separated from the abort-gap (background) tracks. Unfortunately the MC tracks present in the embedded event are indistinguishable from all the other tracks. Therefore track hit-point matching was performed to determine which MC generated hit-point corresponds to a hit-point on a reconstructed track. Hit-points were matched if the measured point is within 5mm of the Monte-Carlo point and tracks are said to be matched if they contain more than 15 matches.

The fraction of real events where the vertex is not found is plotted as a function of luminosity in Figure 5.16. This can be measured from the real data as the vertex finder returns a default value if the vertex is not found. The spread is much larger than the statistical error allows and it is interesting to note that the fraction does not appear to be correlated with luminosity. The abort gap events into which the Monte-Carlo particles

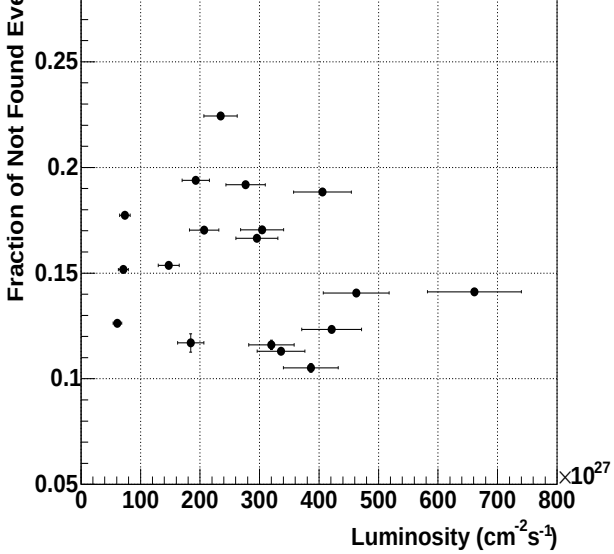

Figure 5.16: Fraction of events where the primary vertex was not found vs luminosity.

were embedded corresponded to those with a 14% not found fraction, approximately in the middle of the distribution indicated in Figure 5.16. This indicates that the sample of abort-gap events embedded into to derive the vertex correction was representative of the entire p + p run, although there may be some error in the overall event re-normalisation.

The Monte-Carlo matched global track distributions for various types of events are plotted in Figure 5.17. The probability for achieving a given type of event as a function of multiplicity is given by dividing plot a (fake vertex), b (not found vertex) or c (good vertex) by plot d (all types of event). The division is shown in Figure 5.18 which demonstrates that significant vertex reconstruction losses occur for events with low multiplicity. An empirical fit was used to parameterise the vertex reconstruction probabilities.

As v0s fail the DCA cut when the primary vertex is fake, and are not reconstructed when the primary vertex is not-found they must be added back into the analysis. If this number is to be estimated from those v0s determined when there is a good vertex we assume that there is an equal probability of generating a Λ, $\overline{\Lambda}$ or K^0_S in fake, not found and good vertex events of a given multiplicity. To check the assumption the average number of Monte-Carlo generated Λ, $\overline{\Lambda}$ and K^0_S for fake, not found, and good vertex events as a function of multiplicity were compared. An example for the Λ is shown in Figure 5.19 where the number of generated Λs per event with a certain multiplicity is compared for

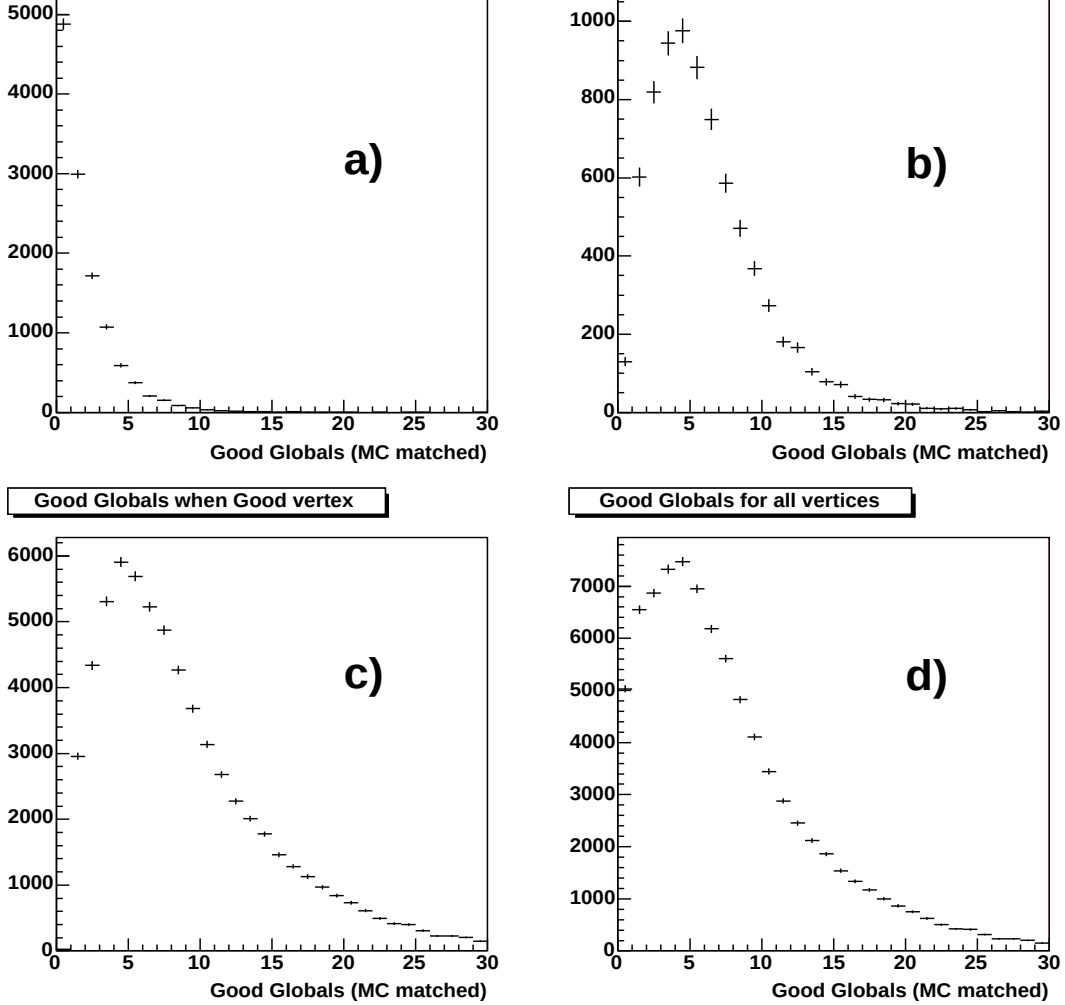

Figure 5.17: MC matched track distributions for the no vertex case (a), the fake vertex case (b), the good vertex case (c) and for all events (d).

fake and good vertices (a), and not found and good vertices (c). The number of good vertex Λs per number of events for that multiplicity is divided by the number of Λs produced in fake (Figure 5.19(b)) or not found vertex (Figure 5.19(d)) events. This gives a measure of the relative probability of producing Λs in good vertex events, compared to fake or not found vertex events. If the equal probability assumption is valid then the ratio plots in Figure 5.19(b) and 5.19(d) should be ~ 1 as a function of multiplicity. Given the statistical error, the ratio is indeed close to unity. This suggests that the Λ yield derived from events with a good primary vertex can be used to correct for the missing yield in fake vertex and not found vertex events. This was also shown to be true for the $\overline{\Lambda}$ and K^0_S.

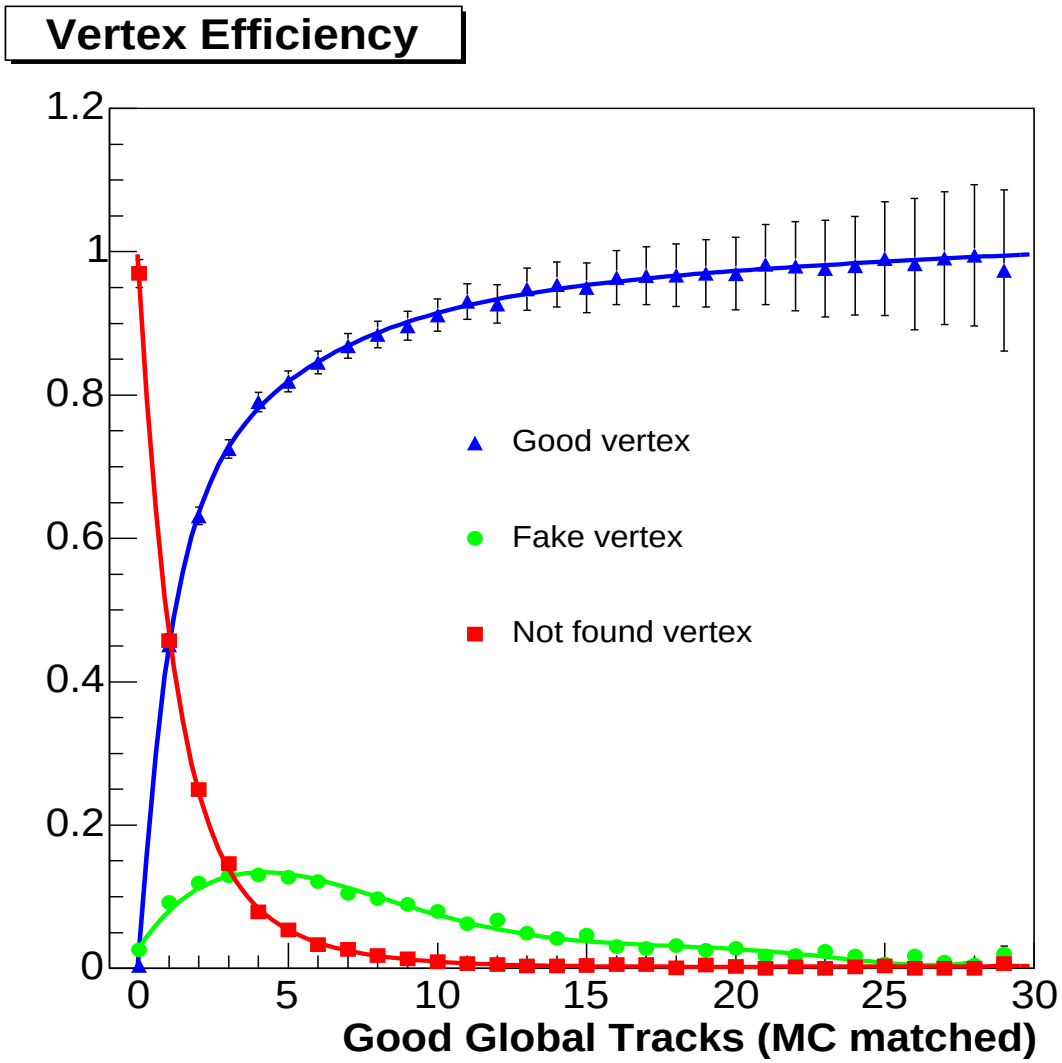

Figure 5.18: Vertex finding probability as a function of good MC matched global tracks.

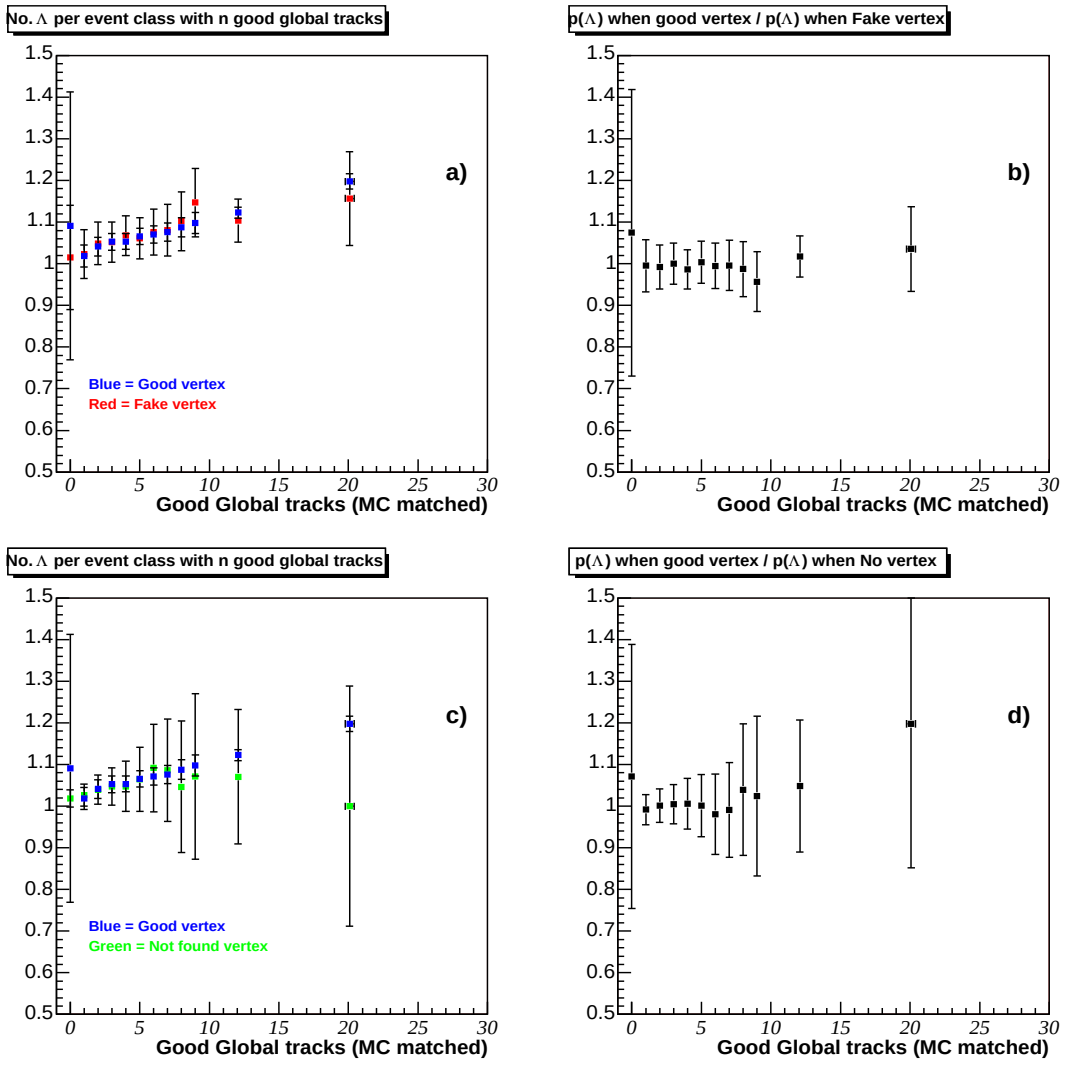

Figure 5.19: Λ generation in events with good, fake and not found vertices. Plots a) and c) compare the average number of Λs produced in fake vertex (a) or not found vertex (c) events with the average number produced in events with a good primary vertex. The corresponding ratio of good/fake and good/not found are displayed in plots b) and d). The ratios are ~ 1 as a function of multiplicity indicating that the correction can be undertaken as a function of multiplicity using the Λ yield from events where a good vertex is measured.

Unfortunately, as shown in Figure 4.4 the number of global tracks is susceptible to the effects of pile-up, and a more reliable measure of multiplicity is the number of primary tracks which appears to be stable as a function of luminosity (Figure 4.9). The number of primary tracks is therefore adopted as a measure of multiplicity, and a vertex correction must be applied as a function of primary tracks. However, as shown in Figure 5.18 the vertex correction is calculated as a function of global tracks because, predictably, the number of primary tracks associated with fake and not found vertices is always (approximately) zero.

The primary track multiplicity is correlated to the global track multiplicity, and this fact is used as the basis of a 'Track Map', which can be used to relate MC matched global tracks to MC matched primary tracks.

The first stage in relating global tracks to primary tracks is to plot a two dimensional histogram of MC matched primaries vs MC matched globals for only those events where a good primary vertex is found, as shown in Figure 5.20. This type of plot can be used to calculate the average number of globals, which correspond to an integer number of primary tracks for all events with a good primary vertex. However, Figure 5.20 would not be complete without also accounting for those events which give 'fake' and 'not-found' vertices. In each bin of the primary track distribution shown in Figure 5.20, the global track distribution must be corrected by the 'not-found' and 'fake' vertex correction factors (shown in Figure 5.18). The weighting is important, as without it a significant number of low multiplicity events are missing from the map. After the weighting process it is possible to calculate the average number of global tracks that map to an integer number of primary tracks for *all triggered events*, as shown in Figure 5.21.

An empirical fit was used to parameterise the relationship between the number of primary tracks and the mean number of global tracks, in Figure 5.21. This fit was used in conjunction with the empirical fits to Figure 5.18 (Vertex finding probabilities as a function of global tracks) in order to determine final vertex finding probability distributions as a function of matched primary track multiplicity, as presented in Figure 5.22.

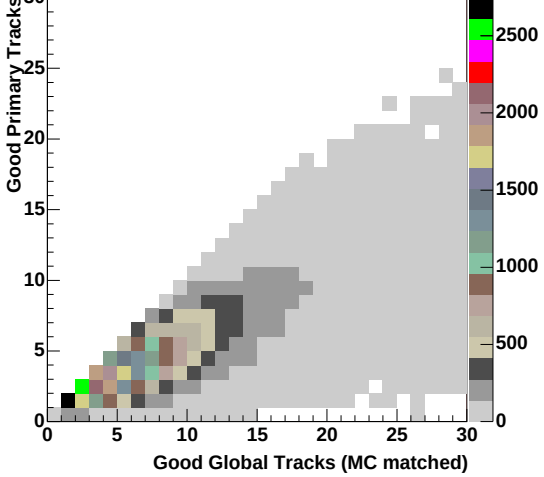

Figure 5.20: MC matched primary tracks vs MC matched global tracks.

5.2.4 Applying the Vertex Correction

The probability for achieving a good vertex is simply given by,

$$p_{good}(n_{primary}) = 1 - p_{fake}(n_{primary}) - p_{notfound}(n_{primary}) \tag{5.5}$$

where $n_{primary}$ is the primary track multiplicity, with the good, fake, and not-found vertex probabilities, $p_{good}(n_{primary})$, $p_{fake}(n_{primary})$ and $p_{notfound}(n_{primary})$ all represented in Figure 5.22. It is assumed that all genuine v0s in fake vertex events fail the DCA cut. There is, however, some probability that the fake vertex will be separated by less than 2cm from the true event vertex. By assuming the background profile in Figure 5.13 remains consistent underneath the main peak, it can be estimated that no more than 2% of "fake" vertices fall within the peak region, which was considered a negligibly small amount. The net yields for Λ, $\overline{\Lambda}$ and K^0_S are therefore corrected by only one factor, $p_{good}(n_{primary})$.

The good vertex correction factor is used to calculate a factor, $f(n_{primary})$, by which to multiply the reconstructed number of Λ, $\overline{\Lambda}$, and K^0_S, in each primary track multiplicity class (ie events with 0,1,2,3... etc primary tracks), where $f(n_{primary})$ is given by,

$$f(n_{primary}) = \frac{1}{p_{good}(n_{primary})} \tag{5.6}$$

Finally the vertex probability distributions shown in Figure 5.21 were originally deter-

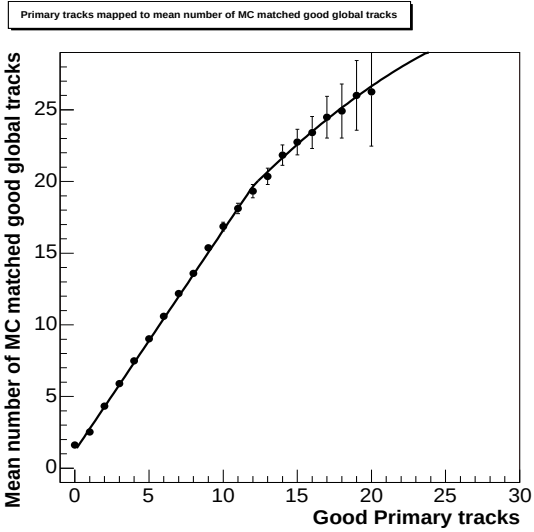

Figure 5.21: Primary tracks vs mean number of good MC matched global tracks.

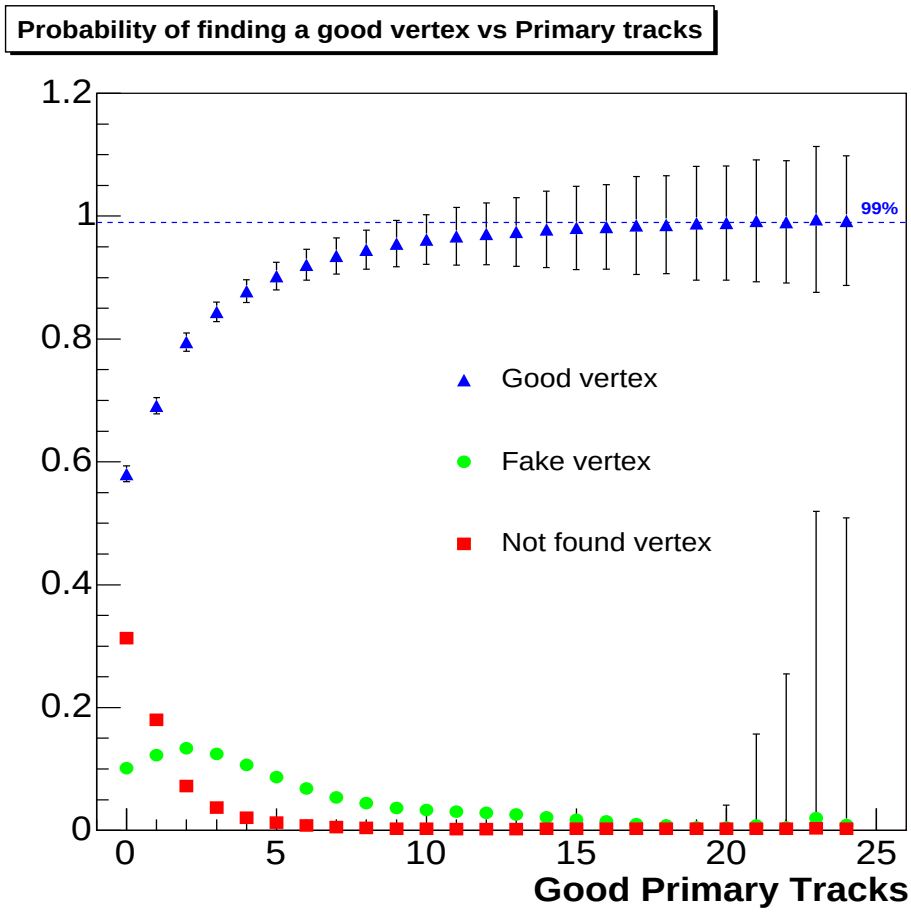

Figure 5.22: Primary vertex efficiency as a function of good primary tracks.

The corrections are to be applied as a function of the number of primary tracks as measured from the real data. Therefore it is important to show that the number of MC matched primary tracks matches the primary track distribution in the real data. The comparison was favourable as shown in Figure 5.23.

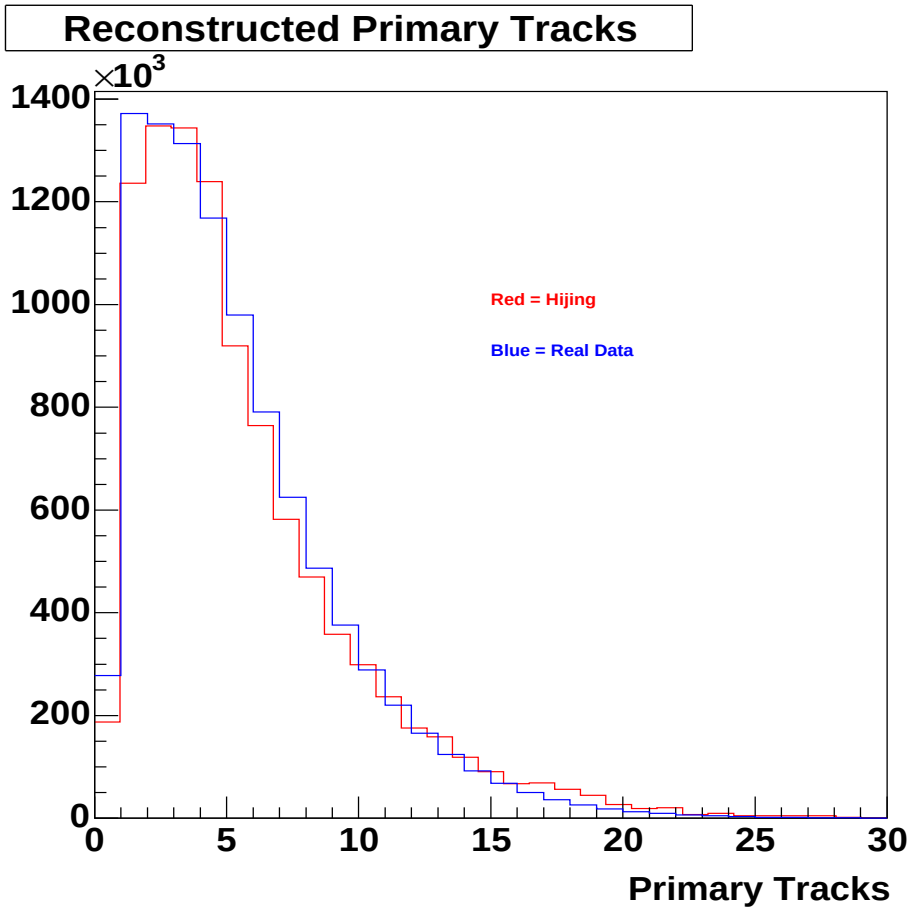

Figure 5.23: Comparison of reconstructed number of MC matched primary tracks from HIJING, and from real data

The number of events available for analysis is summarised in Table 5.4. Before an event was analysed, a series of cuts were made to ensure event quality:

- A "trigger word" cut was made to ensure a valid trigger.
- A primary vertex quality cut was made to ensure that the event was only accepted if a valid (found or fake) vertex was obtained.
- The event had to occur within ± 100cm of the TPC centre, in order to ensure good TPC acceptance.

Replacing Λ, $\overline{\Lambda}$ and K^0_S that are lost because of primary vertex finding inefficiency is the first step of the correction. The second, more basic step is in simply considering the number of lost events for which there was a trigger but for where the vertex was not found. These lost events must also be considered, as they form a valid part of the non-singly diffractive cross section for p + p collisions. The overall event re-normalisation factor was determined from the MC study to be 85.69%, and the corrected number of events, as applied when determining the final yield, is shown in Table 5.4.

No. events before event cuts	No. events after event cuts	Corrected No. Events
14.05 x10^6	10.03 x10^6	11.70 x10^6

Table 5.4: A summary of the total number of events available before and after event cuts.

It is useful to extract the yield as a function of p_T, as the p_T distribution gives information on the particle production mechanisms. Furthermore, corrections for detector acceptance and efficiency must be applied as a function of p_T, as detector acceptance is reduced for low p_T particles.

Invariant mass spectra for Λ, $\overline{\Lambda}$ and K^0_S were initially produced in p_T bins of 100 MeV; this was largely determined by statistics as the p_T resolution for Λ and K^0_S was found to be less than 100 MeV for $p_T < 2$GeV. At $p_T > 1$ GeV this binning proved to be too fine, as yield decreases with increasing p_T, and the 100 MeV bins were later recombined to produce data points with comparable statistics. Negligible statistics were available beyond 5 GeV.

Although the bin counting technique uses 'side bands' either side of the mass peak to estimate a linear background, it was observed that for some of the lowest p_T bins the background is non-linear. An alternative method is to fit the invariant mass peak, using a Gaussian + non-linear (polynomial) background function of the form,

$$f = \frac{A}{\sigma}\sqrt{2\pi}e^{-\frac{(x-\mu)^2}{2\sigma^2}} + a + bx + cx^2 + dx^3 + ex^4 \tag{5.7}$$

where σ, μ and A are the width, mean and area of the Gaussian peak respectively. The fit described by equation 5.7 is shown for the nine lowest 100 MeV p_T bins (from 0 to 900 MeV) for Λ and K^0_S, in Figures 5.24 and 5.25 respectively. In Figures 5.24 and 5.25 the background under the peaks is shown to change from being described by a non-linear function, to being linear.

Unfortunately a requirement of the primary vertex correction technique is that the v0s must not only be binned into p_T bins, but also into multiplicity bins. The vertex correction is applied as a function of multiplicity, and then the multiplicity bins are recombined back into p_T bins. However, the prospects of successfully applying meaningful fits to all bins with such low statistics are poor. As a result the bin counting technique, where the linear background assumption is implicit *had* to be used for this analysis. With bin counting the counts from the *Signal* and *Backgound* regions for the many p_T and multiplicity bins

Furthermore, it was discovered that for the K^0_S the Gaussian mass peak centre, μ, increases as a function of p_T, gradually approaching the published K^0_S mass value of 0.498 GeV/c^2 [7]. This is shown in Figure 5.26.

Clearly then it is important to examine how the net extracted signal changes with the assumption of a linear or non-linear background function. This difference between net signal extracted with the two different background assumptions is shown for the Λ in Figure 5.27. For the K^0_S the *signal* and *background* regions for the low p_T bins were adjusted so as to allow for the shift in the peak centroid, μ. The comparison of net signal extracted with linear and non-linear background assumptions for the K^0_S is displayed in Figure 5.28. Figures 5.27 and 5.28 indicate a small (relative to the statistical error) but systematic difference, especially for the Λ, that could have been considered as an error source (However, ultimately it proved insignificant compared to the overall systematic error).

It is also evident from Figures 5.24 and 5.25 that there is a low p_T cut off at 300 MeV for Λ and 100 MeV for K^0_S. This cut off is due to detector acceptance, and an extrapolation must be made in order to determine the yield from $p_T = 0$.

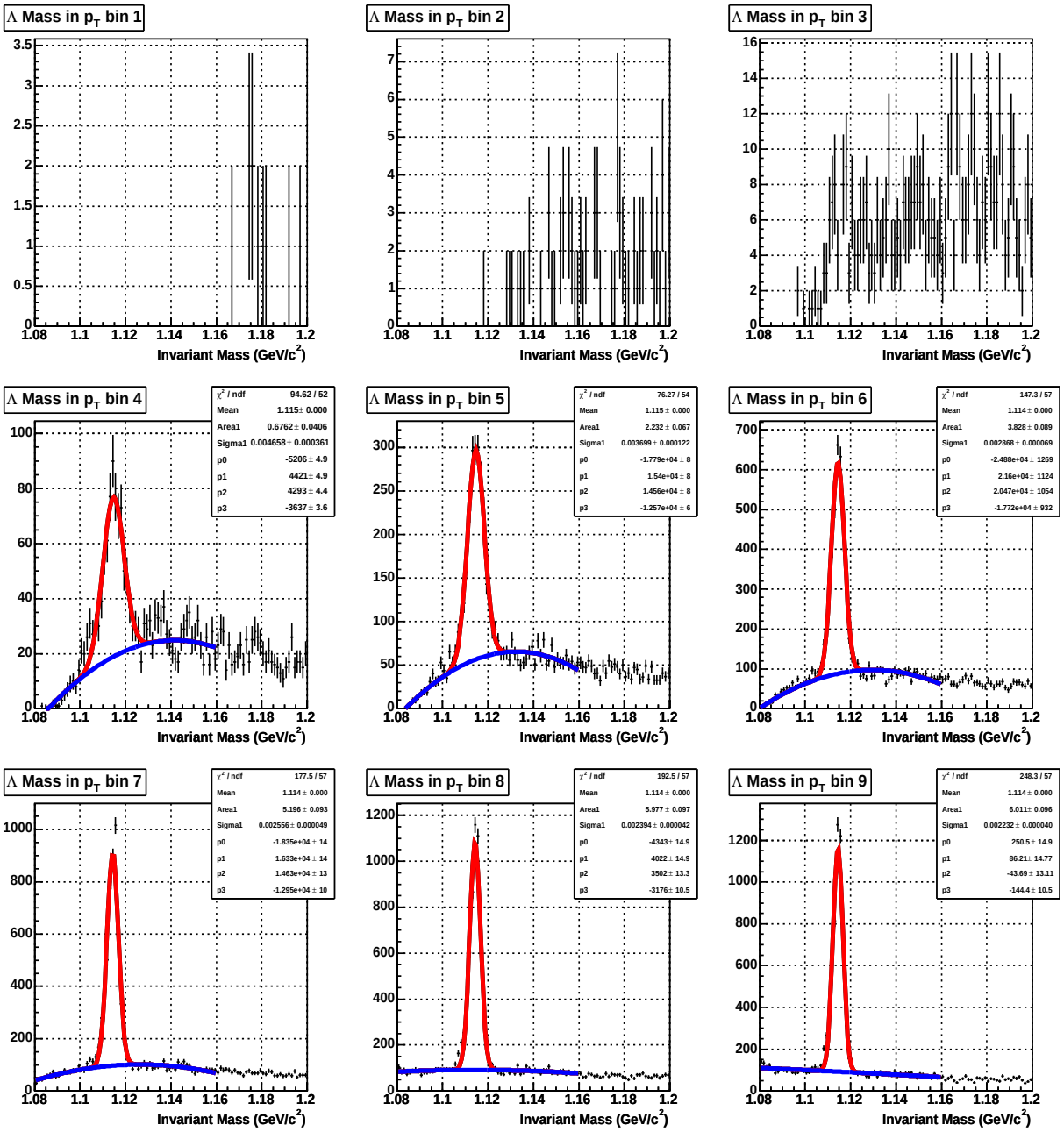

Figure 5.24: Gaussian + polynomial fits (equation 5.7) applied to Λ invariant mass spectra for the nine lowest p_T bins. Each bin is 100 MeV wide, and it is shown that the lowest available p_T bin for Λ is 300 - 400 MeV. The Polynomial background function is shown in blue, and is non-linear for bins 4,5, 6 and 7.

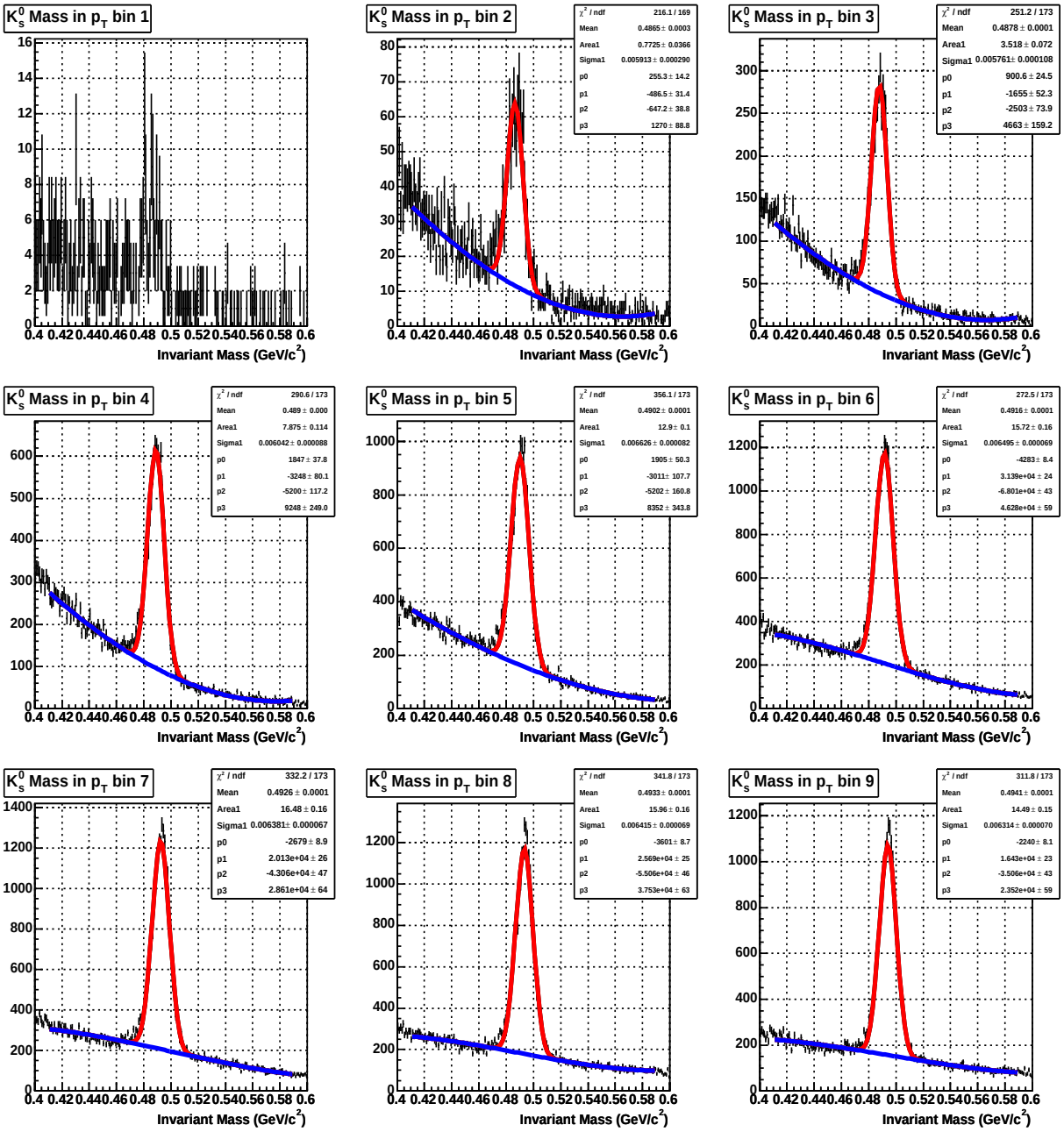

Figure 5.25: Gaussian + polynomial fits (equation 5.7) applied to K^0_S invariant mass spectra for the nine lowest p_T bins. Each bin is 100 MeV wide, and it is shown that the lowest available p_T bin for K^0_S is 100 - 200 MeV. The Polynomial background function is shown in blue, and some non-linearity is observed at low p_T.

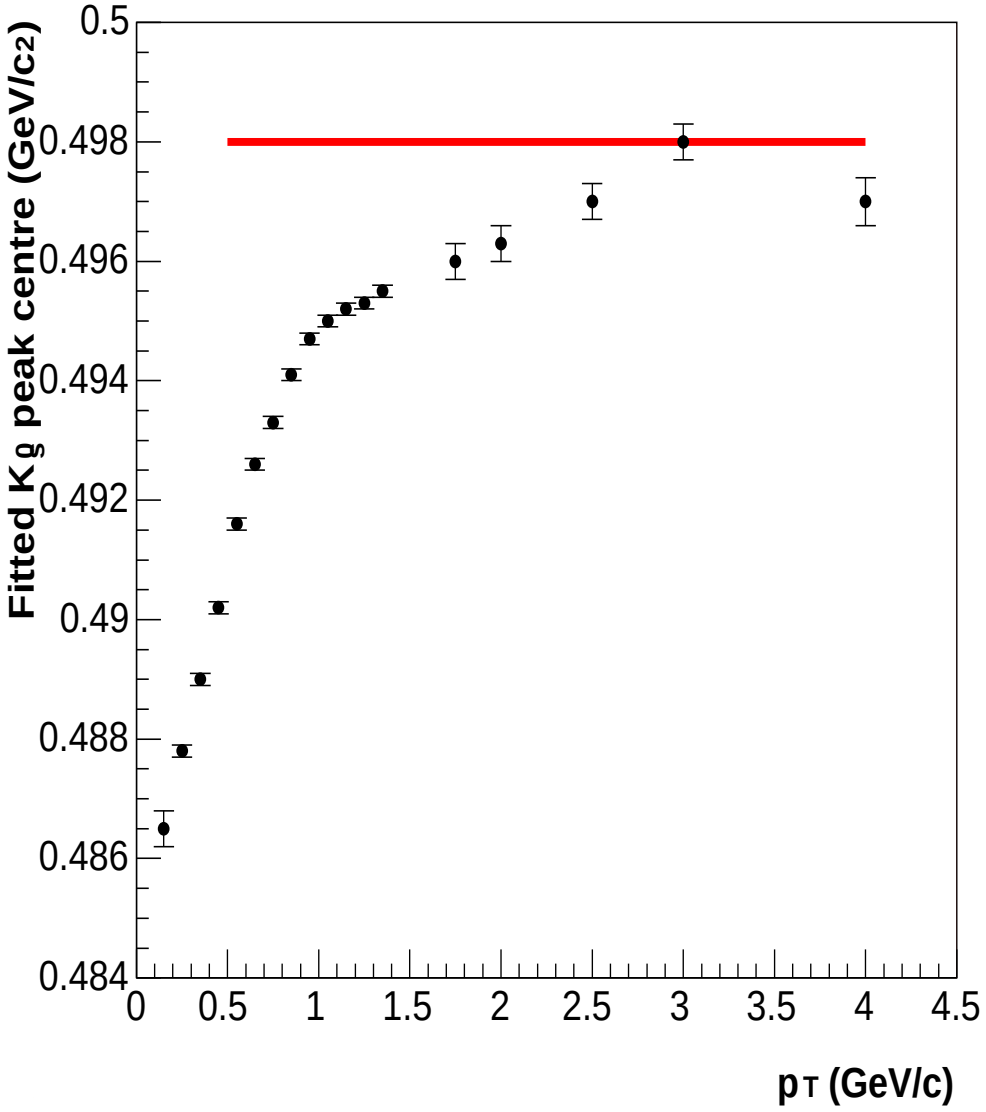

Figure 5.26: A shift in the mean K^0_S invariant mass was observed as a function of p_T. The mass value (given by the μ parameter, defined in equation 5.7) is observed to increase to the quoted value of 0.49765 GeV/c^2 (red line) [7].

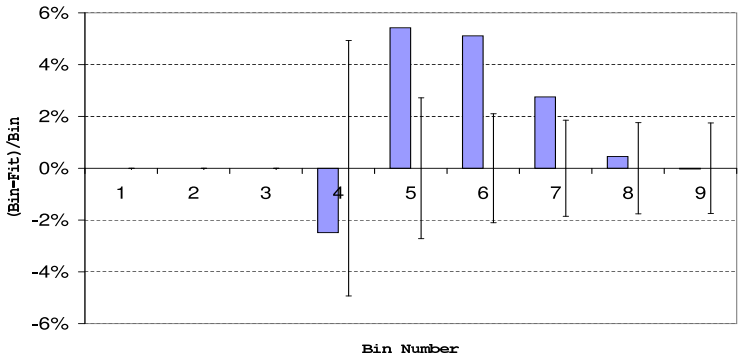

Figure 5.27: The difference as a percentage of the net signal, for the Λ by assuming a linear background compared to a polynomial background (blue bars). The statistical error is also shown.

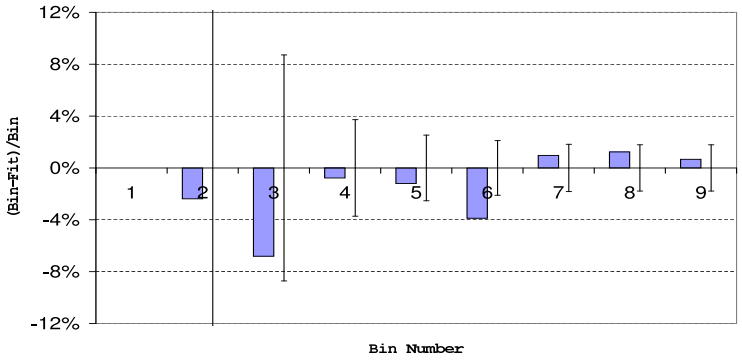

Figure 5.28: The difference as a percentage of the net signal, for the K^0_S by assuming a linear background compared to a polynomial background (blue bars). The statistical error is also shown.

The number of v0s which are reconstructed experimentally is not the total number produced in the collision, as the geometrical acceptance of the TPC and v0 reconstruction efficiency is limited. Additionally, the geometrical cuts which are applied in order to reduce the combinatorial background also reduce the raw v0 signal as shown in Table 5.3. The determination of the 'Total-efficiency' correction (the effects of acceptance and efficiency combined) as a function of p_T is discussed in this section.

As with determining the vertex finding efficiency the total correction is found by Monte-Carlo (MC) simulation. Monte Carlo particles (Λ, $\overline{\Lambda}$ and K^0_S) were randomly generated according to a certain p_T slope, using GENTX. In order to conserve computing resources, only particles which decay via the *measurable* decay channels (see Table 4.1), and which are within the STAR rapidity acceptance ($y\pm$ 1) are generated.

The correction is ultimately applied on a bin by bin basis as a function of p_T and therefore it is not vital for the p_T distribution of the MC particles to resemble that of the real particles. Two populations, with slopes which are exponential in m_T, one of low p_T particles and one of high p_T particles, were generated in order to provide good embedding statistics over the full range of measurable p_T.

For the vertex correction a realistic background environment was provided by the abort gap events, as entire HIJING p + p events were embedded into them. However, the v0 embedding correction is different as only Λ, $\overline{\Lambda}$ and K^0_S are required to be embedded in order for their efficiency to be determined. For the embedding correction real p + p events, which contain genuine and combinatorial v0 candidates as well as pile-up events are used to provide a background environment. It is important to note that all of the tracks from such real events are treated as background tracks. Each MC particle is made to originate from the reconstructed primary vertex position of an event. For real data it is impossible to know if the reconstructed vertex is fake or not, and so all MC v0s will point back to the reconstructed primary vertex, where as all genuine data v0s may not. Thus the 'Total efficiency' correction cannot account for lost v0s due to fake vertex reconstruction, which is why a seperate primary vertex correction was necessary.

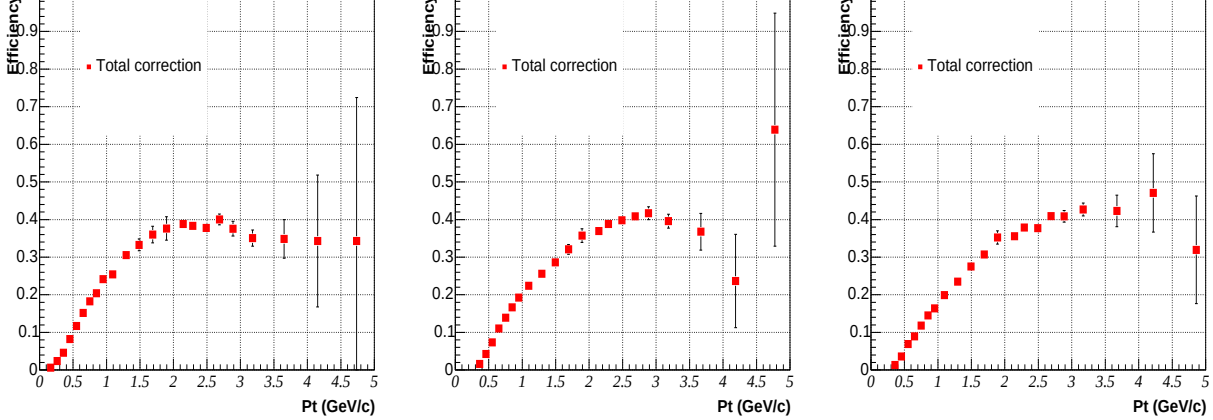

Figure 5.29: Total efficiency correction factors derived from embedding, for Λ, $\overline{\Lambda}$ and K^0_S (running from left to right). These correction factors have been multiplied by the appropriate branching fraction.

The MC particles are decayed and propagated from the reconstructed primary vertex, through the STAR detector system using the GEANT simulation code. The next stage is the actual "embedding" process, where the simulated ADC counts are mixed with those ADC counts from the real event. This new embedded event is then reconstructed in the same way as any normal real event (Chapter 4). As with the vertex correction, the MC tracks present in the embedded event are indistinguishable from all the other tracks. The process of hit matching, mentioned in section 5.2 is used to relate the original MC hit points and the reconstructed hit points. In order to match with an MC v0 particle, a reconstructed v0 must have a minimum of 15 matched hits on both of its daughter tracks; such a matched v0 is called an associated v0.

The real event, and the embedded event *should* be very similar, as essentially they differ by only the one MC embedded v0, with the properties of both the original MC v0s and associated v0s known. The same cuts which are applied to the data were applied to the associated v0 daughters (Table 5.2). The number of associated v0s which pass the geometrical cuts, N(y, p_T), and the number which were originally generated, MC(y, p_T), are then used to determine the total efficiency correction factor, C(y, p_T),

$$C(y, p_T) = \frac{N(y, p_T)}{MC(y, p_T)} \tag{5.8}$$

In order to account for the other decay modes, $C(y, p_T)$ should be multiplied by the

100,000 'High p_T' p + p minimum-bias events were embedded into for Λ, $\overline{\Lambda}$ and K^0_S. The total correction factors for Λ, $\overline{\Lambda}$ and K^0_S are shown in Figure 5.29.

The correction factors were shown to not vary with event multiplicity for Λ, $\overline{\Lambda}$ and K^0_S. This considerably simplified the analysis, as the same total correction factor (those shown in Figure 5.29) could be used to correct the data as a function of p_T, regardless of event multiplicity.

Chapter 6

Consistency checks, Errors and Fits

This chapter describes checks made to ensure the validity of corrections applied to the raw data. Also described are the fits made in order to estimate the unmeasured yield at low p_T and the treatment of statistical and systematic errors incurred by correcting and fitting the data. Finally a correction is made for Λ 'feed-down', where the yield of measured Λ and $\overline{\Lambda}$ is enhanced due to the decay of the doubly strange Ξ particle into 'secondary' Λs.

6.1 Checking the Correction

Although a similar embedding technique had been used for analyses of strange particles produced in high energy Au + Au collisions using the STAR detector (see for example [78]), it was important to confirm that the embedding correction was applicable to p + p collisions. In particular it was thought that by adding one extra MC v0 to the p + p events and then reconstructing that event that the reconstructed primary vertex may be shifted relative to the original primary vertex. This is because the MC v0 daughter tracks are secondary and do not point back to the primary vertex. For Au + Au collisions no shift was observed, but in that instance the new MC tracks were being added to many hundreds. For p + p collisions one MC v0 is embedded per event and so two new MC charged tracks, which do not point back to the primary vertex, are being added to events where the average multiplicity is ~ 5.

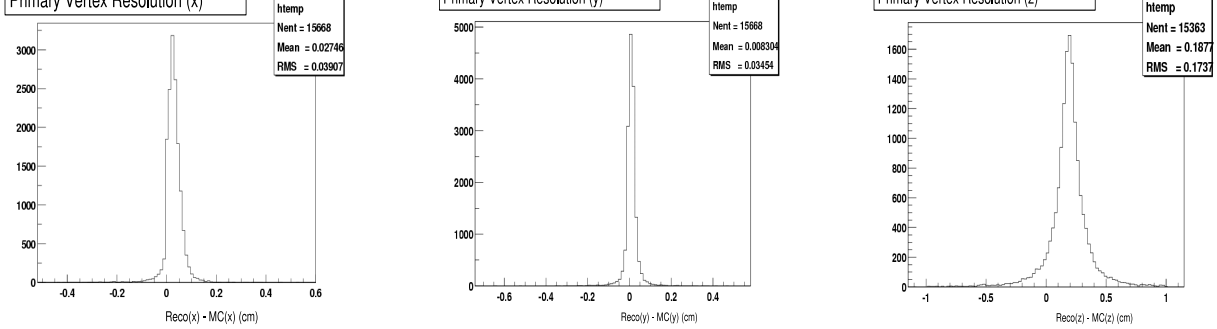

Figure 6.1: Primary vertex resolutions (in cm) in x, y and z (running from left to right). These plots show that adding one extra MC V0 to an event does not significantly perturb the vertex finding process.

The differences in x, y and z, between the primary vertex that was originally reconstructed and the primary vertex reconstructed from the embedded event containing the MC v0 are shown in Figure 6.1. Geometric cuts which utilise the primary vertex information, such as the decay length and distance of closest approach to the primary vertex cuts may be affected by an incorrectly determined primary vertex. Both of these cuts were set to 2cm, much larger than the widths of the peaks displayed in Figure 6.1. Although the apparent shift in the distribution for z was not fully understood, it was believed that as it was small in comparison to the cut values, its effect would be insignificant. However, cut studies were performed in order to determine how sensitive the final corrected yield was to changes in the the decay length and distance of closest approach to the primary vertex cuts (see section 6.5).

The embedding correction is supposed to account for those Λ, $\overline{\Lambda}$, and K^0_S candidates which are lost due to efficiency and detector acceptance effects and also because of the geometrical cuts which are applied (see Table 5.3). Therefore it is important that the cut distributions of the associated v0s from the embedding match those from the real data. Of course it is impossible to know if a Λ, $\overline{\Lambda}$ or K^0_S from the real data is genuine as there is always background contribution under the peak. When comparing the cut distributions, the cut distribution from the background regions of the invariant mass spectra have been subtracted from the cut distributions from the signal regions. Examples of the comparisons made are shown in Figures 6.2 and 6.3 (for Λ). The data and embedded v0 cut distributions are in very good agreement apart from the distance of closest approach

in the real data sample, there are contributions from secondary v0s from weak decays which are not present in the embedding. This effect is called feed-down, and for the Λ comes from the decay of doubly and triply strange hyperons such as the Ξ^-, Ξ^0 and the Ω. Feed-down effects are discussed in section 6.7.

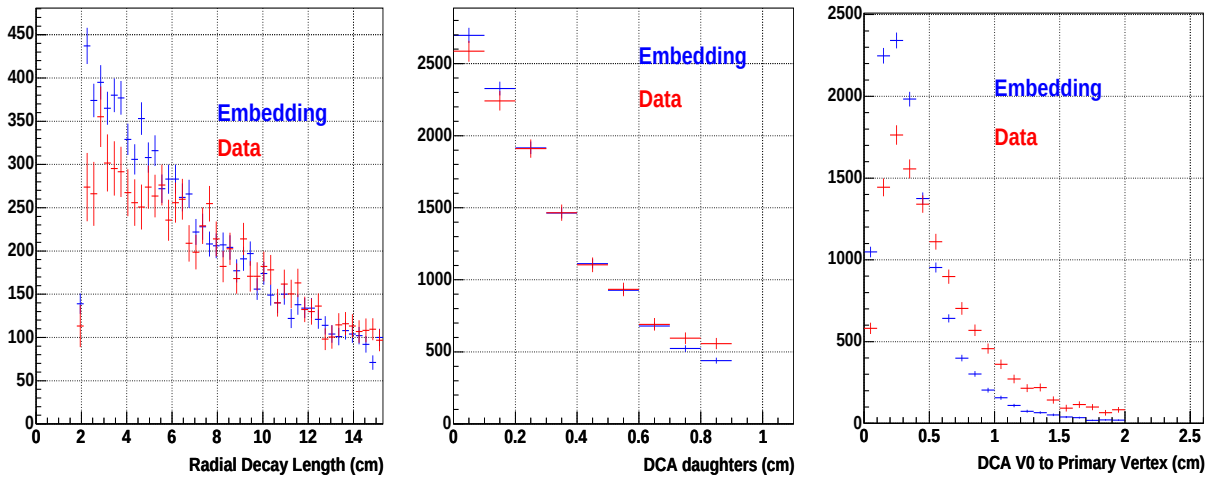

Figure 6.2: Comparison of cut distributions from data and embedding for Λ.

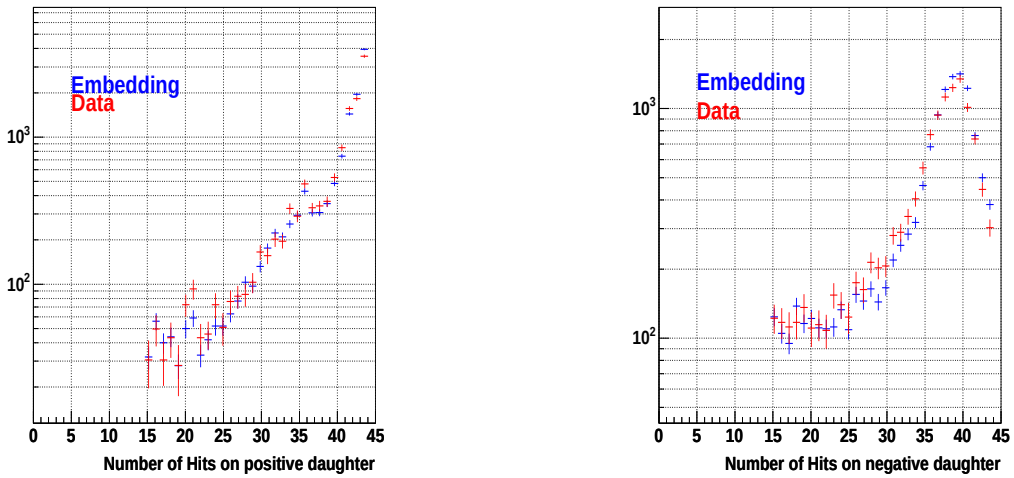

Figure 6.3: Comparison of no. of hit points on v0 daughters from data and embedding for Λ.

A further self consistency check is to determine the mean lifetime ($c\tau$) of Λ, $\overline{\Lambda}$ and K^0_S, as this is a well known quantity [7], and requires the use of the embedding to correct the raw data. The mean lifetime of a particle, $c\tau$ (measured in cm) may be calculated according to,

$$c\tau = \frac{mD_L}{p} \tag{6.1}$$

where m is the particle mass, D_L is the decay length and p is the total momentum. The raw data is corrected as a function of momentum and lifetime $c\tau$, as the measured $c\tau$ of a particle depends on momentum, and the momentum distributions are different in the real data and the embedding. An example of a corrected momentum vs $c\tau$ plot is shown in Figure 6.4. A projection can be made to the lifetime axis, in order to get the lifetime distribution for K^0_S, Λ and $\overline{\Lambda}$, as shown in Figure 6.5. An exponential fit is then applied over the range where the coverage in momentum-lifetime space (Figure 6.4) is most uniform, and the slope gives the value of $c\tau$.

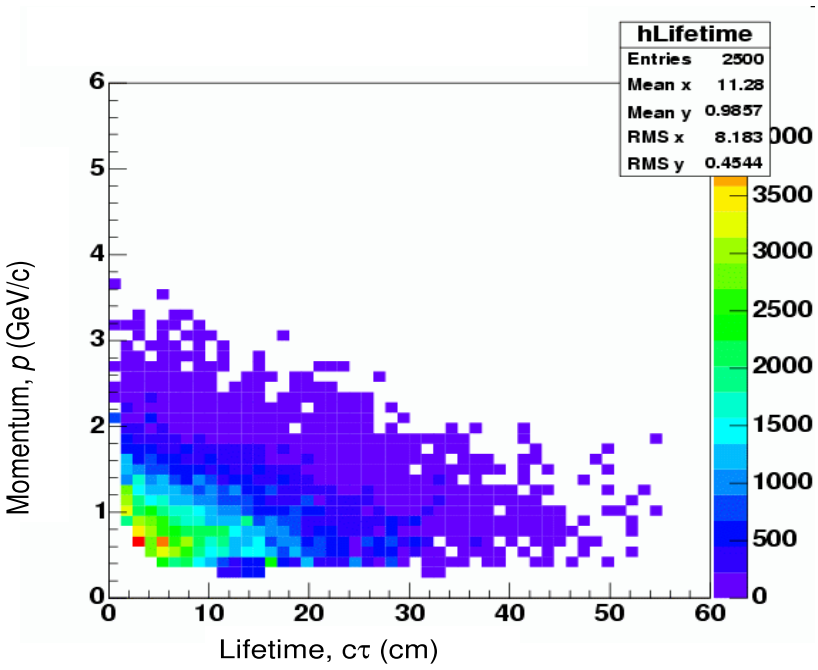

Figure 6.4: Corrected plot of Λ momentum, p, vs lifetime ($c\tau$).

more than 1 σ from the established value of 7.89cm [7]. The measured K^0_S lifetime of 2.66 $\pm$ 0.06 cm agrees much better with the measured lifetime of 2.68 cm [7]. This finding concurs well with the above postulate that the real Λ and $\overline{\Lambda}$ spectra includes contributions from secondary Λs and $\overline{\Lambda}$s, which will increase the apparent lifetime of the Λ and $\overline{\Lambda}$ if their decay length is calculated with respect to the primary vertex.

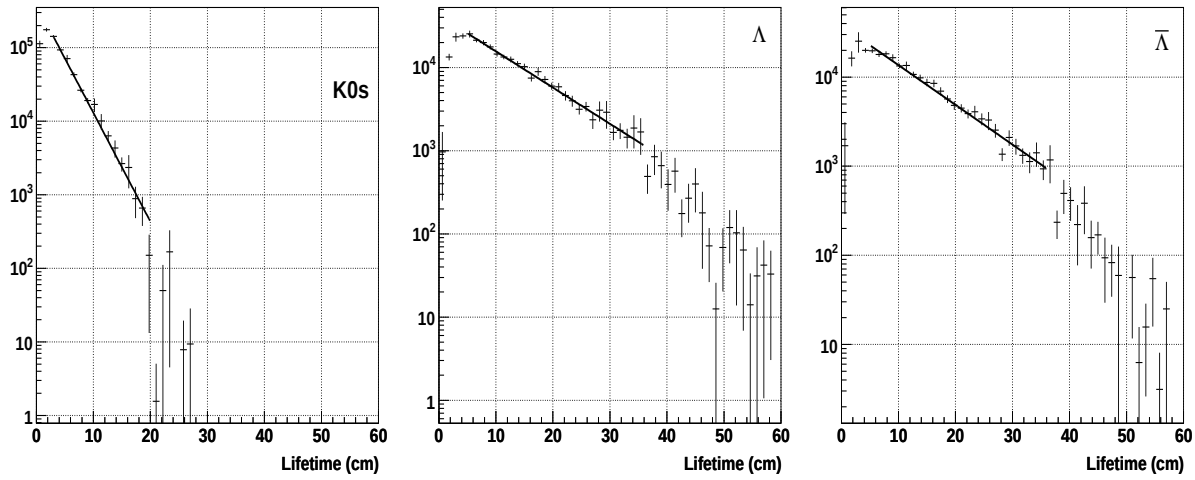

Figure 6.5: Corrected lifetime ($c\tau$) distributions (in cm) for K^0_S, Λ and $\overline{\Lambda}$.

The yield (dN/dy over $|y| < 0.5$) of K^0_S and Λ, $\overline{\Lambda}$ as a function of p_T are plotted in Figures 6.6, 6.7 and 6.8 respectively. These figures are derived by first applying the vertex correction as a function of multiplicity, and then applying the embedding correction as a function of p_T. The point to point errors in Figures 6.6 to 6.8 are statistical only, and determined by assuming Poissonian statistics for the net yields and embedding correction factors extracted using the bin counting technique. This is to say that if N counts are counted in either a *Signal* or *Background* bin then the error on that count is $\sqrt{N}$, with standard methods of error propagation being used to derive the final statistical error [79].

The simplest results which can be determined from such spectra are the yield and $\langle p_T \rangle$ determined by only considering the corrected yield in those p_T bins which were measurable as shown in Table 6.1. It is useful to present the results in this way as they are independent of any assumptions made by fits which may be used to extrapolate over the unmeasured p_T region. As this was the first analysis within the STAR collaboration to employ a vertex correction for v0s, Table 6.1 also shows the yield and $\langle p_T \rangle$ if estimated 'lost' numbers of Λ, $\overline{\Lambda}$ and K^0_S are not added back in to the analysis.

Particle	$\frac{dN}{dy}$	$\langle p_T \rangle$ (GeV/c)	$\frac{dN}{dy}_{NoVTXCOR}$	$\langle p_T \rangle_{NoVTXCOR}$
Λ (0.3 $\rightarrow$ 5.0 GeV)	0.0352 $\pm$0.0007	0.877 $\pm$0.015	0.0324 $\pm$0.0006	0.883 $\pm$0.015
$\overline{\Lambda}$ (0.3 $\rightarrow$ 5.0 GeV)	0.0316 $\pm$ 0.0007	0.864 $\pm$ 0.015	0.0301 $\pm$ 0.0006	0.869 $\pm$0.015
K^0_S (0.1 $\rightarrow$ 5.0 GeV)	0.124 $\pm$ 0.003	0.637 $\pm$ 0.014	0.113 $\pm$ 0.003	0.642 $\pm$ 0.014

Table 6.1: A summary of the Yield and $\langle p_T \rangle$ over the measured p_T range ($|y| < 0.5$). The numbers are from the non feed-down corrected spectra, and the errors quoted are statistical only.

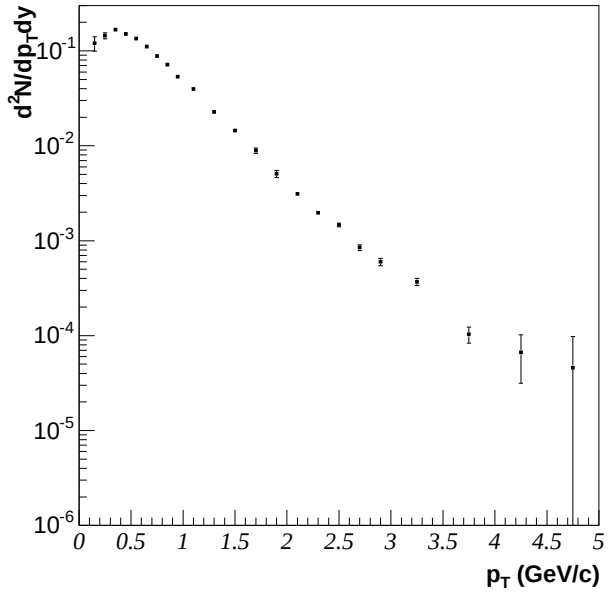

Figure 6.6: K^0_S yield as a function of p_T ($|y| < 0.5$).

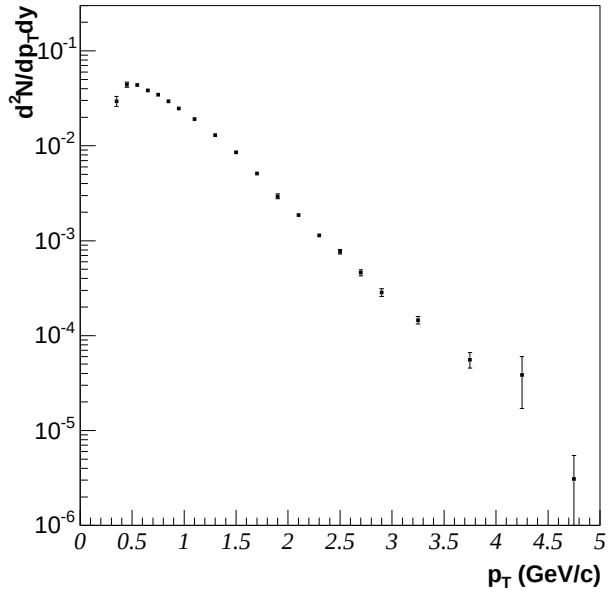

Figure 6.7: Λ yield as a function of p_T ($|y| < 0.5$).

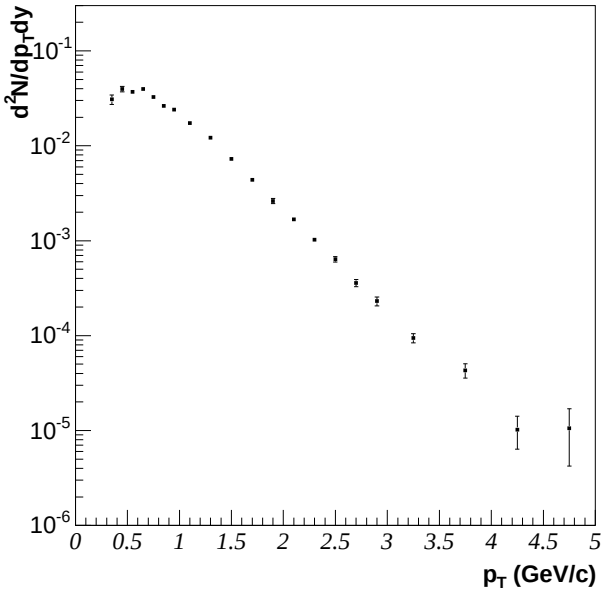

Figure 6.8: $\overline{\Lambda}$ yield as a function of p_T ($|y| < 0.5$).

The results summarised in Table 6.1 indicate that the vertex correction has only a small, $\sim 5\%$ to 10%, effect on the final dN/dy values. However, the largest systematic involved in applying the vertex correction is the total event re-normalisation. The re-normalised number of events, determined from the MC study is shown in Table 5.4. However, Figure 5.16 suggests an uncertainty in the overall re-normalisation factor. The spread is not correlated with luminosity, and is not fully understood. Thus the error in the re-normalisation factor was estimated by using,

$$\sigma_{sys} = \sqrt{\frac{(x_{default} - x)^2}{N-1}} \tag{6.2}$$

where $x_{default}$ is the 0.143 fraction from the MC study, and the x values are those obtained from the data (Figure 5.16). The systematic error on dN/dy indicated by the overall event re-normalisation is $\pm$ 4.1%.

6.5 Cut Studies

Various detector and reconstruction effects which are not accounted for in the reconstruction chain may be the source of additional error. For example, although the embedding correction process is designed to faithfully reproduce every aspect of v0 reconstruction, the correction is inevitably imperfect. This is indicated in the section 5.4, where although the embedding tests gave satisfactory results, reproducing the cut distributions seen in the data, there were notable discrepancies; particularly in the comparison of the DCA of the v0 to the primary vertex distributions (Figure 6.2) and also in the calculation of Λ and $\overline{\Lambda}$ lifetimes. Although these effects may be due to feed-down, it is important to test the sensitivity of the yield and $\langle p_T \rangle$ to variations in the cut parameters. Also, some indication of the systematic error may be given by determining the dN/dy and the $\langle p_T \rangle$, over the measurable p_T range for a variety of different cuts sets, shown in Table 6.2.

Exploiting the azimuthal symmetry of the TPC, the dN/dy and $\langle p_T \rangle$ was studied as a function of azimuthal angle ϕ, in four quadrants around the TPC's major axis. The

set	daughters(cm)	decay length(cm)	primary vertex(cm)	hit points
1 (default)	0.9	2.0	2.0	15
2	0.9	0.0	2.0	15
3	1.5	2.0	2.0	15
4	0.5	2.0	2.0	15
5	0.9	4.0	2.0	15
6	0.9	2.0	1.8	15
7	0.9	2.0	2.2	15
8	0.9	2.0	2.0	17
9	0.9	2.0	2.0	13
10	0.9	1.0	2.0	15

Table 6.2: Different cut parameters used for determining systematic error.

dN/dy and $\langle p_T \rangle$ were also measured with the TPC magnet operating in forward (FFF) and reverse full field (RFF) mode. The yield and dN/dy were expected to be the same in all quadrants, and for all field settings, and so the variations should give a measure of systematic error. The variations in dN/dy for K^0_S and Λ are plotted in Figures 6.9 and 6.10.

Although the variations in dN/dy and $\langle p_T \rangle$ due to these systematic are all within 3 σ of the statistical error, one may expect there to be much less variation, as all measurements are derived from the same data set. Therefore the systematic error on dN/dy and $\langle p_T \rangle$ (a quantity x) were determined according to equation (6.2) with $x_{default}$ representing that value of $\langle p_T \rangle$ or dN/dy corresponding to that value measured using the optimised (default) cut set. The systematic errors calculated for K^0_S and non feed-down corrected Λ are summarised in Table 6.3. The systematic error for the $\overline{\Lambda}$ was assumed to be equal to that of the Λ, due to the similar nature of the analyses.

Particle	$\frac{dN}{dy}$	$\langle p_T \rangle$
Λ (0.3 $\rightarrow$ 5.0 GeV)	2.8 %	0.8 %
K^0_S (0.1 $\rightarrow$ 5.0 GeV)	2.6 %	1.1 %

Table 6.3: A summary of systematic errors for Λ and K^0_S, incurred by changing cuts, by using different field settings, and by restricting acceptance to each of the 4 TPC quadrants in turn.

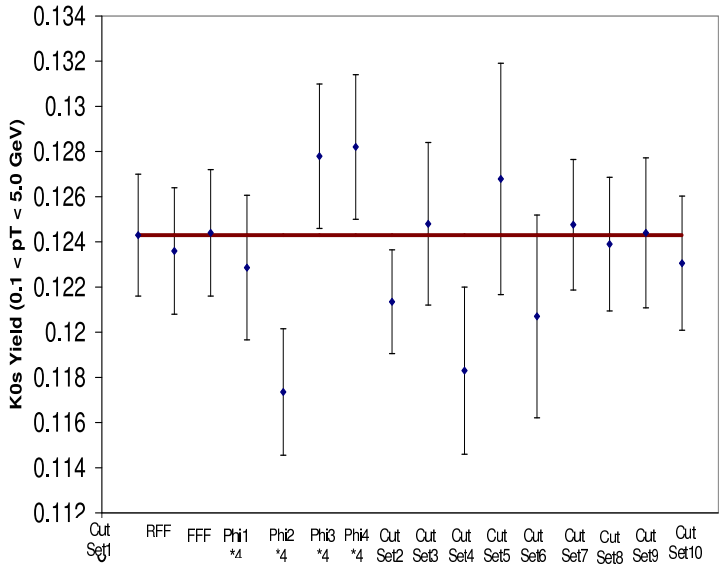

Figure 6.9: K^0_S yields for different cut sets, ϕ and magnetic field settings.

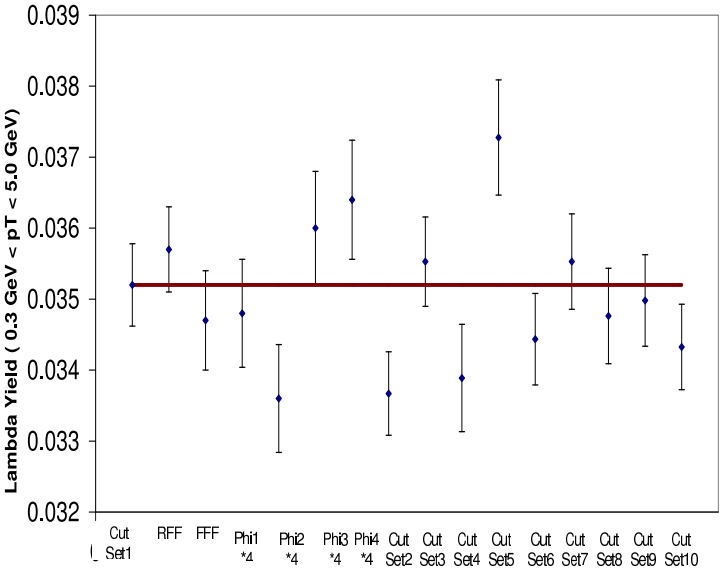

Figure 6.10: Λ yields for different cut sets, ϕ and magnetic field settings.

Fitting the p_T spectra is a vital part of the analysis, as it enables extrapolations to be made over the low p_T region of the spectra where there was no acceptance. However, in order to believe the extrapolation the fit must have some theoretical basis. In heavy ion analyses it is common to use an m_T exponential function inspired by a thermal description of the emitting source [35],

$$\frac{1}{2\pi p_T}\frac{d^2N}{dydp_T} = Ae^{\frac{-m_T}{T}} \tag{6.3}$$

where A is a constant and T is the temperature. There is also the pQCD inspired power law function described by equation 2.3. Hagedorn showed that equation 2.3 may be re-written as [35],

$$\frac{1}{2\pi p_T}\frac{d^2N}{dydp_T} = B\left(1+\frac{2p_T}{(n-3)<p_T>}\right)^{-n} \tag{6.4}$$

where B and n are constants. The UA1 experiment observed that, for Λ and $\overline{\Lambda}$ the p_T spectra is harder than that of K^0_S, with the effect of pushing n in the power law (equation 6.4) to ∞. This was also observed for this analysis and so, therefore, in effect an exponential in p_T, as shown in equation 6.5 was used to fit the Λ and $\overline{\Lambda}$ spectra,

$$\frac{1}{2\pi p_T}\frac{d^2N}{dydp_T} = Ae^{\frac{-p_T}{T}} \tag{6.5}$$

As pointed out by Hagedorn [35], spectra may contain contributions from both thermal emission, represented by equation 6.3 and the pQCD inspired power law model represented by equation 6.4. As such a composite equation is represented by,

$$\frac{1}{2\pi p_T}\frac{d^2N}{dydp_T} = Ae^{\frac{-m_T}{T}} + B\left(1+\frac{2p_T}{(n-3)<p_T>}\right)^{-n} \tag{6.6}$$

as for the Λ and $\overline{\Lambda}$ $n \to \infty$ and equation 6.6 becomes,

$$\frac{1}{2\pi p_T}\frac{d^2N}{dydp_T} = Ae^{\frac{-m_T}{T}} + Be^{\frac{-p_T}{T}} \tag{6.7}$$

$$\frac{1}{2\pi p_T}\frac{d^2N}{dydp_T} = (A.e^{\frac{-m_T}{T}})_{p_T<x} + \left(B\left(1+\frac{2p_T}{(n-3)<p_T>}\right)^{-n}\right)_{p_T>x} \tag{6.8}$$

where *only* the m_T exponential (equation 6.3) is applied at low p_T values (< x) and *only* the pQCD inspired power law (equation 6.4) is applied at large p_T values (> x). The parameter x is made to vary as a free parameter. Equation 6.8 requires the additional condition that the slopes of its two composite parts are continuous at the join point, x. The n parameter does not tend to ∞ for equation 6.8.

The fits were performed using a χ^2 minimisation procedure [81], and are displayed in Figures 6.11 to 6.16. The mid-rapidity yield for $|y| < 0.5$ was extracted by integrating, from $p_T = 0$, the fit function $f(p_T)$,

$$dN/dy = 2\pi \int_0^\infty p_T f(p_T) dp_T \tag{6.9}$$

and similary the $\langle p_T \rangle$ was extracted by using,

$$<p_T> = \frac{\int_0^\infty p_T f(p_T) dp_T}{\int_0^\infty f(p_T) dp_T} \tag{6.10}$$

except for equation 6.4 where $\langle p_T \rangle$ is one of the fit parameters. The dN/dy and $\langle p_T \rangle$ were extracted from the best fits of equations 6.3 to 6.8 to the spectra and are presented in Table 6.4, together with the χ^2/DF, where DF is the number of degrees of freedom. It can be seen that equations 6.3 and 6.4, previously used to describe heavy ion and $\mathrm{p} + \overline{\mathrm{p}}$ spectra do not describe the data as well as the composite forms described by equations 6.6, 6.7 and 6.8.

The composite functions described by equations 6.6, 6.7 and 6.8., gave similar χ^2/DF and so were used to determine an estimate of the error in the extrapolation over the unmeasured p_T region. The extrapolation over these p_T regions is shown more clearly in Figures 6.17, 6.18 and 6.19. The systematic error estimated from taking the difference between these fits is summarised in Table 6.5. The seperate contributions to systematic error (from the vertex correction (4.1% to dN/dy), the cut study (Table 6.3) and the fit

Particle	(Eq'n 6.3)	(Eq'n 6.4 (K^0_S)) (Eq'n 6.5) (Λ,$\overline{\Lambda}$)	(Eq'n 6.8)	(Eq'n 6.6 (K^0_S)) (Eq'n 6.7 (Λ,$\overline{\Lambda}$))
Λ χ^2/DF	193/19	73/19	27/15	20/17
$\overline{\Lambda}$ χ^2/DF	166/19	77/19	23/15	21/17
K^0_S χ^2/DF	425/21	52/20	23/17	18/18
Λ dN/dy	0.0366	0.0476	0.0403	0.0414
$\overline{\Lambda}$ dN/dy	0.0342	0.0446	0.0376	0.0389
K^0_S dN/dy	0.107	0.138	0.126	0.129
Λ $\langle p_T \rangle$ (GeV/c)	0.833(T=0.272)	0.692	0.776	0.762
$\overline{\Lambda}$ $\langle p_T \rangle$ (GeV/c)	0.819(T=0.273)	0.679	0.766	0.749
K^0_S $\langle p_T \rangle$ (GeV/c)	0.702(T=0.291)	0.581	0.626	0.612

Table 6.4: Results from fitting equations 6.3 to 6.8 to p_T spectra. All yields and $\langle p_T \rangle$ are for $|y| < 0.5$.

Particle	$\frac{dN}{dy}$	$\langle p_T \rangle$
Λ	2.7 %	1.8 %
$\overline{\Lambda}$	3.3 %	2.3 %
K^0_S	2.3 %	2.3 %

Table 6.5: Systematic error incurred by extrapolating the composite fit equations over the un-measurable p_T regions for Λ, $\overline{\Lambda}$ and K^0_S.

extrapolation (Table 6.5)) are assumed as being independent and are therefore added in quadrature in order to derive the final systematic for the final dN/dy and $\langle p_T \rangle$ of K^0_S and non-feed-down corrected Λ and $\overline{\Lambda}$, summarised in Table 6.6.

Particle	dN/dy	$\langle p_T \rangle$ (GeV/c)
Λ	$0.0414 \pm 0.0008_{stat} \pm 0.0024_{syst}$	$0.762 \pm 0.022_{stat} \pm 0.015_{syst}$
$\overline{\Lambda}$	$0.0389 \pm 0.0008_{stat} \pm 0.0023_{syst}$	$0.749 \pm 0.022_{stat} \pm 0.018_{syst}$
K^0_S	$0.129 \pm 0.003_{stat} \pm 0.007_{syst}$	$0.612 \pm 0.020_{stat} \pm 0.015_{syst}$

Table 6.6: A summary of dN/dy and $\langle p_T \rangle$ for Λ, $\overline{\Lambda}$ (non feed-down corrected) and K^0_S ($|y| < 0.5$).

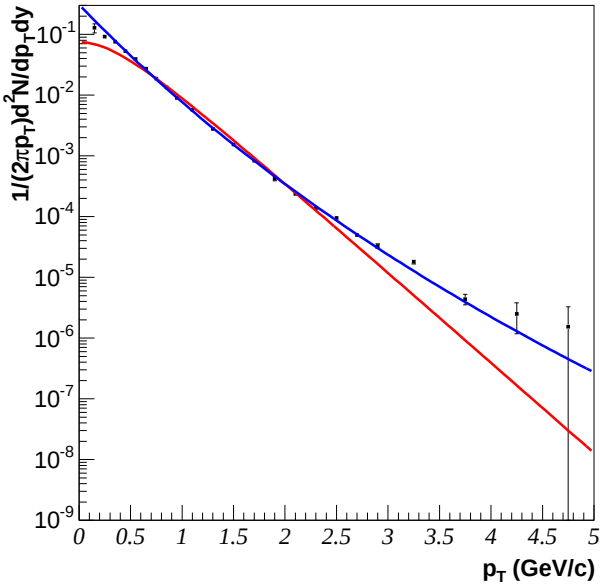

Figure 6.11: K^0_S spectrum as a function of p_T ($|y| < 0.5$). The m_T exponential fit (equation 6.3) is red and power law fit (equation 6.4) is blue.

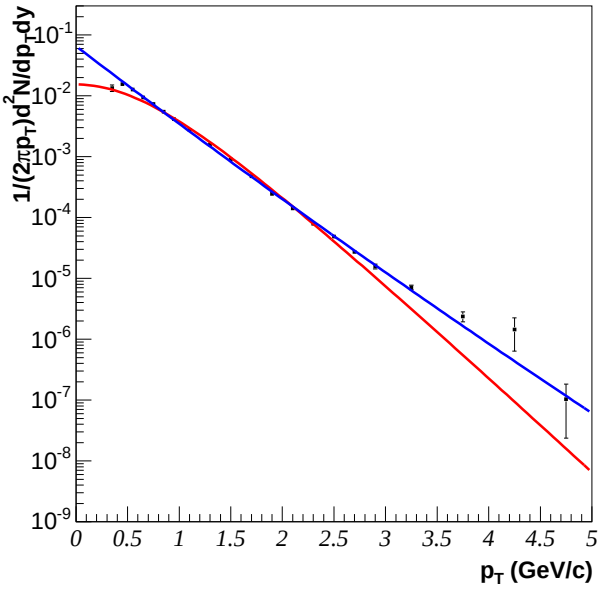

Figure 6.12: Λ spectrum as a function of p_T ($|y| < 0.5$). The m_T exponential fit (equation 6.3) is red and power law fit (equation 6.4) is blue.

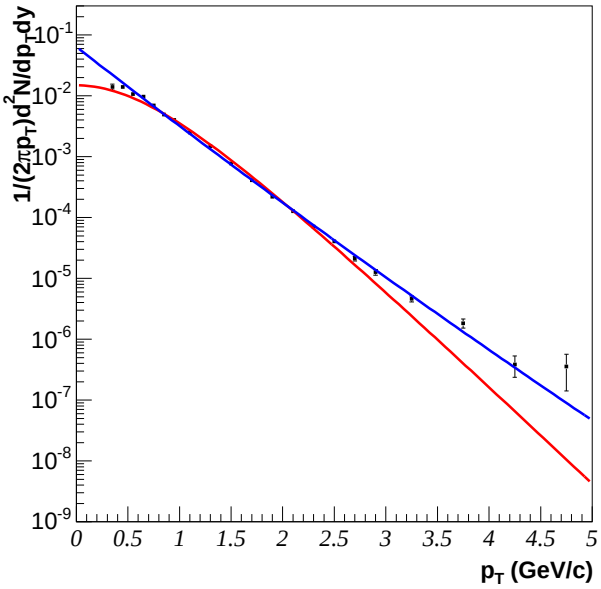

Figure 6.13: $\overline{\Lambda}$ spectrum as a function of p_T ($|y| < 0.5$). The m_T exponential fit (equation 6.3) is red and power law fit (equation 6.4) is blue.

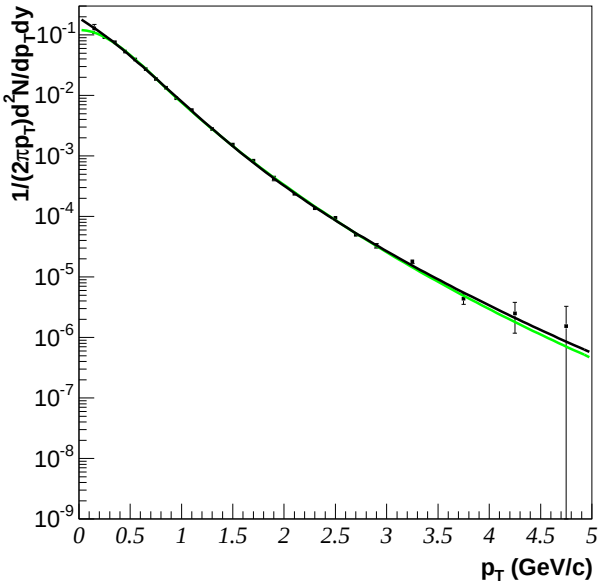

Figure 6.14: K^0_S spectrum as a function of p_T ($|y| < 0.5$). The composite form (equation 6.6) is black, and the 2 component fit (equation 6.8) is green.

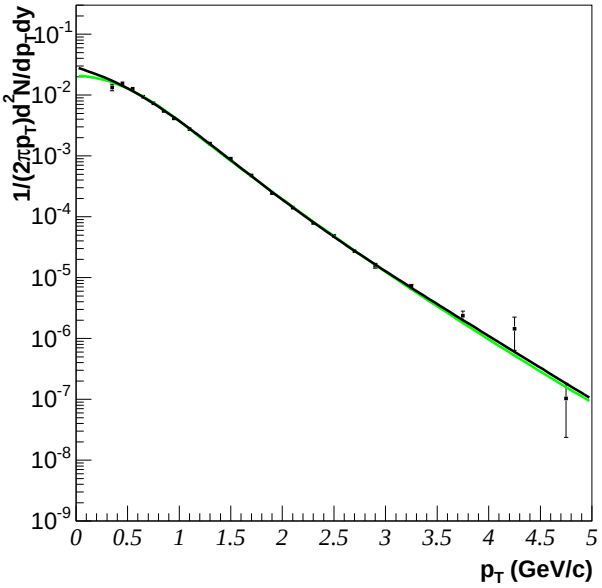

Figure 6.15: Λ spectrum as a function of p_T ($|y| < 0.5$). The composite form (equation 6.7) is black, and the 2 component fit (equation 6.8) is green.

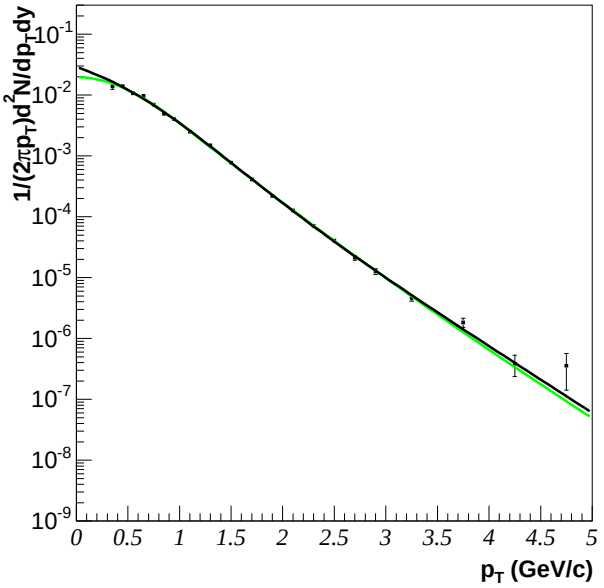

Figure 6.16: $\overline{\Lambda}$ spectrum as a function of p_T ($|y| < 0.5$). The composite form (equation 6.7) is black, and the 2 component fit (equation 6.8) is green.

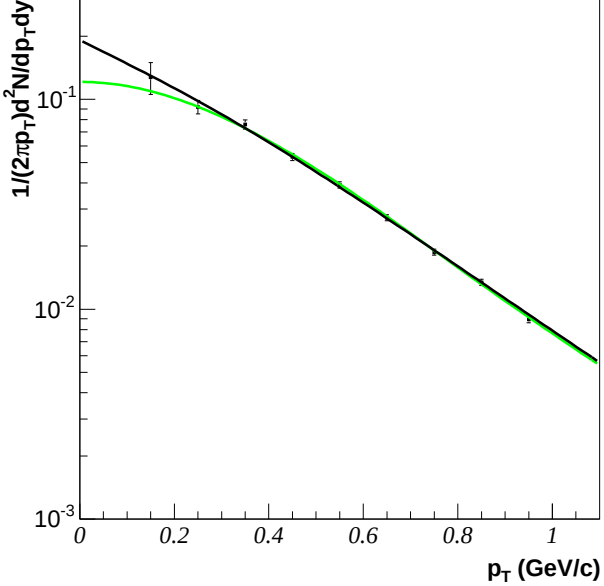

Figure 6.17: K^0_S spectrum as a function of p_T ($|y| < 0.5$). The composite form (equation 6.6) is black, and the 2 component fit (equation 6.8) is green. Fit extrapolation error over the range $0 < p_T < 0.1$ was determined from the difference between these functions.

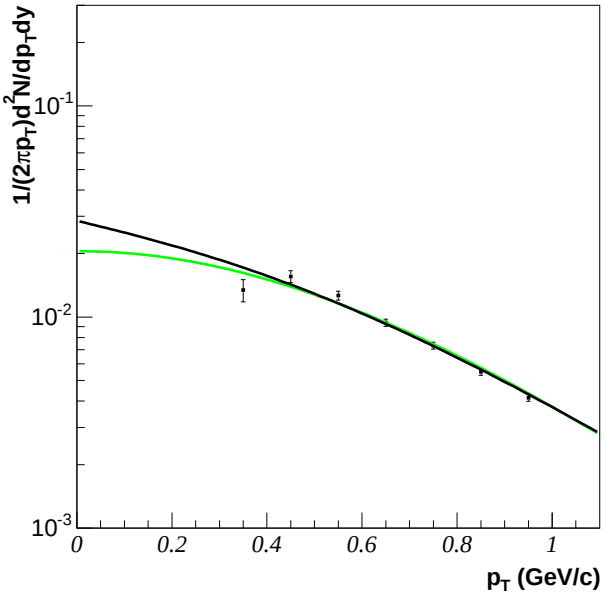

Figure 6.18: Λ spectrum as a function of p_T ($|y| < 0.5$). The composite form (equation 6.7) is black, and the 2 component fit (equation 6.8) is green. Fit extrapolation error over the range $0 < p_T < 0.3$ was determined from the difference between these functions.

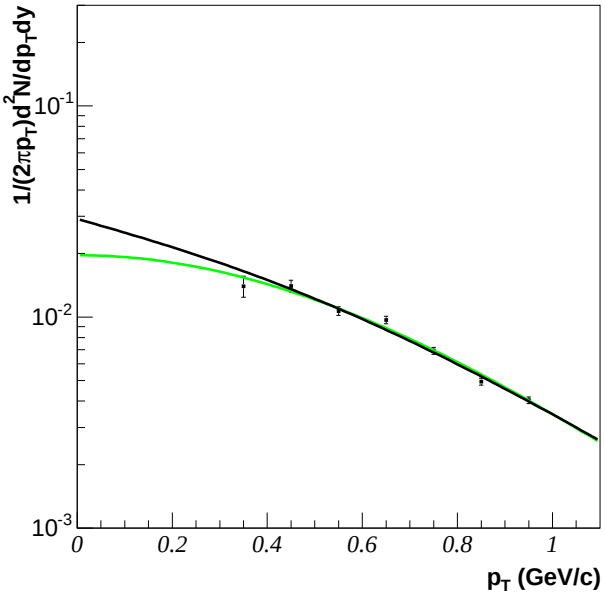

Figure 6.19: $\overline{\Lambda}$ spectrum as a function of p_T ($|y| < 0.5$). The composite form (equation 6.7) is black, and the 2 component fit (equation 6.8) is green. Fit extrapolation error over the range $0 < p_T < 0.3$ was determined from the difference between these functions.

The measured Λ and $\overline{\Lambda}$ spectra have contributions from primary Λs (directly produced) and secondary Λs from the decay of heavier hyperons. Some particles such as the Σ^0 undergo strong decays, making the Σ^0 decay vertex indistinguishable from the primary vertex. It is thus impossible to isolate the Σ^0 contribution to the total Λ yield using a topological analysis alone. Most quoted Λ yields therefore include the contribution of Σ baryons.

Another contribution comes from the decay of doubly strange Ξ^- and $\overline{\Xi^-}$ which undergo weak decays into Λ (and $\overline{\Lambda}$) as shown in equations 6.11 and 6.12. The Λs and $\overline{\Lambda}$s can be reconstructed using the v0 finding technique then paired with a charged pion, so as to create an Ξ candidate. The invariant mass of the Λ and π pair can be computed, and topological background reduction techniques similar to those described in section 5.1 be applied in order to extract the Ξ^- spectra.

$$\Xi^- \rightarrow \Lambda + \pi^-(b = 0.999,\, c\tau = 4.9\text{cm}) \tag{6.11}$$

$$\overline{\Xi^-} \rightarrow \overline{\Lambda} + \pi^+(b = 0.999,\, c\tau = 4.9\text{cm}) \tag{6.12}$$

The analysis of Ξ^- and $\overline{\Xi^-}$ was performed by another member of the STAR collaboration and is described elsewhere [80]. These measured mid-rapidity yields for Ξ^- and $\overline{\Xi^-}$ (shown in Table 6.7) are used as the basis for a Λ and $\overline{\Lambda}$ feed-down correction.

An additional source of feed-down comes from the Ξ^0 and $\overline{\Xi^0}$ decays,

$$\Xi^0 \rightarrow \Lambda + \pi^0(b = 0.995,\, c\tau = 8.7\text{cm}) \tag{6.13}$$

$$\overline{\Xi^0} \rightarrow \overline{\Lambda} + \pi^0(b = 0.995,\, c\tau = 8.7\text{cm}) \tag{6.14}$$

which are *not* measured. For the purposes of calculating the feed-down, the Ξ^- yield is assumed to be equal to the Ξ^0 yield and the $\overline{\Xi^-}$ yield equal to the $\overline{\Xi^0}$ yield.

Although virtually every Ξ or $\overline{\Xi}$ feeds down into a Λ or $\overline{\Lambda}$, one cannot simply subtract

Ξ^-	0.00181 ± 0.00008	0.97 ± 0.02
Ξ^+	0.00178 ± 0.00008	0.95 ± 0.02

Table 6.7: A summary of dN/dy and $\langle p_T \rangle$ for Ξ^- and Ξ^+ in p + p at $\sqrt{s} = 200$ GeV with $|y| < 0.5$ [80].

the Ξ yields in order to obtain the feed-down corrected Λ yields. This is because the efficiency of reconstructing secondary Λ and $\overline{\Lambda}$ may not be the same as the primary Λ and $\overline{\Lambda}$ efficiency. This is expected as the mean decay length of secondary Λ and $\overline{\Lambda}$ (from Ξ decay) is longer than for primary particles. Therefore a larger proportion of secondary Λ ($\overline{\Lambda}$) may be expected to pass the decay length cut. On the other hand more may fail the DCA to the primary vertex cut, as the secondary Λs do not originate from the primary vertex. The importance of feed-down corrections thus becomes apparent as the uncorrected spectra is a mixture of both primary and secondary Λs with only the primary Λ efficiency being used to correct the spectra.

As the efficiency correction varies as a function of p_T, the feed-down correction must also be applied as a function of p_T. Not only does the secondary Λ efficiency have to be found, but also the p_T spectra for the secondary Λ particles has to determined, as it is not equal to the Ξ p_T distribution.

The secondary Λ efficiency was investigated by embedding Monte Carlo generated Ξ^- into real events, as described in the embedding section. The comparison between the efficiency for primary Λ, compared to secondary Λ from Ξ^- decays, for the optimised set of cuts shown in Table 5.2 is shown in Figure 6.20. A quantity R_{eff} was defined which is the ratio of secondary and primary efficiencies such that,

$$R_{eff} = \frac{C(p_T)_{secondary}}{C(p_T)_{primary}} \tag{6.15}$$

where $C(p_T)_{secondary}$ and $C(p_T)_{primary}$ are the secondary and primary Λ finding efficiencies respectively.

This analysis utilised the same embedding generated for the separate Ξ^- analysis [80], in order to determine $C(p_T)_{secondary}$. However, no embedding was available in order

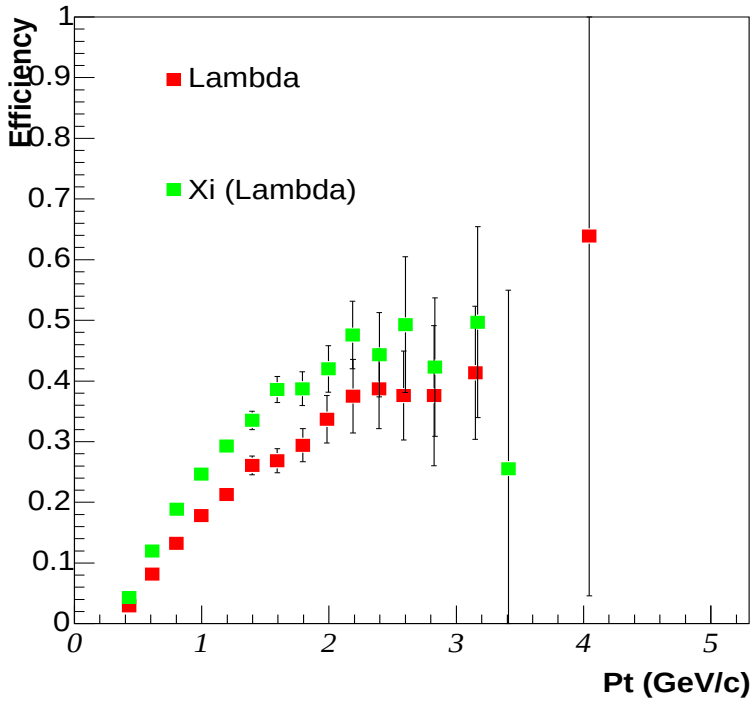

Figure 6.20: A comparison of primary and secondary Λ efficiency ($|y| < 0.5$), assuming that all secondary Λ come from Ξ^- decay.

to determine the efficiency for secondary Λ which originate from Ξ^0 decay. Instead the efficiency for secondary Λ from Ξ^0 decays was deduced by generating Monte Carlo Ξ^0 and Ξ^-, and propagating the decay particles through the STAR detector system using GEANT. After the geometric cuts had been applied, the ratio of Λ from Ξ^0 decay to those from Ξ^- decay (with $|y| < 0.5$) was found to be ~ 0.9, and flat as a function of p_T. This indicated that although the Ξ^0 and Ξ^- posses different decay lengths, they contribute equal numbers of secondary Λ to the final measured yield, assuming equal yields of Ξ^0 and Ξ^-. Therefore the secondary Λ finding efficiency was assumed to be the same for both the Ξ^- and Ξ^0 feed-down corrections.

As well as knowing the secondary Λ finding efficiency, a secondary Λ distribution as a function of p_T must be reproduced. It is impossible to get such a distribution from the real data, so the Ξ^- embedding was used as shown in Figure 6.21. In Figure 6.21 the p_T spectrum of the measured Ξ^- is shown, together with a Monte Carlo generated Ξ^- spectrum. The Monte Carlo Ξ^- spectrum is made to have approximately the same p_T distribution as the data and is re-normalised according to the measured Ξ^- yield. The secondary Λ

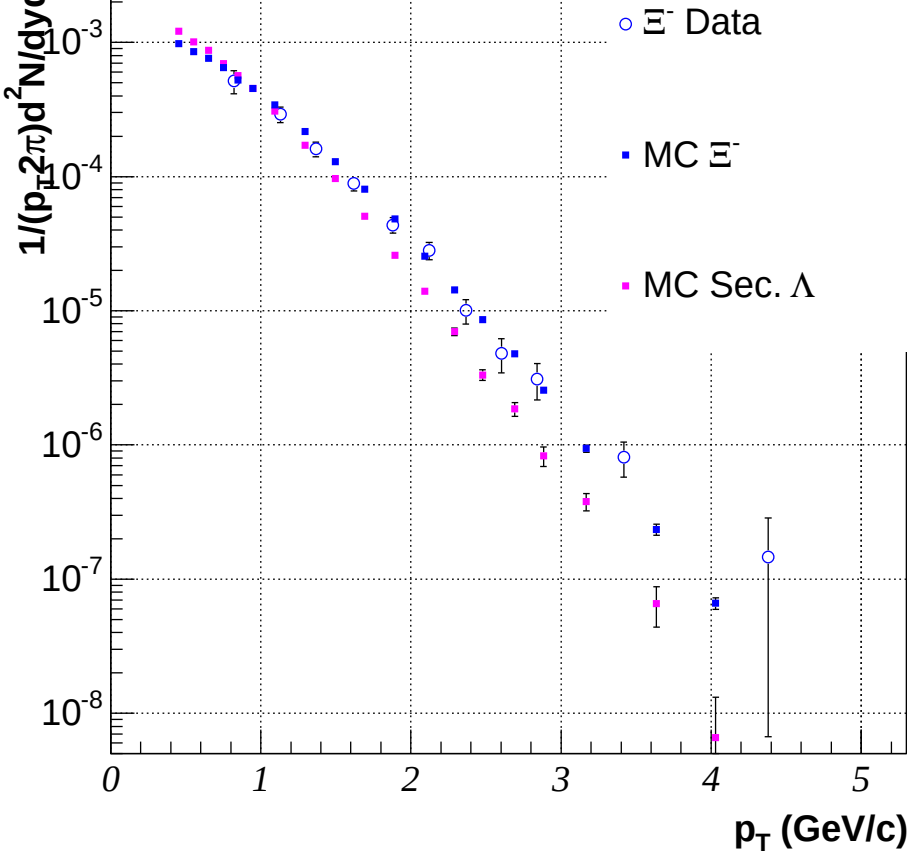

Figure 6.21: Comparison between the measured Ξ^- spectrum [80], and the Monte Carlo Simulated Ξ^- and secondary Λ spectra ($|y| < 0.5$).

distribution, $Simu(p_T)$ also shown in Figure 6.21 can be used to feed-down correct the measured Λ spectra. Ultimately a feed-down corrected spectrum, $Corrected(p_T)$, is made from the measured p_T spectrum (after efficiency corrections), $Measured(p_T)$ according to,

$$Corrected(p_T) = Measured(p_T) - Simu(p_T) \times R_{eff}(p_T) \tag{6.16}$$

As the same cuts were used for Λ and $\overline{\Lambda}$, the R_{eff} function as determined for Λ was also used for the $\overline{\Lambda}$ feed-down correction.

Feed-down corrections were applied on a p_T bin by p_T bin basis according to equation 6.16. Composite fits were applied to the Λ and $\overline{\Lambda}$ spectra, as shown in Figures 6.22 and 6.23 respectively. The feed-down corrected dN/dy and $\langle p_T \rangle$ as extracted from the composite fits are shown in Table 6.8.

Particle	dN/dy	$\langle p_T \rangle$ (GeV/c)
Λ	$0.0368 \pm 0.0008_{stat} \pm 0.0028_{syst}$	$0.759 \pm 0.024_{stat} \pm 0.021_{syst}$
$\overline{\Lambda}$	$0.0335 \pm 0.0008_{stat} \pm 0.0026_{syst}$	$0.747 \pm 0.023_{stat} \pm 0.023_{syst}$

Table 6.8: A summary of dN/dy and $\langle p_T \rangle$ for feed-down corrected Λ and $\overline{\Lambda}$ ($|y| < 0.5$).

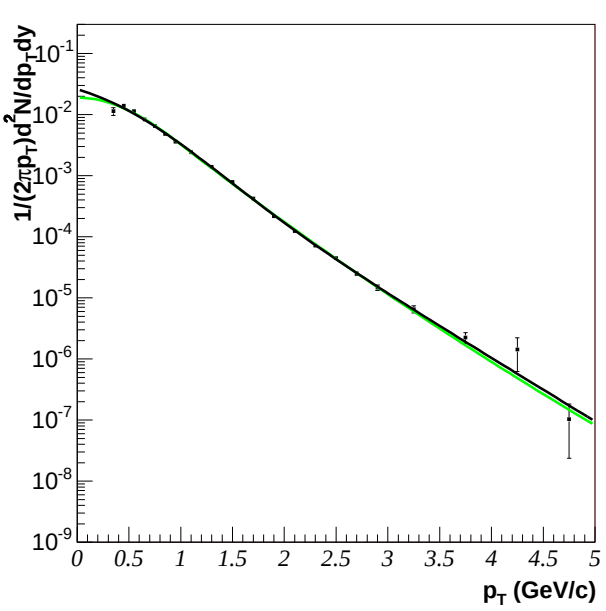

Figure 6.22: Λ spectrum as a function of p_T with correction for Ξ^0 and Ξ^- feed-down ($|y| < 0.5$).

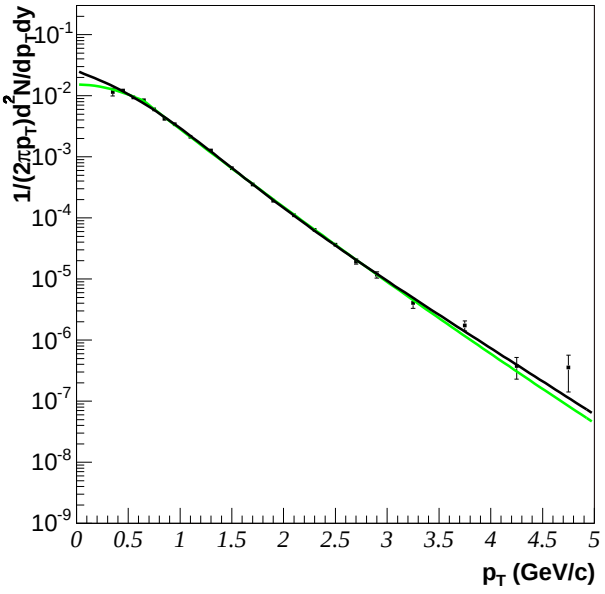

Figure 6.23: $\overline{\Lambda}$ spectrum as a function of p_T with correction for $\overline{\Xi^0}$ and $\overline{\Xi^-}$ feed-down ($|y| < 0.5$).

If the results in Table 6.8 are compared to the non-feed-down corrected yield and $\langle p_T \rangle$ for Λ and $\overline{\Lambda}$ shown in Table 6.6, it can be observed that applying the feed-down correction makes little difference to the $\langle p_T \rangle$. However, the Λ yield is shown to drop by $\sim$ 11 % with the $\overline{\Lambda}$ yield dropping by $\sim$ 14 %.

Chapter 7

Results

As was discussed in Chapter 6, the final yields and $\langle p_T \rangle$ for Λ, $\overline{\Lambda}$ and K^0_S are derived by using fits to extrapolate the spectra to $p_T = 0$. For convenience the feed-down corrected results are summarised in Table 7, below.

Particle	dN/dy	$\langle p_T \rangle$ (GeV/c)
Λ	$0.0368 \pm 0.0008_{stat} \pm 0.0028_{syst}$	$0.759 \pm 0.024_{stat} \pm 0.021_{syst}$
$\overline{\Lambda}$	$0.0335 \pm 0.0008_{stat} \pm 0.0026_{syst}$	$0.747 \pm 0.023_{stat} \pm 0.023_{syst}$
K^0_S	$0.129 \pm 0.003_{stat} \pm 0.007_{syst}$	$0.612 \pm 0.020_{stat} \pm 0.015_{syst}$

Table 7.1: A summary of dN/dy and $\langle p_T \rangle$ for feed-down corrected Λ and $\overline{\Lambda}$ and also K^0_S ($|y| < 0.5$).

The fitting techniques described in section 6.6 can be utilised so as measure Λ, $\overline{\Lambda}$ and K^0_S yield and $\langle p_T \rangle$ over different rapidity intervals or for events of different multiplicity. As shown in the next section, this is useful when making comparisons to other experiments. Results are also compared to pQCD model predictions. In the final section the Λ and $\overline{\Lambda}$ yields determined by this analysis, and also the yields of Ξ^- and $\overline{\Xi^-}$ (see [80]) are compared to corresponding yields from Au + Au collisions at $\sqrt{s} = 200$ GeV, in order to determine if yields of Λ and Ξ are enhanced in heavy ion collisions.

The UA5 experiment measured mid-rapidity yields for $\Lambda + \overline{\Lambda}$ and K^0_S from $\mathrm{p} + \overline{\mathrm{p}}$ collisions also at $\sqrt{s} = 200$ GeV [28]. It is expected that the yield from $\mathrm{p} + \overline{\mathrm{p}}$ experiments will be quite similar to $\mathrm{p} + \mathrm{p}$ experiments at $\sqrt{s} = 200$ GeV, thus the UA5 result will form a useful comparison. Unfortunately, the UA5 experiment measured strange yields over a much wider rapidity range ($|\mathrm{y}| < 2$) than the rapidity range ($|\mathrm{y}| < 0.5$) over which yields are quoted in this thesis. The rapidity distribution is known to be roughly flat at mid-rapidity [82], so an initial comparison with UA5 results may involve multiplying the measured yield by 4.

The results of Dawson et al. [42] show that it is possible to tune the PYTHIA event generator [40] in order to achieve agreement with charged particle spectra from high energy $\mathrm{p} + \overline{\mathrm{p}}$ collisions. PYTHIA simulations of $\mathrm{p} + \mathrm{p}$ and $\mathrm{p} + \overline{\mathrm{p}}$ collisions at $\sqrt{s} = 200$ GeV were made in order to determine appropriate scaling factors by making comparisons between the rapidity distributions of Λ, $\overline{\Lambda}$ and K^0_S.

In order to test the shape of the rapidity distributions from PYTHIA the distributions generated for $\mathrm{p} + \mathrm{p}$ collisions were compared to STAR yields, measured over the available STAR detector acceptance ($|\mathrm{y}| < 1$). In order to determine a rapidity extrapolation factor it is only necessary to use the shape of the rapidity distribution. Thus the mid-rapidity PYTHIA points are made to agree with the measured yields (Table 7), by normalising the PYTHIA distribution to the data at y=0. As expected, no significant variation was observed in the Λ, $\overline{\Lambda}$ and K^0_S yield over the limited range of ($|\mathrm{y}| < 1$), thus agreeing with the PYTHIA rapidity distributions shown for K^0_S, Λ and $\overline{\Lambda}$ in Figures 7.1, 7.2 and 7.3 respectively.

Although the Λ, $\overline{\Lambda}$ and K^0_S yields from $\mathrm{p} + \mathrm{p}$ and $\mathrm{p} + \overline{\mathrm{p}}$ collisions are expected to be approximately equal at $\sqrt{s} = 200$ GeV, it is interesting to test this assumption, using PYTHIA. The PYTHIA generated $\mathrm{p} + \overline{\mathrm{p}}$ rapidity distributions for K^0_S, Λ and $\overline{\Lambda}$ are shown in Figures 7.4, 7.5 and 7.6. Here the PYTHIA $\mathrm{p} + \overline{\mathrm{p}}$ distributions are multiplied by the same normalising factor used for the PYTHIA $\mathrm{p} + \mathrm{p}$ distributions. As the measured yields also agree with the $\mathrm{p} + \overline{\mathrm{p}}$ rapidity distributions over ($|\mathrm{y}| < 1$), PYTHIA also indicates that

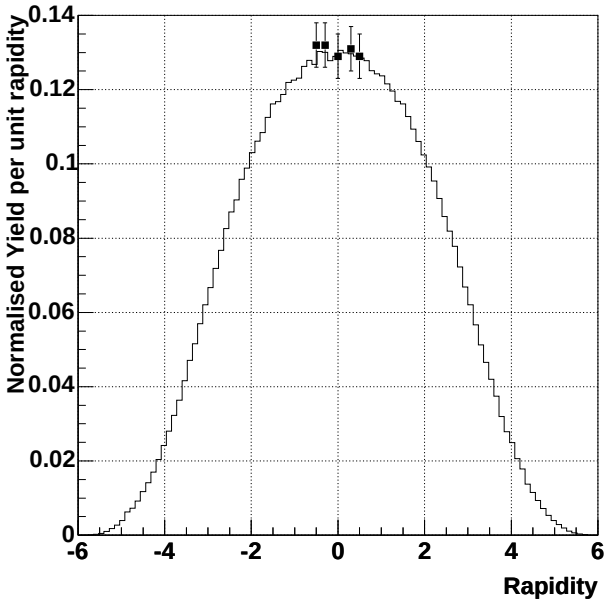

Figure 7.1: Measured K^0_S yield, and normalised PYTHIA rapidity distribution for p + p at $\sqrt{s} = 200$ GeV.

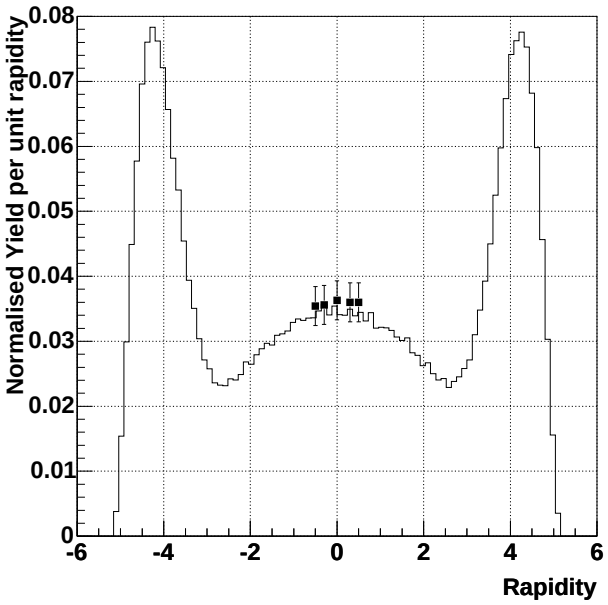

Figure 7.2: Measured Λ yield, and normalised PYTHIA rapidity distribution for p + p at $\sqrt{s} = 200$ GeV.

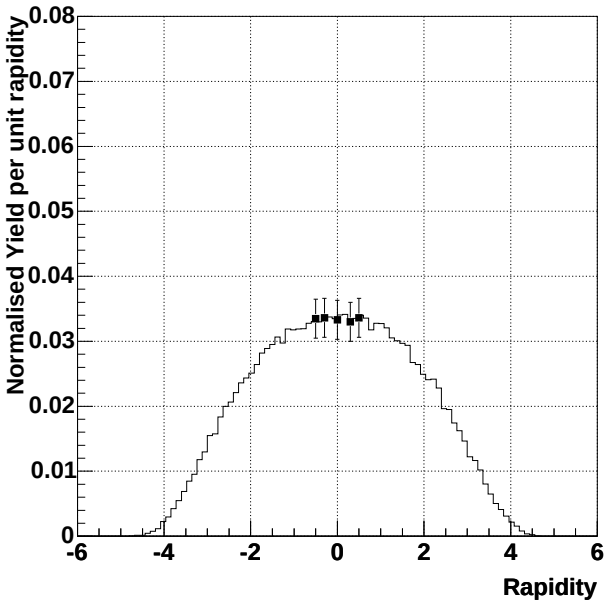

Figure 7.3: Measured $\overline{\Lambda}$ yield, and normalised PYTHIA rapidity distribution for p + p at $\sqrt{s} = 200$ GeV.

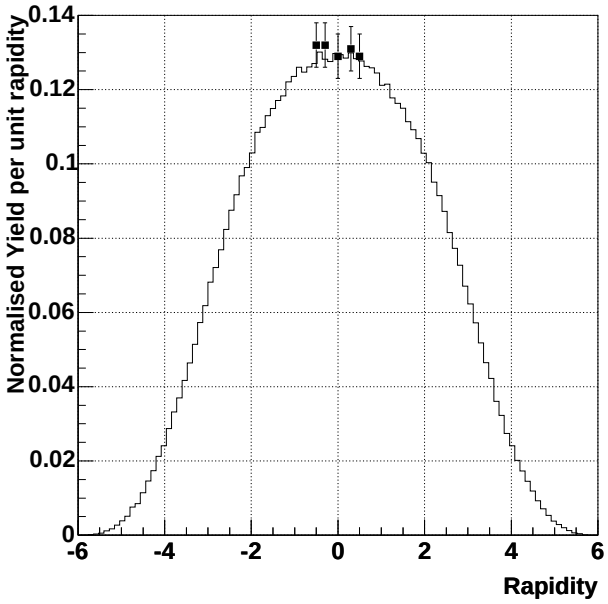

Figure 7.4: Measured K^0_S yield ($\mathrm{p}+\mathrm{p}$), and normalised PYTHIA rapidity distribution for $\mathrm{p}+\overline{\mathrm{p}}$ at $\sqrt{s} = 200$ GeV.

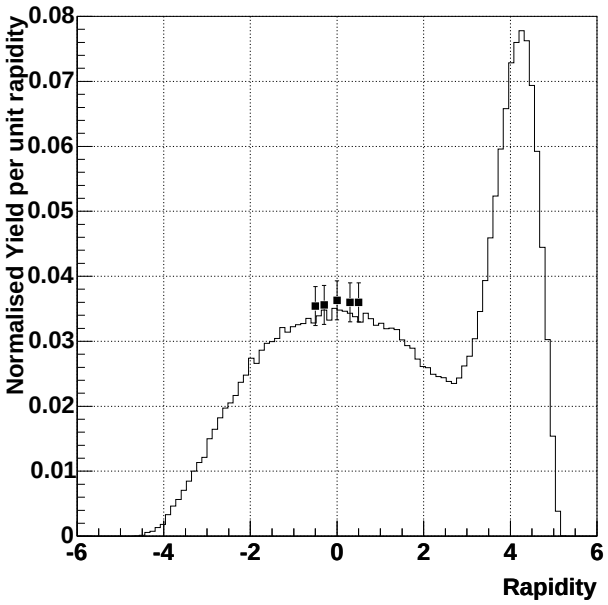

Figure 7.5: Measured Λ yield ($\mathrm{p}+\mathrm{p}$), and normalised PYTHIA rapidity distribution for $\mathrm{p}+\overline{\mathrm{p}}$ at $\sqrt{s} = 200$ GeV.

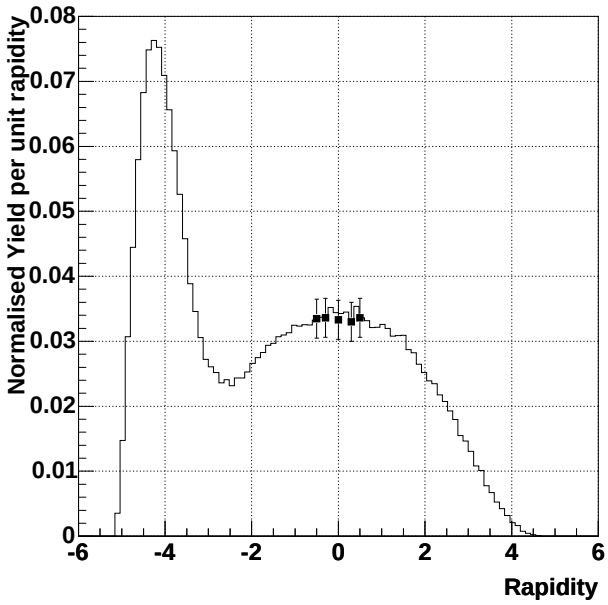

Figure 7.6: Measured $\overline{\Lambda}$ yield ($\mathrm{p}+\mathrm{p}$), and normalised PYTHIA rapidity distribution for $\mathrm{p}+\overline{\mathrm{p}}$ at $\sqrt{s} = 200$ GeV.

distributions shown in Figures 7.1, 7.2 and 7.3 were used to generate scaling factors, by simply dividing the PYTHIA yield for particles with rapidity $|y| < 2$ by the PYTHIA $|y| < 0.5$ yield. A factor of ~ 3.6 was determined for $(\Lambda + \overline{\Lambda})$ and also K^0_S; sufficiently different from 4 to justify the PYTHIA simulation. The UA5 yield and the scaled STAR yields are shown in Table 7.2. As anticipated, good agreement was achieved between the STAR exrapolated dN/dy and the UA5 measured dN/dy.

Particle	STAR dN/dy $\|y\| < 0.5$	UA5 dN/dy $\|y\| < 2.0$	STAR dN/dy $\|y\| < 2.0$
$\Lambda + \overline{\Lambda}$	$0.0703 \pm 0.0011_{stat} \pm 0.0038_{syst}$	0.27 ± 0.07	$0.252 \pm 0.0039_{stat} \pm 0.0136_{syst}$
K^0_S	$0.129 \pm 0.003_{stat} \pm 0.007_{syst}$	0.44 +/- 0.09	$0.466 \pm 0.011_{stat} \pm 0.025_{syst}$

Table 7.2: A summary of dN/dy for $\Lambda + \overline{\Lambda}$ and K^0_S (Λ, $\overline{\Lambda}$ feed-down corrected) measured by the UA5 [28] and STAR experiments.

As was discussed in section 2.1.2, an increase of Λ, $\overline{\Lambda}$ and K^0_S $\langle p_T \rangle$ with multiplicity was observed by UA1 at $\sqrt{s} = 630$ GeV, and for K^0_S by E735 at $\sqrt{s} = 1.8$ TeV [32],[33]. As the spectra had to be divided into multiplicity bins in order to apply the vertex correction, it is convenient to extract the yield and $\langle p_T \rangle$ from the multiplicity divided spectra. Six multiplicity bins were created, where multiplicity is defined as all primary tracks which have $|\eta| < 1$.

Mult. class	No. primary tracks ($a \to b$)	$\frac{Yield_{\Lambda(a\to b)}}{N_{events(a\to b)}}$	$\frac{Yield_{\overline{\Lambda}(a\to b)}}{N_{events(a\to b)}}$	$\frac{Yield_{K^0_S(a\to b)}}{N_{events(a\to b)}}$	$N_{events(a\to b)}$
1	$0 \to 2$	0.0083 ± 0.0011	0.0072 ± 0.0009	0.0322 ± 0.0043	4.12×10^6
2	$3 \to 4$	0.0299 ± 0.0031	0.0268 ± 0.0028	0.1009 ± 0.0106	2.86×10^6
3	$5 \to 6$	0.0479 ± 0.0048	0.0440 ± 0.0045	0.1544 ± 0.0158	1.96×10^6
4	$7 \to 8$	0.0695 ± 0.0072	0.0629 ± 0.0065	0.2160 ± 0.0228	1.19×10^6
5	$9 \to 12$	0.1030 ± 0.0010	0.0987 ± 0.0096	0.2960 ± 0.0289	1.13×10^6
6	> 13	0.1798 ± 0.0186	0.1775 ± 0.0184	0.5019 ± 0.0529	4.63×10^5
SUM		0.0423	0.0393	0.132	11.7×10^6
Mean Tracks	4.90	7.96	8.12	7.60	

Table 7.3: A table showing yields of Λ, $\overline{\Lambda}$ and K^0_S ($|y|$ <0.5), in each of the six multiplicity classes which are defined as all those events which have primary track multiplicity ($|\eta| < 1$) from a to b inclusive.

Λ or $\overline{\Lambda}$ being ~ 22 times more abundant in high multiplicity collisions (> 13 tracks), compared to low multiplicity collisions ($0 \rightarrow 2$ tracks). The lighter K^0_S is only 15 times more abundant in high multiplicity collisions, compared to collisions of the lowest multiplicity class, suggesting that Λ and $\overline{\Lambda}$ production in the lowest multiplicity class is suppressed due to their larger mass. Interestingly the ratio of $\overline{\Lambda}$ to Λ increases from 0.86 in the lowest multiplicity class ($0 \rightarrow 2$), to 0.99 in the > 13 class, suggesting that the relative proportions of $q\overline{q}$ pairs compared to original valence quarks (at y=0) grow with multiplicity. This may be caused by harder collisions at the partonic level, which in turn might create more energetic (or 'longer') strings, which then fragment into more $q\overline{q}$ pairs.

The behaviour of Λ, $\overline{\Lambda}$ and K^0_S $\langle p_T \rangle$ as a function of multiplicity is shown in Figure 7.7. As for the UA1 results (Figure 2.5) the same trend of increasing $\langle p_T \rangle$ as a function of multiplicity is observed. However, where as the UA1 (and for the K^0_S, E735) results indicate a linear relationship between $\langle p_T \rangle$and multiplicity, in Figure 7.7 there is, perhaps, the hint of a 'step' in the relationship between $\langle p_T \rangle$and multiplicity for Λ and $\overline{\Lambda}$, at around 7 primary tracks. Also the $\langle p_T \rangle$ increase for the Λ and $\overline{\Lambda}$ does not appear to be as steep as the trend observed by UA1.

The overall value of $\langle p_T \rangle$ obtained for the K^0_S by UA1 ($\mathrm{p} + \overline{\mathrm{p}}$ at $\sqrt{s} = 630$ GeV) is less than measured by this analysis. Table 7.4 shows a comparison with the ($\Lambda + \overline{\Lambda}$) and K^0_S $\langle p_T \rangle$ as measured by the UA5 collaboration, and the K^0_S $\langle p_T \rangle$ is again shown to be less than the measured value. A possible explanation may be in the fact that both UA1 and UA5 fit power laws (equation 2.3) to their K^0_S spectra, which has (as shown in Table 6.4) the effect of reducing $\langle p_T \rangle$.

Particle	STAR $\langle p_T \rangle$ (GeV/c) $\lvert y \rvert < 0.5$	UA5 $\langle p_T \rangle$ (GeV/c) $\lvert y \rvert < 2.0$
$\Lambda + \overline{\Lambda}$	$0.753 \pm 0.033_{stat} \pm 0.068_{syst}$	$0.8^{+0.2}_{-0.14}$
K^0_S	$0.612 \pm 0.020_{stat} \pm 0.015_{syst}$	$0.53^{+0.08}_{-0.06}$

Table 7.4: A summary of $\langle p_T \rangle$ for $\Lambda + \overline{\Lambda}$ (feed-down corrected) and K^0_S measured by the UA5 [28] and STAR experiments.

It is revealing to briefly compare the behaviour of $\langle p_T \rangle$ and $\frac{\overline{\Lambda}}{\Lambda}$ with the trends observed

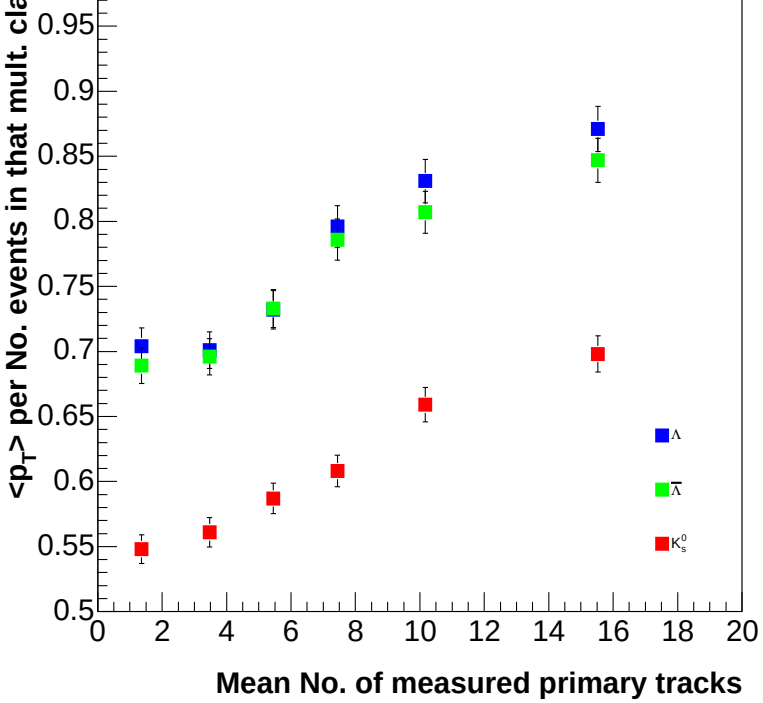

Figure 7.7: Plot of $\langle p_T \rangle$ vs measured primary track multiplicity ($|\eta| < 1$) for Λ, $\overline{\Lambda}$ and K^0_S ($|y| < 0.5$).

in high energy Au + Au collisions. For relativistic heavy ion collisions, multiplicity is used as a measure of collision centrality (see Appendix A), and for Au + Au collisions at $\sqrt{s} =$ 130 GeV both $\frac{\overline{\Lambda}}{\Lambda}$ and the Hagedorn temperature parameter, T ($\langle p_T \rangle$), were observed to be approximately constant with multiplicity [78]. Given that a single p + p collision may consist of multiple parton+parton interactions [43], it is not unreasonable to consider that multiplicity may have also been related to the 'centrality' of a p + p collision. However, the observations of increasing $\langle p_T \rangle$ and $\frac{\overline{\Lambda}}{\Lambda}$ with multiplicity in p + p collisions strongly suggest that the increase in multiplicity is caused by harder interactions between the constituent partons, unlike for high energy heavy ion collisions.

7.2 Comparisons with Models

As discussed in Chapter 2, comparison with various model predictions remains a good reason for studying the p + p data in its own right. Calculations based on next to leading order pQCD have been made for the K^0_S spectra by Albino, Kniehl and Kramer (AKK)

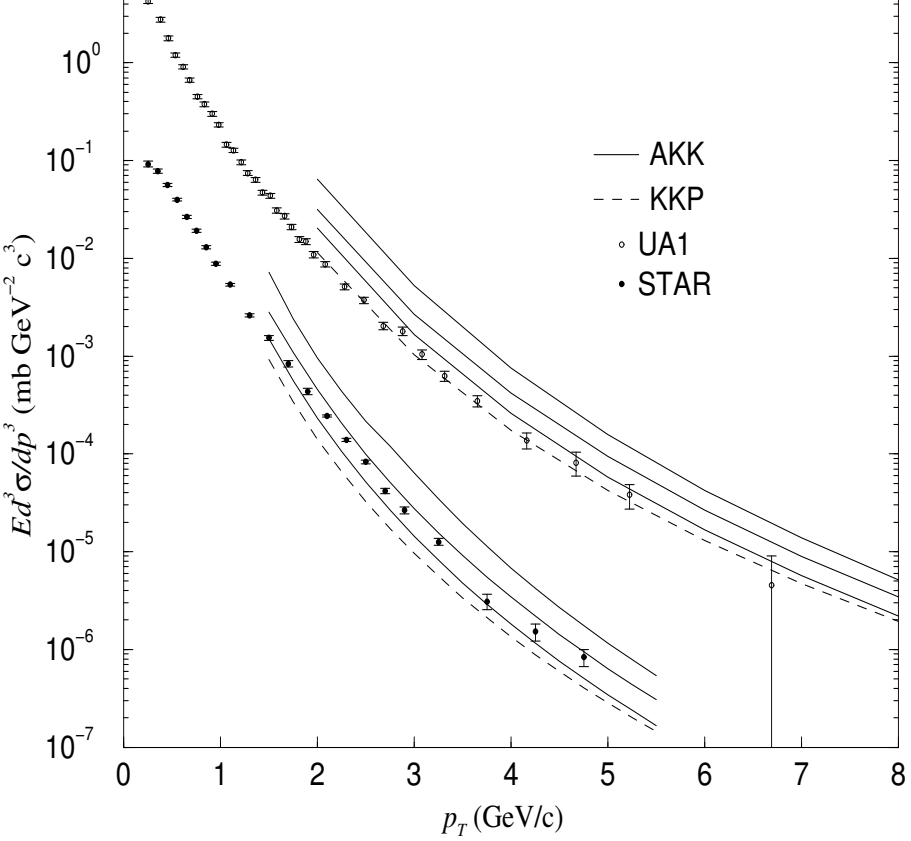

Figure 7.8: A comparison of the K^0_S spectra with next to leading order pQCD calculations [83],[84]. For clarity the STAR K^0_S, determined by this analysis have been divided by 30. For the AKK prediction, the three solid lines represent three different parameterisations of the pQCD calculation.

[83], and also Kniehl, Kramer and Pötter (KKP) [84]. Figure 7.8 compares the pQCD calculations with the measured K^0_S spectra. Even at high p_T there are discrepancies between the calculations and the data, with the KKP results in particular favouring the UA1 data. However, the K^0_S from this analysis appear to achieve better agreement with the more recent AKK calculation compared to the KKP prediction.

Dumitru has also studied p + p collisions within the context of the PYTHIA model [52]. Dumitru states that at RHIC energies, the colour flux tubes may no longer be orientated longitudinally (as in non-pQCD processes), but instead acquire significant transverse momentum, due to perturbative interactions. Although hadrons are still being produced via a fragmentation mechanism, the fragmenting strings can be rotated with respect to the lab frame, and can be regarded as 'mini jets'. Therefore this picture is consistent

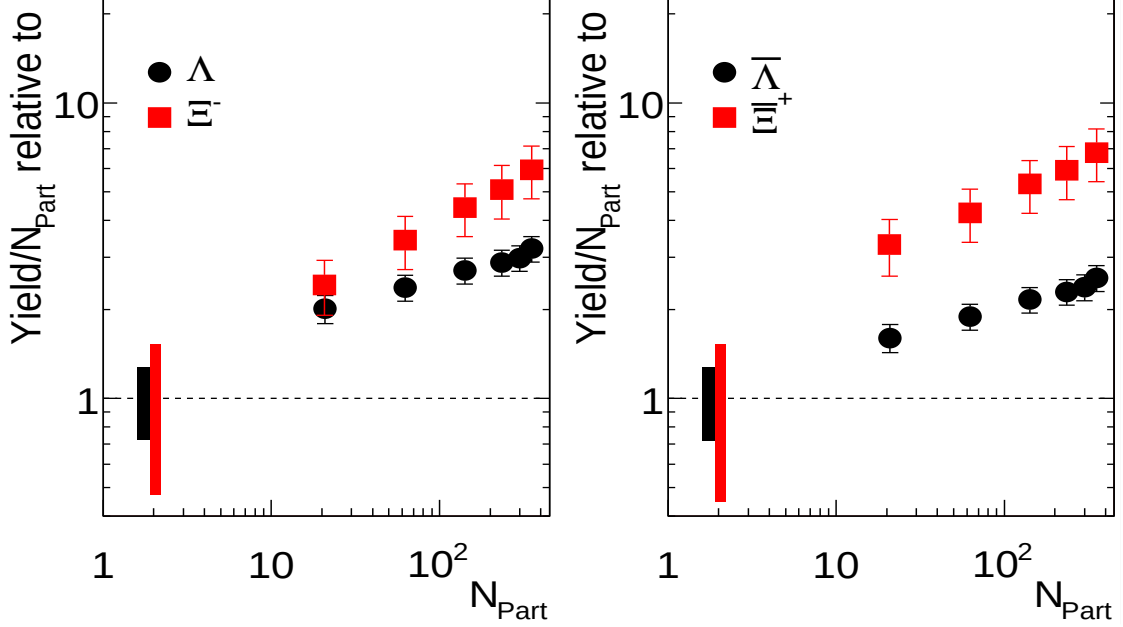

Figure 7.9: Strangeness enhancement factors at $\sqrt{s} = 200$ GeV according to equation 7.1, plotted as a function of the number of participating nucleons (N_{part}).

with the model of Wang and Hwa [48], and explains the increase of $\langle p_T \rangle$ with multiplicity observed elsewhere [33], [32], and also by this analysis as shown in Figure 7.7.

7.3 Strangeness Enhancement

The Λ, $\overline{\Lambda}$, Ξ^- and $\overline{\Xi^-}$ yields in Au + Au collisions at $\sqrt{s} = 200$ GeV measured by the STAR experiment [86] are compared with the p + p yields to derive strangeness enhancement factors, by using equation 7.1,

$$Enhancement = \frac{\left(\frac{Yield}{N_{part}}\right)_{Au+Au}}{\left(\frac{Yield}{N_{part}}\right)_{p+p}} \tag{7.1}$$

where N_{part} is the number of participating nucleons in the Au + Au collisions. Details of the calculation of N_{part} are described in Appendix A. The resulting strangeness enhancement factors are displayed below in Figure 7.9.

An enhancement is observed for all centralities, with the doubly strange Ξ^-s being enhanced more than the Λs, in accordance with Rafelski's original prediction. However,

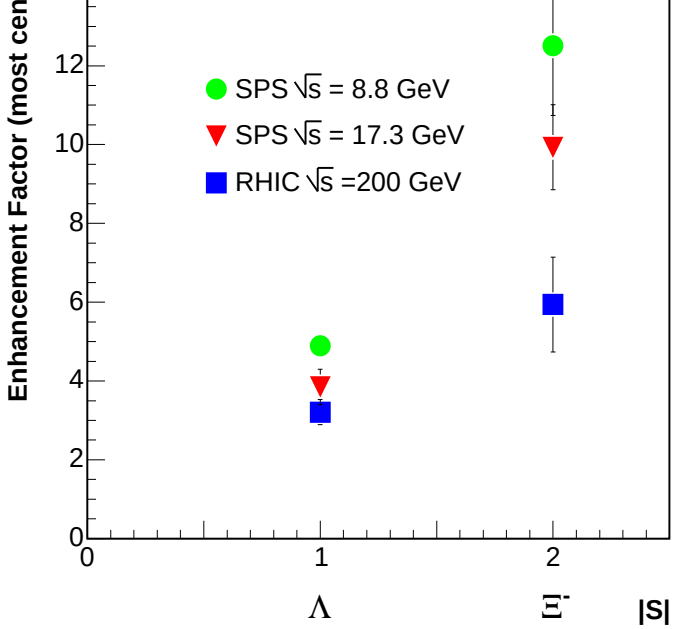

Figure 7.10: Strangeness Enhancement factors as a function of $\sqrt{s}$ for Λ and Ξ^- in only the most central bins.

when these enhancement factors are compared to the enhancement measured at the CERN SPS at $\sqrt{s} = 17.3$ GeV, and a more recent CERN SPS $\sqrt{s} = 8.8$ GeV measurement [87], it is found that enhancement at RHIC energies is actually *less* than at the lower SPS energies. This is shown for the most central Λ and Ξ^- yields in Figure 7.10. One possible explanation for the decrease in the enhancement factors as $\sqrt{s}$ increases has been put forward by Tounsi, Mishke and Redlich [89]. It is argued that strangeness enhancement may be explained by the different ways in which thermal model calculations have to be approached if they are to successfully describe the experimentally measured yields and ratios of particles. For small systems, such as p + p or p + Be, the canonical ensemble must be used; this means that all quantum numbers have to be conserved locally. The result is that there not only has to be sufficient energy to create strangeness in small systems, but also sufficient phase space. The volume of the system created by collisions at constant $\sqrt{s}$ is believed to be directly proportional to the number of participants, N_{part}.

Figure 7.11 shows the expected enhancement factors for Ωs, Ξs, and Λs as a function of N_{part} calculated using statistical models for collision energies of $\sqrt{s} = 8.8$ GeV. Crucially it has been shown that increasing the collision energy, also increases the available phase space

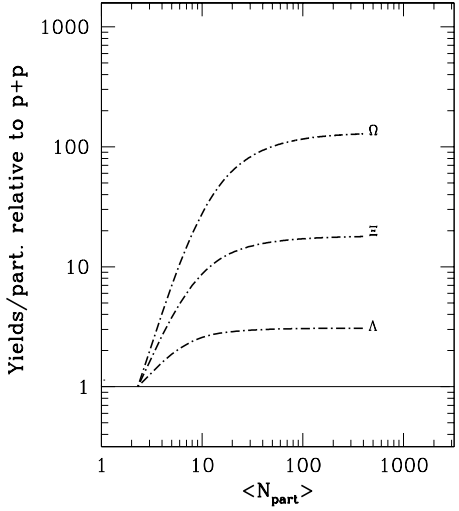

Figure 7.11: Centrality dependence of the relative enhancement of particle yields per participant in central $\mathrm{Pb}+\mathrm{Pb}$ to $\mathrm{p}+\mathrm{p}$ collisions at $\sqrt{s} = 8.73$ GeV [89].

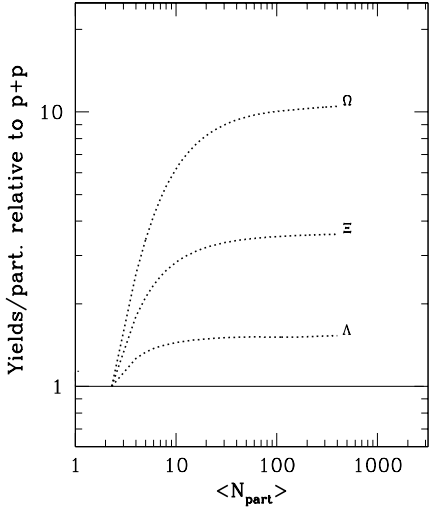

Figure 7.12: Centrality dependence of the relative enhancement of particle yields/participant in central $\mathrm{Pb}+\mathrm{Pb}$ to $\mathrm{p}+\mathrm{p}$ collisions at $\sqrt{s} = 130$ GeV [89].

for particle production in small systems such as $\mathrm{p}+\mathrm{p}$ or $\mathrm{p}+\mathrm{Be}$. Thus the enhancement factors are predicted to decrease with increasing $\sqrt{s}$, as the baseline measured ($\mathrm{p}+\mathrm{p}$ or $\mathrm{p}+\mathrm{Be}$) becomes less 'canonically' suppressed with respect to the larger $\mathrm{Au}+\mathrm{Au}$ or $\mathrm{Pb}+\mathrm{Pb}$ system. This is indicated by the comparison of Figure 7.11 with Figure 7.12 which shows the expected enhancement factors for Ωs, Ξs and Λs as a function of N_{part} calculated using statistical models for collision energies of $\sqrt{s} = 130$ GeV; enhancement at $\sqrt{s} = 8.73$ GeV (Figure 7.11) is shown to be greater than at $\sqrt{s} = 130$ GeV (Figure 7.12). No calculation was available for the 200 GeV data.

In both Figures 7.11 and 7.12 the expected enhancement rapidly increases with the volume (N_{part}), and for the Ξ and Λ saturates as $N_{part} > 30$. Conversley, as shown in Figure 7.9, the trend for the experimentally measured enhancement factors is for a smooth increase in enhancement with N_{part}, and is not reproduced in the statistical model by Tounsi, Mishke and Redlich (Figure 7.12). One possible explanation for this could be that models show that the strangeness saturation factor, γ_s is ~ 1 for only the most central $\mathrm{Au}+\mathrm{Au}$ data, but is less than 1 for all other centralities. The model by Tounsi, Mishke and Redlich assumes full strangeness equilibration for all centralities [89].

Another possible explanation could be in the calculation of the scaling factor, N_{part}.

collisions, thus further increasing the strangeness yield with increasing number of participants. A combination of N_{binary} (see Appendix A) and N_{part} scaling may be better [86].

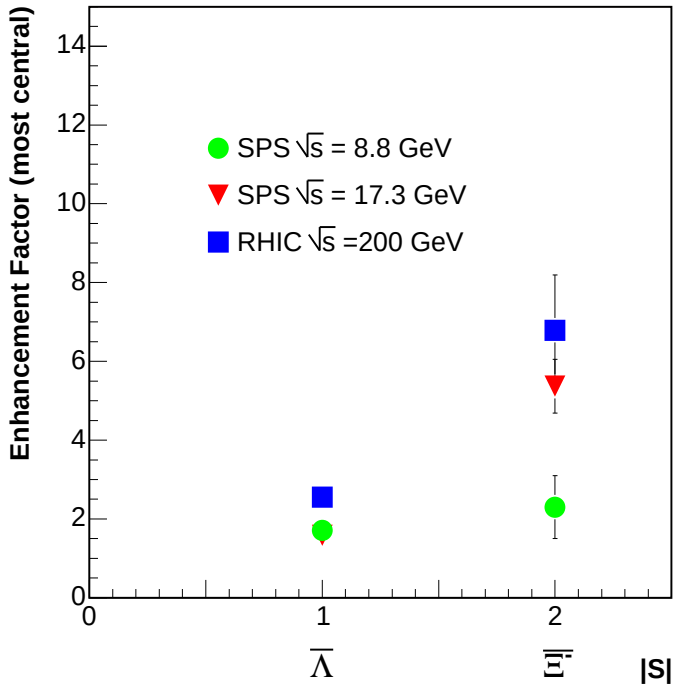

Figure 7.13: Strangeness enhancement factors as a function of $\sqrt{s}$ for $\overline{\Lambda}$ and $\overline{\Xi^-}$ in only the most central bins.

As was shown in Figure 1.7 (in Chapter 1) the anti-baryon to baryon ratio increases as a function of $\sqrt{s}$. This may be interpreted as a decrease in the baryo-chemical potential as $\sqrt{s}$ increases, as the system gets closer to becoming net baryon free. Thus, when considering the enhancement for different $\sqrt{s}$ of anti-strange particles, such as the $\overline{\Lambda}$ and $\overline{\Xi^-}$ the additional effect of the changing baryo-chemical potential plays an important role, as anti-baryons become enhanced with respect to baryons as $\sqrt{s}$ increases. Thus while Λ and Ξ^- become suppressed with increasing $\sqrt{s}$ (Figure 7.10), the $\overline{\Lambda}$ and $\overline{\Xi^-}$ are enhanced as shown in Figure 7.13.

Chapter 8

Conclusions and Outlook

The analysis of Λ, $\overline{\Lambda}$, and K^0_S from p + p collisions at $\sqrt{s} = 200$ GeV have been discussed and the particle spectra as a function of p_T have been presented. The spectra can be used to better constrain microscopic QCD and phenomenological models and macroscopic thermal models, and hence improve the understanding of particle production in high energy physics. Clues to how theorists can go on and use this data are given by the fact that two component fits best describe the data, and also by the increase in $\langle p_T \rangle$ and yield with multiplicity, which may be due to a growing mini-jet contribution.

A pQCD inspired power law fit is needed to describe the high p_T part of the Λ, $\overline{\Lambda}$ and K^0_S spectra, where as a Hagedorn m_T exponential is needed at low p_T. It is interesting to note that for Au + Au collisions at $\sqrt{s} = 200$ GeV the Hagedorn m_T exponential gives a good fit to the spectra over the full range of measured p_T for $(\Lambda + \overline{\Lambda})$ [88]. This may suggest that collective effects (which result in thermalisation and bulk flow) play a greater role in Au + Au collisions. Intriguingly, for the K^0_S spectrum a power law like tail is observed for $p_T > 4$ GeV in Au + Au collisions; the fact that the pQCD-like part of the K^0_S spectrum is shifted to higher p_T in Au + Au may indicate that a two component fit should work best for neutral strange particle production in heavy ion collisions, should sufficient statistics become available to extend the high p_T reach of the spectra.

Strangeness enhancement has long been used as a signature for a Quark-Gluon Plasma phase of matter. However, when the STAR enhancement result is compared with those results from SPS, enhancements of Λ and Ξ^- are observed to decrease with energy for the

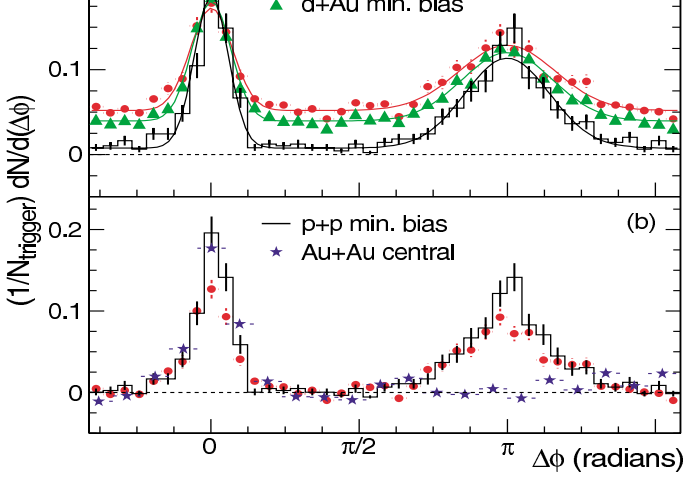

Figure 8.1: Hadronic jet correlation studies from from collisions of Au + Au, d + Au and p + p collisions at $\sqrt{s} = 200$ GeV. Figure (a) compares correlations from d + Au collisions with p + p collisions, where no QGP is expected, and no suppression is observed. Suppression of the away side jet is observed only for Au + Au collisions (b), suggesting the formation of a deconfined state of matter [90].

most central data. It is argued that this is due to the baseline comparison measurement (p + p collisions at RHIC and p + Be at the SPS) becoming less canonically suppressed as the collision energy increases [89]. Although such models claim to be able to predict the level of canonical strangeness enhancement, any such 'correction' would be strongly model dependent. Although strangeness enhancement may still be a characteristic of QGP formation, the wealth of new data to come from the experiments at RHIC over the last three years have resulted in the discovery of new QGP signatures.

One of the most striking signatures to come from the STAR collaboration is in the suppression of high p_T particles from central Au + Au collisions compared to p + p and d + Au collisions at $\sqrt{s} = 200$ GeV [90]. In these studies a statistical approach is adopted in order to correlate (as a function of azimuth) two high p_T particles. Here $N_{trigger}$ is the number of 'trigger' particles with $4 < p_T < 6$ GeV/c. The distribution of other tracks in the event, with $2 < p_T < p_T(trig)$ GeV/c is made with respect to the trigger track (with $p_T = p_T(trig)$) as a function of azimuth. The distribution is built up over a large number of events, with di-jets (which are back-to-back) being characterised by peaks at 0 and π radians in azimuth, as shown for p + p and d + Au charged hadron correlations in

is indicated by a peak at 0, and *no* corresponding peak at π radians. pQCD inspired models suggest that high energy partons that are responsible for jet production may lose energy by induced gluon radiation if they travel through a colour de-confined system [91]. Thus it may be possible for one of the jet-producing partons to escape the QGP (the 'trigger'), but for its partner to encounter a region of de-confined colour (the QGP), and be absorbed. Effectively the formation of the Quark-Gluon Plasma is believed to dissipate the energy of one of the jets, thus removing the back-to-back correlation observed in p + p and d + Au collisions. Showing that back-to-back correlations occur for charged hadrons in d + Au collisions was important, as it demonstrated the suppression was not due to nuclear modification of the parton distribution functions [92].

8.1 Outlook

Although strangeness appears to be enhanced at $\sqrt{s} = 200$ GeV, the decrease in enhancement as a function of $\sqrt{s}$ must be properly understood, if strangeness enhancement is to be regarded as a significant QGP signature. This indicates how important it is to understand the control measurement. Significantly, the suppression of high p_T particles represents one of the most compelling pieces of evidence for the formation of a de-confined state of matter. However, such analyses do not indicate a definitive 'discovery' of the QGP, as they are not sensitive to whether the system is thermalised. Although, as discussed in Chapter 2, the plasma should theoretically last sufficiently long for it to thermalise, the main experimental evidence for thermalisation remains in the fits obtained by thermal models, where the assumption of thermalisation is implicit. However, thermal models can also be used to succesfully fit results from p + p collisions where thermalisation cannot occur.

Approximately 100 million minimum bias Au + Au collisions at $\sqrt{s} = 200$ GeV have been collected in the latest completed RHIC run (Year 4). The increased statistics will enable the study of the rarer high p_T particles, allowing the p_T spectra for Λ, $\overline{\Lambda}$ and K^0_S to reach further out to higher p_T. It may then become more obvious that the heavy ion

explain the high p_T tail.

RHIC has been operating since July 2000, but the Large Hadron Collider (LHC) at CERN is scheduled to become operational in 2007. At the LHC $\mathrm{p}+\mathrm{p}$ collisions with maximum $\sqrt{s} = 14$ TeV will be possible; almost an order of magnitude larger than at the Tevatron, and almost two orders of magnitude than at RHIC. As calculated by Wang [49], at this energy ($\sqrt{s} > 4$ TeV) particle production is dominated by mini-jet fragmentation, and the Λ, $\overline{\Lambda}$ and K^0_S spectra determined by this analysis (where, at $\sqrt{s} = 200$ GeV soft particle production still dominates), will form a useful comparison.

At the LHC heavy ion collisions with $\sqrt{s} = 5.5$ TeV will be possible. At these energies, the Quark-Gluon Plasma is expected to live longer, and so the analyses may be more focused on exploring the properties of the de-confined phase, that has been glimpsed at the Relativistic Heavy Ion Collider.

Appendix A

Determination of N_{part}

As indicated in Figure A.1, the number of interacting nucleons, N_{part} in heavy ion collisions can be between two (for the most peripheral collisions) and $2A$ (for the most central collisions), where A is the nucleon mass number. Therefore, unless the heavy ion yields are scaled down, a comparison of yields from p + p and heavy ion collisions will not be useful. This section discusses this scaling process.

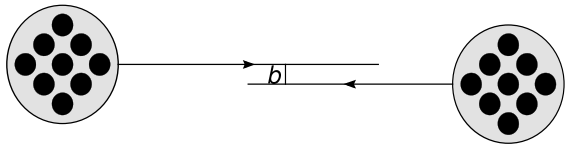

a) Central collisions have small impact parameter

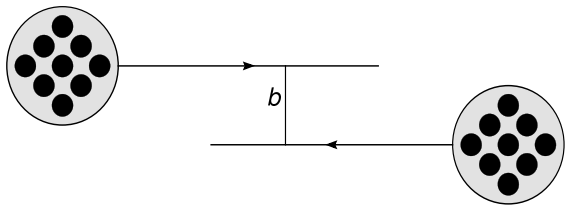

b) As the centrality decreases, the number of particpanting nucleons also decreases

Figure A.1: In heavy ion collisions, collision centrality is related to impact parameter. Energy densities and temperatures are expected to be greatest where the impact parameter, b, is smallest and the number of produced particles is largest.

For heavy ion collisions the centrality of an event determines the number of nucleons which have interacted. The lowest impact parameter collisions are called the most central

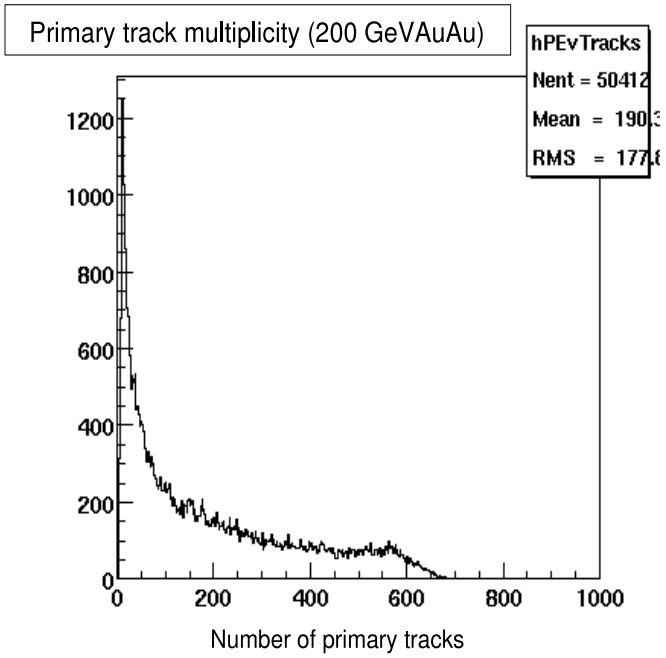

Figure A.2: The measured primary track multiplicity from Au + Au collisions at $\sqrt{s} =$ 200 GeV. For Au + Au collisions multiplicity is used to define event centrality.

events, with centrality decreasing with increasing impact parameter.

A direct measure of impact parameter is not possible, and instead, the experimentally measured particle multiplicity, as shown in Figure A.2 is used to give a measure of centrality. This is possible as the number of produced particles will increase with the number of interacting nucleons and therefore the centrality. The cross-section is divided into different centrality bins, with, for example, the most central collisions corresponding to those 5% of events with the largest multiplicity.

The number of interacting nucleons, corresponding to a particular centrality bin, must be theoretically calculated if yields from Au + Au and p + p collisions are to be compared. To do this STAR uses a Monte-Carlo based Glauber model [93]. In Glauber theory all of the nucleons are assumed to have only straight-line trajectories, and have the same interaction cross-section.

In the Monte Carlo model, two nuclei are generated with impact parameter, b, and the number of individual nucleon interactions are counted for that b. This process is repeated for many different randomly generated values of b.

0-5%	$352\ ^{+}_{-4}$
5-20%	$256\ ^{+7}_{-8}$
20-40%	$141\ ^{+9}_{-11}$
40-60%	$62\ ^{+8}_{-10}$
60-80%	$21\ ^{+5}_{-7}$

Table A.1: Table of number of participants and centrality determined using Glauber model calculations (taken from[94]). The numbers in this table were used in order to determine strangeness enhancement per participating nucleon (For Au + Au collisions at $\sqrt{s} = 200$ GeV).

The mean number of participating pairs of nucleons, N_{part}, is the number of nucleons that were hit, or interacted in some sense, which is why they are often also referred to as the number of wounded nucleons. When a nucleon pair has interacted once it cannot be counted again for N_{part}. The maximum value of N_{part} is 2×197, and will occur for a perfectly central Au + Au collision. Alternatively, the number of binary collisions, N_{bin} (where a nucleon can be counted as undergoing more than one collision) can be used to scale the yields, where for a perfectly central collision, the maximum value of $N_{bin} = 197^2$. Binary collision scaling is expected to work best for high p_T particles (> 2 GeV [73]), where as N_{part} scaling is expected to work at low p_T.

The measured multiplicity can be correlated with the Monte Carlo generated particle multiplicity. As the number of participating nucleons is related to the collision centrality (which can be inferred from the multiplicity), the number of participants as a function of centrality, can be determined (Table A.1) [94]. The values of N_{part} shown in Table A.1 were used to help determine the strangeness enhancement factors as a function of centrality shown in Figure 7.9.

Bibliography

[1] J. Adams and M. Heinz (STAR Collaboration), nucl-ex/0403020.

[2] G D Rochester and J G Wilson, Cloud Chamber Photographs of the Cosmic Radiation, (Pergamon Press London, 1952).

[3] M. Gell-Mann, Phys. Lett. 8, pp214 (1964).

[4] W. Bartel et al, Phys. Lett. 28B, pp148 (1968).

[5] R. Feynman, Phys. Rev. Lett. 23 pp1415 (1969).

[6] D. J. Gross. F. Wilczek, Phys. Rev. Lett. 30 pp1343 (1973).

[7] Eidelman et al. (Particle Data Group), Phys Lett B592, pp1 (2004).

[8] S.Hahn (DELPHI), Nucl. Phys. B (Proc. Suppl.) 74 pp12 (1999).

[9] D.Perkins, Introduction to High Energy Physics, pp 44(Cambridge University Press, 2003).

[10] A. C. Benvenuti et al., Phys. Lett. B223, pp490 (1989).

[11] J.C.Collins, M.J.Perry, Phys. Rev. Lett. 34, pp1353 (1975).

[12] C. Wong, Introduction to High-Energy Heavy Ion Collisions, pp344 (World Scientific, 1994).

[13] I. J. R Aitchison and A. J. G Hey, Gauge theories in Particle Physics (Adam-Hilger, 1989).

[14] D. Boyanovsky, hep-ph/0102120.

[16] F. Karsch, Nucl. Phys. A698, pp199 (2002).

[17] F. Karsch, A Peikert and E. Laermann, hep-lat/0012023.

[18] R. Xu Chin. J. Astron. Astrophys. astro-ph/0407074.

[19] S. Hands Contemp.Phys. 42 209 (physics/0105022) (2001).

[20] H. Caines (STAR Collaboration), nucl-ex/0412016

[21] J.D. Bjorken, Phys. Rev. D27 pp140 (1983).

[22] J.Rafelski and B. Muller, Phys. Rev. Lett. 48, pp1066 (1982).

[23] P. Braun-Munzinger, D. Magestro K.Redlich, J.Stachel.,nucl-th/0304013.

[24] E.Anderson et al, (WA97 Collaboration),Phys. Lett. B 449, pp401 (1999).

[25] F. Antinori et al., (NA57 Collaboration), Phys. Lett. B595, pp68 (2004).

[26] S.S. Adler, et al, (PHENIX collaboration) nucl-ex/0409015.

[27] T. Akesson Phys. Lett. 108B no.1 pp58 (1982).

[28] R.E.Ansorge et al, (UA5 Collaboration) Nucl. Phys. B328, pp36 (1989).

[29] D.Perkins, Introduction to High Energy Physics, pp172 (Cambridge University Press, 2003).

[30] S. Kretzer, hep-ph/0003177 (2000).

[31] D. Stump et al., hep-ph/0303013.

[32] G. Bocquet et al (UA1 Collaboration), Phys. Lett. B 366, pp441 (1996).

[33] T.Alexopolous et al (E735), Phys. Rev. D Vol 48 , pp3, pp984 (1993).

[34] F. M. Borzumati, G. Kramer, Z. Phys C 67 pp137 (1995).

[35] R. Hagedorn, Riv. Nuovo Cimento 6, pp1 (1983).

ex/0304038 (2003).

[37] D.E.Soper hep-ph/9702203.

[38] B.Andersson, G. Gustafson, G. Ingelsman and T. Sjostrand Phys Rep. 97 31 (1983).

[39] D.Perkins, Introduction to High Energy Physics, pp 180(Cambridge University Press, 2003).

[40] T. Sjostrand et al. Pythia 6.2, Physics and Manual, hep-ph/0308153 (2002).

[41] X. N. Wang and M. Gyulassy, Phys. Rev. D 44 3501 (1991).

[42] I. Dawson et al. Czech Journal of Phys. Vol. 53 Suppl A, A1 (2003).

[43] T. Alexopoulos et al, Phys. Lett. B, 435, 453 (1998).

[44] B. Alper et al., Nucl. Phys. B100 pp237 (1975) .

[45] C. Albajar et al., Nucl. Phys., B 309 pp405 (1988).

[46] T. K. Gaisser and F. Halzen PRL, V54 No16 pp1754 (1985).

[47] L. Durand and H. Pi, PRL 58 v4 pp 303 pp303 (1987).

[48] X. N.Wang and R. C. Hwa Phys Rev D 39 187 (1989).

[49] X. N Wang Phys Rev D Vol43 No1 pp104 (1991).

[50] C. Wong, Introduction to High-Energy Heavy Ion Collisions, pp29 (World Scientific, 1994).

[51] A. Giovannini and R. Ugoccioni, hep-ph/9710361.

[52] A. Dumitru, hep-ph/9810378.

[53] J. Adams et al., (STAR Collaboration) nucl-ex/0501009.

[54] T. B. Biro, E. van Doorn, B.Muller and X. N Wang. nucl-th/9303004.

[56] K. J. Eskola and X. N. Wang, nucl-th/9307011.

[57] J. Rafelski, Phys. Lett. B 262, 333. (1991)

[58] P. Braun-Munzinger nucl-th/9508020.

[59] J. Cleymans, F. Becattini hep-ph/0011322.

[60] P. Braun-Munzinger, D. Magestro K.Redlich, J.Stachel., hep-ph/0105229

[61] F. Becattini et al. hep-ph/9708248.

[62] F.Becattini hep-ph/9702274.

[63] J. Adams et al., (STAR Collaboration) nucl-ex/0309012.

[64] C. Wong, Introduction to High-Energy Heavy Ion Collisions, pp 71 (World Scientific, 1994).

[65] M. Harrison et al., Nucl. Instrum. Meth.,A499 235 (2003).

[66] The STAR experiment website, www.star.bnl.gov

[67] H. Hahn et al., Nucl. Instrum. Meth.,A499 245 (2003).

[68] K.H.Ackermann et al, (STAR Collaboration), Nucl. Phys. A661, 681c (1999).

[69] K.H.Ackermann et al, (STAR Collaboration), Nucl. Instrum. Meth. A499, 624 (2003).

[70] M. Anderson et al, Nucl Instrum. Methods A 499 659 (2003).

[71] C. Wong, Introduction to High-Energy Heavy Ion Collisions, pp28 (World Scientific, 1994).

[72] I. M Sakredja, J. T. Mitchell, Tracking for the STAR TPC, STAR note SN 0190 (unpublished).

[73] J. E. Gans, PhD Thesis, Yale University (USA) (2004).

[75] J. Balewski, (STAR Collaboration) Author of PPLMV software.

[76] G. Knoll, Radiation Detection and Measurement, pp32 (Wiley, 1989).

[77] R. Brun et al., GEANT user Guide, CERN Report DD/EE/84-1 (1987).

[78] M. Lamont, PhD Thesis, University of Birmingham,UK (2002).

[79] L. Lyons, A Practical Guide to Data Analysis for Physical Science Students (Cambridge University Press, 1991).

[80] R. Witt (STAR collaboration), J. Phys. G 31 (2005).

[81] F. James and M. Roos., Comput. Phys. Commun., 10:343-367, (1975).

[82] J. Letessier, J. Rafelski, Hadrons and Quark Gluon Plasma (pp144) (Cambridge University Press, 2002).

[83] S. Albino, B. A. Kniehl and G. Kramer, hep-ph/0502188 (2005).

[84] B. A. Kniehl and G. Kramer and B.Pötter, Nucl. Phys. B582, 514 (2000).

[85] M. Heinz, (STAR collaboration), hep-ex/0501017 (2004).

[86] H. Caines, (STAR collaboration), nucl-ex/0412015 (2004).

[87] G. E. Bruno (NA57 collaboration) J.Phys. G30 pp717 (2004).

[88] R. J. Fries, B. Muller, C. Nonaka, S. A. Bass, Phys.rev C68:044902 (2003) [nucl-th/0306027].

[89] A. Tounsi, A. Mishke and K. Redlich, Nucl. Phys A715 pp565 (2003).

[90] J. Adams, et al. (STAR Collaboration) Phys.Rev.Lett. 91:172302 (2003) [nucl-ex/0306024].

[91] M. Gyulassy, I. Vitev, X-N Wang and B-W Zhang, nucl-th/0305010.

[92] J. J. Aubert et al, Nucl. Phys., B293 pp740 (1987).

[94] M. Miller, PhD Thesis, Yale University, USA (2003).